

ABSTRACT

Title of dissertation: **EXPERIMENTS WITH A
SUPERFLUID BEC RING**

Avinash Kumar, Doctor of Philosophy, 2018

Dissertation directed by: **Professor Gretchen Campbell
Department of Physics**

This dissertation presents multiple results of our experiments with ring-shaped ^{23}Na Bose-Einstein condensates. First, we measure the effect of temperature on the lifetime of quantized, persistent currents. We find that the persistent current lifetime decreases when the temperature is increased. We also extract the critical velocity by measuring the size of hysteresis loops. The critical velocity is found to be a strong function of temperature. Second, we implement a new technique of measuring the circulation state of a persistent current in-situ, which is minimally-destructive. This technique uses the Doppler effect. We then measure the current-phase relation of a weak link inserted in the ring-shaped superfluid and measure the excitation spectrum of the ring-shaped superfluid. Finally, we study the dynamics of rapidly expanding rings, and explore the analogy between our experimental system and the expansion of the universe.

EXPERIMENTS WITH A SUPERFLUID RING

by

Avinash Kumar

Dissertation submitted to the Faculty of the Graduate School of the
University of Maryland, College Park in partial fulfillment
of the requirements for the degree of
Doctor of Philosophy
2018

Advisory Committee:

Professor Steven L. Rolston, Chair

Dr. Gretchen K. Campbell, Advisor

Dr. Charles W. Clark

Professor Christopher Jarzynski, Dean's Representative

Professor Christopher J. Lobb

© Copyright by
Avinash Kumar
2018

Dedication

This thesis is dedicated to my beloved family, friends and colleagues who have stood by me through good times and bad. I would have nothing without their support. As I write this, I realize my fortune to have a strong emotional backup system, which has made the journey through graduate school possible.

I have a special mention: my maternal grandfather Shri Shiv Shankar Prasad Singh. Three weeks after my thesis defense, he left this world for his heavenly abode. Life will never be the same without him. I pray that I can do something in my life that can make him proud. My grandmother, Shrimati Shobha Devi remains with us, and I pray for her long life.

Acknowledgments

I had a very educational and enjoyable stay in the laser cooling and trapping group at the Joint Quantum Institute, exploring multiple aspects of superfluidity. This thesis, which summarizes these experiments, has been made possible by contributions of multiple people. I will forever be grateful for their help.

First of all, I would like to thank my advisor Dr. Gretchen Campbell for giving me the opportunity to work in her group. I have always been amazed by her knowledge, patience, and eagerness to educate. I joined this group with no prior experience in an experimental lab. She had to teach me even the most basic things in the lab, like using a soldering iron or coupling light into a fiber. She was very supportive while I learned these basic skills. I was fortunate to have well defined goals throughout my PhD. She has been very approachable throughout my stay, whether it be for scientific problems or my own personal problems. It has truly been a privilege to work in this group.

The duration of my PhD can be divided into two major parts. The first part was spent on the NIST Gaithersburg campus. There, I had the fortune to work with several exceptional postdocs: Steve Eckel, Fred Jendrzejewski and Kevin Wright, all of them are now heading their own research groups. I overlapped the most with Steve, and he has played a great role in making all the experiments in this thesis possible. Steve had valuable suggestions on all aspects of the experiment: optics, electronics, data analysis and insight into the physics of the problem. Kevin got me started on my first electronics projects, helping me design digital buffer boxes and

vacuum interlock. Fred had valuable feedback on multiple projects, especially the projects on the decay of persistent current and analyzing the excitation spectrum of the ring superfluid.

Working at an institution like Joint Quantum Institute means you are working in the proximity with some of the world's leading researchers in laser cooling and trapping. I have benefited tremendously with my interaction with Charles Clark. Charles has been a great mentor for me, providing me with great advice for my postdoc and internship search. He has been very helpful in interpreting our experimental results, especially the data on the excitation spectrum of a superfluid ring. In Mark Edwards, I found a person who could educate me in the numerical techniques for simulating Bose-Einstein condensates. Eite and his student Ranchu collaborated with us, looking at the time evolution of interference patterns when a ring condensate is released from a target trap.

The other PI's in the laser cooling and trapping group: Paul Lett, Ian Spielman, Trey Porto and Steve Rolston, have contributed to my knowledge of ultracold atoms. I am thankful to Ian for encouraging us to start a project on studying ring superfluids in a dynamic potential with radial expansion. This project made us think about the connections between cosmic inflation and a rapidly expanding superfluid ring. Paul helped me with questions on dye lasers and electromagnetically induced transparency. I cherish the Wednesday meeting with Trey's and Steve's group, where I have been introduced to multiple ideas and occasional questions to solve on the board.

I have also benefited by interacting with Bill Phillips. His enthusiasm for

science is contagious. His enthusiasm is on full display when he introduces laser cooling and trapping to a group of beginners. He has provided a lot of input in the final draft of the research publications we have submitted. His reading of our manuscript is rigorous and challenging. I feel that he has a knack of bringing out all the aspects that you tried to push under the carpet, and even grammatical errors are not spared. All of our manuscripts have benefited tremendously from his reading.

Chris Lobb has been our go to person for drawing analogies between superconducting systems and a ring-shaped superfluid with a weak link. We have used his expertise for interpreting the current-phase relation of the weak link and the decay of persistent current in a superfluid ring. He also helped me in going through the textbook by Tinkham when I was reading about superconductivity for the first time.

The second part of my PhD was spent at the University of Maryland campus, after shifting our lab from Gaithersburg. This move gave us an opportunity to re-design our experiment and make improvements. I joined a group consisting of Hector, Madison, Monica and Swarnav in building the new generation of the sodium BEC experiment. I learned about design and construction of an experiment from scratch. This group took an empty room and converted into a functioning ultracold experiment. At the time of writing this thesis, they are within a factor of few from achieving Bose-Einstein condensation. I would also like to thank Alessandro for the sea change he has brought in the way electronics projects are executed at JQI. Some of the electronics boxes are better than the commercial version.

I have also benefited from my interaction with other graduate students, espe-

cially Gretchen's strontium lab. Dan Barker and Ben Reschovsky were very helpful when I was trying to find my feet in this area of research. Neal Pisenti has pulled me out of technical issues several time, especially during electronics projects. I have received help from graduate students of other labs as well. Zach Smith was very helpful when I was implementing the computer control for the new lab. Elizabeth Goldschmidt, now a PI at Army labs have always been willing to give me career advice. Other graduate students and postdocs in the group: Dina Genkina, Lauren Aycock, Don Fahey, Arne, Hsin-I, Roger, Abby, Tian, Prasoon; were always generous in sharing lab supplies when we ran out of equipment.

I would like to acknowledge financial support from the Physics Frontier Center which provided for my stipend, tuition and fee. I am also grateful for the dedicated staff at the UMD physics department and at NIST. Without Melissa, Cindy, Gail and Kim, a smooth procurement of experimental equipment would be very difficult.

Lastly, I would like to thank my family for their support. I am grateful to my parents and grandparents who raised me and instilled the passion for education. They provided me with more resources for education than they themselves received. My elder sister was a very effective mentor during my early education. I first met my wife in high school. In her, I have found a good friend and companion, who has kept my spirits up when things would not work for me in the lab. I lost several months of work because of an accident, and she was there at my side giving me strength. I have also received lot of support from my father and mother in-law about my decision to pursue further education. I could not have asked for a better support environment at home, every member of my extended family that I know of

has expressed pleasure on my decision to pursue a doctorate.

It is impossible to remember and mention everyone here, so I apologize to all of those I have forgotten to mention.

Table of Contents

Dedication	ii
Acknowledgements	iii
List of Figures	xi
List of Abbreviations	xx
1 A brief history of superfluidity and superconductivity	1
1.1 Overview of Fundamental concepts	6
1.1.1 Order parameter	6
1.1.2 Healing length	7
1.1.3 Quantized Persistent currents	7
1.1.4 Modeling superfluid flow	9
1.1.5 Critical velocity and phase slips	10
1.1.6 Phase Slips	15
1.1.7 Hysteresis, energy landscape and particle interactions	16
1.2 Relevance of this work	20
1.2.1 Previous work done	20
1.2.2 Results of this thesis	22
2 Experimental details	27
2.1 Experimental setup	27
2.2 Experimental steps	29
2.3 Electronics development	38
2.3.1 Vacuum and Temperature Interlock	38
2.3.2 Digital Buffer	42
2.4 Optics Setup Development	42
2.4.1 Optical setup for ring potential	42
2.4.2 Red detuned dipole trap for vertical trapping	45
2.4.3 Blue detuned potentials for vertical trapping	47
2.4.4 Imprinting a circulation state	52

3	Interferometric Measurement of the Current-Phase Relationship of a Superfluid Weak Link	53
3.1	Overview	54
3.1.1	Tunneling in quantum degenerate systems	54
3.1.2	Phase coherence of BECs	56
3.2	Experimental setup	57
3.3	Analysis of the Interferogram	59
3.3.1	Extracting the winding number	59
3.3.2	Extracting the current phase relation	60
3.4	Theoretical model	62
3.5	Non-quantization of the angular momentum	64
3.6	Experimental results	65
3.7	Tracking the time evolution of spirals	73
4	Resonant wavepackets and shock waves in an atomtronic SQUID	77
4.1	Overview	78
4.2	A simple model of resonant wavepacket generation by an oscillating weak link	81
4.3	Experimental Parameters	87
4.4	Bogoliubov - de Gennes description of elementary excitations of a BEC	89
4.5	Driving and Probing the Excitations	93
4.6	Generation of supersonic shock waves	100
4.7	Summary	103
5	Minimally destructive, Doppler measurement of a quantized, superfluid flow	104
5.1	Overview	105
5.2	Theory	109
5.3	Experimental details	111
5.4	Results	115
5.5	Conclusion	120
6	Temperature induced decay	121
6.1	Overview	122
6.2	Experimental procedure	134
6.3	Measuring the temperature	137
6.4	The effect of temperature on perturbation strength calibration	140
6.5	Table of Experimental parameters and fit	144
7	A rapidly expanding Bose-Einstein condensate: an expanding universe in the lab	145
8	Conclusions and Future Experiments	146

A	Electronics development	148
A.1	Vacuum interlock operation	148
A.2	Evaporation sequence	150
B	A rapidly expanding Bose-Einstein condensate: an expanding universe in the lab	153
	Bibliography	166

List of Figures

- 1.1 The energy landscape for a toroidal superfluid. In (a), the rest state $\ell = 0$ is the global energy minimum. In (b), the first circulation state $\ell = 1$ is the global energy minimum as an external rotating perturbation has been introduced in the system. 17
- 2.1 **This figure is taken from [1].** This figure shows the sodium D2 transition hyperfine structure. The $3S_{1/2}$ manifold makes the ground state and the $3P_{3/2}$ level makes the excited state manifold. The laser cooling and trapping is performed on the $F = 2$ to the $F' = 3$ cycling transition. An external magnetic field bias breaks the degeneracy of the hyperfine levels. The sodium atoms are transferred to the $|F = 1, m_F = -1|$ state for magnetic trapping, which has been indicated by an orange dot. 31
- 2.2 The schematic in this figure shows the implementation of a vacuum interlock. All the circuit components are digital, using components from the 7400 transistor-transistor logic (TTL) series. According to the naming convention: 7404 is a hex inverting gate, 7408 is a 2 input AND gate, 7432 is a 2 input OR gate and 7474 is a D flip-flop. The symbols VSS and PE denote a voltage of +5V and ground respectively. Any symbol beginning with R and LED shows a resistor and a light emitting diode respectively. The symbol DB9 shows the cable carrying info from the vacuum gauge controller to the vacuum interlock. Toggle switches are denoted by X3 and X4, X3 is the switch for disabling the interlock, while X4 is the switch for manually enabling the interlock again. The output of the AND gate V3/1 goes to the relay controlling the gate valve. 40

2.3	The schematic in this figure shows the implementation of a digital buffer. All the circuit components are digital. The input BNC signals U_5 and U_6 are shown to the left, while the output signals U_1 and U_2 are to the right. The optocouplers are depicted by the part number HPCL 7720. These optocouplers couple the input side to the output side optically, cutting down on the electrical noise and crosstalk between various channels. The part number 74AC125N shows a one input digital buffer, where the output tracks the input. The symbols VDD and VSS denote the +5V power supply to the input and the output side. The symbols GND and GND1 denote the ground connection to the input and the output side. The power supply to the input and the output side are kept separate to prevent noise coupling.	41
2.4	Setup for shaping a red-detuned Gaussian beam into a light sheet. The optical parts shown as A1,A2,A3 and A4 are a translation stage, focusing objective, half wave-plate and a cylindrical lens respectively. Their part numbers have been listed in section 2.4.2	46
2.5	Optical parts labeled in the figure are: A1 is fiber mount with translational adjustments in both the x and the y axis (Thorlabs part number C110TME-A), A2 is a cage mounted polarizing beam splitter cube (Thorlabs part number CM1-PBS251), A3 is cylindrical lens of focal length 40 mm, A4 is an iris for alignment purposes, A5 and A6 are mirrors, A7 is an achromat of focal length 300 mm used to measure the power in the beam (Thorlabs part number AC508-300-A1), A8 is a pi phase plate, A9 is an achromat of focal length 200 mm and A10 is a photodiode to intensity lock the beam (Thorlabs part number PDA36A)	49
2.6	The above image is a false color absorption image of the atoms when they are are being transferred from the TOP trap to the blue-detuned sheet. This image shows a situation when the relative position of the TOP trap and the blue-detuned trap is adjusted for maximum transfer efficiency. The picture follows a false color scheme, dark blue and dark red represent regions of regions of lowest and highest atomic density respectively. In the picture above: three separate atomic clouds labeled as A,B and C can be seen. The atomic cloud on the left, shown as ‘A’, is a group of atoms that were transmitted through the blue-detuned sheet after being released from the TOP trap. The atomic cloud on the center, shown as ‘B’, is a group of atoms that were captured by the blue-detuned sheet after being released from the TOP trap. The atomic cloud on the right, shown as ‘C’, is a group of atoms that were reflected by the blue-detuned sheet after being released from the TOP trap. The gravitational field acts from the right to the left. This image was taken using horizontal imaging system.	50

2.7	The above image is a false color absorption image of the atoms when they are being transferred from the TOP trap to the blue-detuned sheet. This image shows a situation when the relative position of the TOP trap and the blue-detuned trap is adjusted for minimum transfer efficiency. The picture follows a false color scheme, dark blue and dark red represent regions of lowest and highest atomic density respectively. In the picture above: two separate atomic clouds labeled as A and B can be seen. The atomic cloud on the left, shown as ‘A’, is a group of atoms that were transmitted through the blue-detuned sheet after being released from the TOP trap. The atomic cloud on the right, shown as ‘B’, is a group of atoms that were reflected by the blue-detuned sheet after being released from the TOP trap. No atoms were trapped in the sheet trap, and hence cannot be seen in the time of flight images. The gravitational field acts from the right to the left. This image was taken using horizontal imaging system.	51
3.1	Figure taken from [2]. Example of a possible phase/density profile around the ring. The phase profile has been evaluated in a frame co-rotating with the weak link. The green curve shows the density and the blue curve shows the phase. As we are in the rotating frame, the phase accumulated around the ring by the velocity (as measured in this frame) must be equal to $2\pi(\Omega/\Omega_0) - 2\pi\ell$, where ℓ is the circulation state. The additional phase drop due to the weak link γ is also shown in the figure.	63
3.2	Figure taken from [2]. (a) <i>In-situ</i> image of the ring and disc BECs. The dimensions can be estimated using the scale bar shown in the figure. (b) Example interferogram after 15 ms time-of-flight (left) when there is no current in the ring. Traces of the azimuthal interference fringes extracted from an image processing algorithm have been drawn as a guide to the eye (right). (c) Interferograms for various winding numbers, where the arrow indicates the direction of flow. (d) Traces of the interference fringes to guide the eye and count the number of spiral arms. The extracted winding number is also shown.	67
3.3	Figure taken from [2]. (a) Schematic of the atoms in the trap with a weak link applied. The coordinate system used throughout is shown; $\theta = 0$ corresponds to the \hat{x} axis. (b) A close up of the weak link region. When the weak link is rotated at Ω , atoms flow through the weak link as shown by the stream lines. Larger velocities along the stream lines correspond to darker lines. (c) The resulting density $n(\theta)$, velocity $v(\theta)$, and phase $\phi(\theta)$ as a function of angle, with the phase drop γ across the weak link shown. (d) Method of extracting the phase from an interferogram (left). First, we trace the interference fringes around the ring (center) and then fit the discontinuity across the region where the barrier was (right).	69

3.4	Figure taken from [2]. Plot of the normalized current around the bulk of the ring, $I_{bulk}/I_0 = \alpha/2\pi$, vs. the rotation rate Ω of the weak link for four different weak link potential strengths U : (a) $0.45 \mu_0$, (b) $0.6 \mu_0$, (c) $0.7 \mu_0$, (d) $0.8 \mu_0$. The solid lines are the prediction of local density approximation (LDA) model. The dashed, vertical lines show the predicted transitions between the different winding number branches. The thin, gray, diagonal lines represent the limit of the solid body rotation, when all the atoms in the condensate move around the bulk of the ring with the weak link, i.e., $I_{bulk} = n_{1d}R\Omega$	71
3.5	Figure taken from [2]. (a) Derivative of the initial bulk current $dI_{bulk}/d\Omega$ vs. U , normalized to the expected value in the limit where $U/\mu_0 \geq 1$, $n_{1d}R$. The solid line shows the prediction of the LDA model. (b)–(d) Extracted current-phase relationships from the data in Fig. 3.4, for three different weak link potential strengths U : (b) $0.45 \mu_0$, (c) $0.6 \mu_0$, (d) $0.7 \mu_0$. γ is the phase across the weak link and I_{WL} is the current through it, normalized to $I_0 = n_{1d}R\Omega_0 \approx 5 \times 10^5$ atoms/s. The solid curves represent the prediction of our theoretical model. The dashed lines merely guide the eye by connecting the multiple branches of the current-phase relationship.	72
3.6	Figure taken from [3]. The radial spacing between azimuthal fringes is shown as function of time. The experimental data is for a condensate with no circulation state and weak link present before releasing the atoms in time of flight. The experimental, GPE and single-particle fringe spacings are shown by red dots with one-standard deviation statistical error bars, blue markers and a black line, respectively. The value of R has a uncertainty, which arises from the fit function. This uncertainty is shown by the shaded region around the blackline.	76
4.1	Figure taken from [4]. Trajectories of wavepackets in a ring when the strength of the weak link is modulated. The grey shaded areas represent the density depleted region, which changes as a function of time, t . The strength of the weak link oscillates with a frequency of $\nu_q = q\nu$: (a) $q = 1/2$; (b) $q = 3/2$; (c) $q = 1$; (d) $q = 2$. Here, ν is the orbital frequency of the phonons. The solid and dashed lines indicate the ring azimuthal coordinates, ϕ , of the centers of the wavepackets. The blue lines show the standing-wave-like density modulation created by the phonon wavepackets as they travel around the ring and overlap.	82

4.2	<p>Figure taken from [4]. Trajectories of wavepackets in a ring when the position of the weak link is modulated harmonically. The frequency of the modulation is given by $\nu_q = q\nu$, where (a) $q = 1/2$; (b) $q = 3/2$; (c) $q = 1$; (d) $q = 2$. Here, ν is the orbital frequency of the phonons. The grey shaded areas represents the density depleted region of the weak link, whose azimuthal position changes as a function of time, t. The solid and dashed lines indicate the azimuthal coordinate, ϕ, of the centers of the wavepackets. The blue lines show the standing-wave-like density modulation created by the phonon wavepackets as they travel around the ring and overlap. . . .</p>	83
4.3	<p>Taken from [4]. The BdG spectrum for the elementary excitations of a ring condensate. The blue (red) curves correspond to the excitation modes that are even (odd) in the axial (z) direction. The lowest branch represents the excitations in the azimuthal direction, the frequency of which is linear at small m (denoted by the black line). The slope determines the orbital frequency of sound $\nu = 37.9(2)$ Hz. . . .</p>	92
4.4	<p>Figure taken from [4]. Time evolution of phonon wavepackets generated through amplitude modulation of the barrier (see Fig. 4.1). The normalized 1D density (colorbar) shows wavepackets, or localized regions of high density, moving around the ring (azimuthal coordinate ϕ) with time t. The density also shows the barrier oscillating at $\phi = 0$ with frequency $\nu_q = q\nu$. Modes with $q = 1/2$ (a) and $q = 3/2$ (b) are nonresonant; modes with $q = 1$ (c and e) and $q = 2$ (d) are resonant. This corresponds to the ‘ring’ modes.</p>	95
4.5	<p>Figure taken from [4]. Time evolution of phonon wavepackets generated though position modulation of the barrier (see Fig. 4.2). The normalized 1D density (colorbar) shows wavepackets, or localized regions of high density, moving around the ring (azimuthal coordinate ϕ) with time t. The density also shows the barrier oscillating about $\phi = 0$ with frequency $\nu_q = q\nu$. Modes with $q = 1/2$ (a and e) and $q = 3/2$ (b) are resonant; modes with $q = 1$ (c) and $q = 2$ (d) are nonresonant. This corresponds to the ‘box’ modes.</p>	96
4.6	<p>Figure taken from [4]. Atomic loss spectra for an intensity modulated weak link. The numerical simulations are on the left and the experimental values are on the right. These results are for a weak link with a mean strength of $V_0/\mu = 0.30(2)$ (blue triangles) and $V_0/\mu = 0.50(4)$ (red circles). The y axis is the is the fraction of atoms N_R/N that remain in the trap after 2 s of excitation. The vertical black (red) lines correspond to the resonant frequencies of the box (ring) modes. The dashed lines are a guide to the eye.</p>	98

4.7	<p>Figure taken from [4]. Atomic loss spectra for a position modulated weak link. The numerical simulations are on the left and the experimental values are on the right. These results are for weak link heights of $V_0/\mu = 0.15(1)$ (green diamonds), $V_0/\mu = 0.30(2)$ (blue triangles), and $V_0/\mu = 0.60(4)$ (red circles), <i>with</i> ν_d being the drive frequency. The y axis is the fraction of atoms N_R/N that remain in the trap after 2 s of excitation. The vertical black (red) lines correspond to the resonant frequencies of the box (ring) modes. The dashed lines are a guide to the eye.</p>	99
4.8	<p>Figure taken from [4]. The above figure shows the azimuthal 1d density normalized to the background density for a supersonic flow in a BEC. To create the shock wave, the weak link is turned on non-adiabatically with a 100 μs ramp. The normalized density is shown vs. time. The numerical solution is on the left and the experimental measurement is on the right.</p>	101
5.1	<p>Taken from [5]. (a) Image of the ring condensate <i>in-situ</i> without an applied perturbation. (b) A sinusoidal perturbation excites a standing-wave superposition of counterpropogating phonon modes. The white line intersects the ring at the maximum and minimum of the perturbation. The left image shows the density; the average density is subtracted from the right image. These images show the resulting density modulation, 100 μs after the perturbation has been removed. (c) Full density (top) and average-subtracted-density (bottom) images taken 9.1 ms after removal of the perturbation. The density modulation rotates relative to the initial perturbation in the presence of superfluid flow. The winding numbers are shown below the images.</p>	107
5.2	<p>Taken from [5]. (a) Schematic of the setup used to trap the atoms and create the double ring potential and sinudoidal perturbation. A DMD is illuminated with blue-detuned light and is imaged onto the atoms using a telescope (solid lines) , which ensures that incoming collimated beams remain collimated after they emerge from the telescope (dashed lines). (b) The halftoned patterns \parallel written to the DMD for the bare ring potential (left) and the perturbed ring potential (right). (c) After convolution with the point-spread function of the imaging system, the potentials formed are smooth, and show a clear sinusoidal perturbation (right).</p>	111
5.3	<p>Taken from [5]. Plot of the normalized 1D density of the ring $n_{1D}(t, \theta)/n_{0,1D}(\theta)$ (see text) vs. angle, for different times after the perturbation. The solid blue lines show the experimental data and the red dashed lines show the fit to the data. Each trace represents one shot of the experiment. For these data, there is no persistent current present ($\ell = 0$).</p>	114

5.4	Taken from [5]. Plot of the normalized 1D density as a function of azimuthal angle and hold time after the perturbation. The three panels correspond to having different persistent currents in the ring: (a) $\ell = -1$, (b) $\ell = 0$, and (c) $\ell = 1$. For each time and winding number, there is one experimental shot (i.e., there is no averaging). The green lines show the expected precession of the antinodes of the standing wave, according to Eq. 5.3.	116
5.5	Taken from [5]. Histogram of the number of occurrences of measured precession angles of one of the antinodes of the standing wave at $t = 35.1$ ms. The red curve is a fit of three, independent Gaussians. These Gaussians correspond to three different winding numbers: $\ell = -1$, $\ell = 0$, and $\ell = 1$ (left to right).	118
6.1	Taken from [6]. Target shaped condensate, energy landscape and effective escape temperature (color online). a) <i>In situ</i> image of trapped atoms, with 5% of the total atoms imaged [7]. Experiments are performed on the ring-shaped BEC and the resulting winding number ℓ is read out by interfering the ring condensate with the disc-shaped BEC in time of flight. The disc-shaped BEC acts as a phase reference. (b) Energy landscape showing the stationary state, $\ell = 0$, and the persistent current state, $\ell = 1$, as minima in the potential. The energy barrier E_b needs to be overcome for a persistent current to decay from $\ell = 1$ to $\ell = 0$. The decay can be induced either via thermal activation (TA), or quantum tunneling (QT). (c) Crossover from quantum tunneling to the thermally activated regime. The escape temperature T_{esc} (see text) first remains constant (horizontal blue line) and then becomes equal to the physical temperature T (slanted gray line). A dotted line acts as a guide to the eye depicting $T_{esc} = T$	125
6.2	Taken from [6]. (color online). (a) Average measured winding number $\langle \ell \rangle$ vs. t , the duration for which a stationary perturbation is applied. The four data sets correspond to different strengths of the stationary perturbation U_b : $0.50(5)\mu$ (circles), $0.53(5)\mu$ (squares), $0.56(6)\mu$ (inverted triangles) and $0.59(6)\mu$ (triangles). Here, μ is the unperturbed chemical potential. The temperature of the superfluid was $85(20)$ nK. The solid curves show exponential fits. (b) The average measured winding number $\langle \ell \rangle$ vs. U_b for fixed t : 0.5 s (circles), 2.5 s (squares) and 4.5 s (inverted triangles). The solid curves show a sigmoidal fit of the form $\langle \ell \rangle = [\exp((U_b/\mu - \zeta)/\alpha) + 1]^{-1}$. The temperature of the superfluid was $40(12)$ nK.	126

6.3	Taken from [6]. (color online). Measured decay rate of the persistent current Γ as a function of perturbation strength U_b for four different temperatures: 30(10) nK (circles), 40(12) nK (squares), 85(20) nK (inverted circles) and 195(30) nK (triangles). The solid lines are fits of the form $\Gamma = \Omega_a \exp(E_b/k_B T_{esc})$, where E_b is the energy barrier, k_B is the Boltzmann constant, and T_{esc} and Ω_a are fit parameters. The inset shows the extracted T_{esc} as a function of measured physical temperature: 30(10) nK (triangle), 40(12) nK (square), 85(20) nK (circle) and 195(30) nK (inverted triangle). The solid line shows $T_{esc} = T$	129
6.4	Taken from [6]. Hysteresis loop for a perturbation strength of $0.64(4)U_b/\mu$ for 40(12) nK (a), 85(20) nK (b), and 195(30) nK (c).(d) Size of the hysteresis loop, $(\Omega_+ - \Omega_-)/\Omega_0$ (see text), vs. barrier strength for three different temperatures: 40(12) nK, diamonds, 85(12) nK (squares), and 195(12) nK (triangles). The zero temperature, GPE predicted, area of the hysteresis loop is shown as a purple band, which incorporates the uncertainty in speed of sound. The left y axis of the inset shows the hysteresis loop size shown in (a)-(c) as a function of temperature for a perturbation strength of $0.64(4)U_b/\mu$. The right y axis of the inset shows the corresponding extracted critical velocity (mm/s).	132
6.5	Taken from [6]. The experimental sequence for measuring current decay. A stationary perturbation with height $U_b/\mu \approx 1.1$, where μ is the chemical potential is turned on during T_{sp} to destroy any spontaneous circulation. A rotating perturbation with the same height imprints the $\ell = 1$ circulation state during T_{int} . A stationary perturbation with strength less than the chemical potential (shown here as $0.5U_b/\mu$) probes the circulation state for t . An intermediate step $T_{exp} - t$ is introduced to ensure that the total experimental time T_{exp} remains constant.	136
6.6	Taken from [6]. Measured temperature vs. power in the red-detuned (1064 nm) vertical trapping beam. The errorbars show the statistical uncertainty.	137
6.7	Taken from [6]. Measured temperature vs mask beam power. Measurements are for a vertical trapping frequency of 520 Hz (circles) and 970 Hz (triangles) as a function of power in the radial trapping beam incident on the DMD. The experiment was carried out with the lowest radial trapping power of 14.6 mW.	139

6.8	<p>Taken from [6]. (a) Computed condensate fraction as a function of temperature. The points show the results of our ZNG calculations for a vertical trapping frequency of 512 Hz (see text). A fit of the form $N_c/N = 1 - (T/T_c)^\alpha$ with $\alpha = 2.22(9)$ is also shown. (b) Computed chemical potential as a function of temperature. The red line shows a fit of the form $\mu(T)/\mu(T = 0) = 1 - (T/T_c)^\beta$ with $\beta = 2.72(4)$. For reference, the dash-dot line shows $\mu(T)/\mu(T = 0) = [1 - (T/T_c)^\alpha]^{1/2}$, expected from the Thomas-Fermi approximation. The difference between these two curves yields the first order correction to the barrier calibration as a function of temperature.</p>	141
A.1	<p>The figure above shows the waveforms during a typical evaporation sequence to produce a BEC in a red-detuned sheet. The first panel shows the current flowing in the quadrupole coils producing a field of 1.2 G/(A-cm). The second panel shows the voltage of the analog switch controlling the power to the amplifier for the TOP trap coils. The third panel shows the power in the red-detuned sheet. The last panel shows the frequency of the RF field responsible for evaporative cooling in MHz. The red-lines separate marks the end of a step in the sequence, which have been detailed in the table A.1</p>	151

List of Abbreviations

α	alpha
β	beta
AOD	acousto-optic deflector
BCS	Bardeen, Cooper and Schreiffer
BEC	Bose-Einstein condensation
BKT	Berezinskii-Kosterlitz-Thouless
DMD	Digital micro-mirror device
GPE	Gross-Pitaevskii equation
GL	Ginzburg-Landau
LDA	local density approximation
LG	Laguerre-Gauss
MOT	magneto-optical trap
PTAI	partial transfer absorption imaging
RF	radio frequency
SQUID	superconducting quantum interference device
TDGPE	time dependent Gross-Pitaevskii equation
TEM	transverse electromagnetic
TF	Thomas-Fermi
TOP	time orbiting potential
TTL	transistor-transistor logic
TWA	Truncated-Wigner approximation
UHV	ultra high vacuum
ZNG	Zaremba-Nikuni-Griffin

Chapter 1: A brief history of superfluidity and superconductivity

Temperature is a measurement of the average kinetic energy in any physical system. Progress in science and technology has made access to extreme ranges of temperature possible: hot plasma fusion experiments with temperatures reaching 10's of millions degrees [8] down to ultracold atoms experiments, which reach 500×10^{-12} K [9]. This thesis addresses questions related to the behavior of materials at low temperatures. Whether the behavior of a physical system is decided by classical or quantum mechanics is determined by the ratio between the de-Broglie wavelength λ_d and the inter-particle separation l_p . The work of de-Broglie established matter wave duality and showed that associated with each particle is a wavelength which is inversely proportional to its momentum. As a particle confined to a potential cools down, the de-Broglie wavelength increases, while the inter-particle separation decreases. When the two become comparable $\lambda_d \simeq l_p$, and quantum effects begin to dominate. This dominance of quantum effects at low temperatures give rise to several interesting phenomenon like superconductivity and superfluidity in some materials.

At the start of the 20th century there were rapid advances in the study of low temperature physics. One of the pioneers in this field was Kammerlingh Onnes,

who was the first to liquefy helium in 1908 [10]. Three years later, he found that the resistance of a mercury wire immersed in liquid helium drops to zero [11], a phenomena which he coined superconductivity. He also found that at a particular temperature a superconductor in the shape of a loop can sustain current for a very long time, these states were called persistent current states [12]. Interestingly, even though Onnes was the first to liquefy helium, and later used liquid helium as a medium to investigate conductivity of metals, he never investigated the transport properties of liquid helium in detail. It was left to Kapitsa [13], Allen and Misener [14] who liquefied helium and discovered superfluidity. They found that the kinematic viscosity of a flow of helium had dropped by three orders of magnitude after crossing the lambda point.

Meanwhile, in parallel to experimental studies, theoretical efforts were ongoing to understand superconductivity and superfluidity. Ginzburg and Landau first came up with a phenomenological model to study superconductivity without addressing the underlying microscopic theory. Using Landau's theory of second-order phase transitions, Ginzburg and Landau argued that the free energy of a superconductor near the superconducting transition can be expressed in terms of a complex order parameter field ψ , which is nonzero below a phase transition into a superconducting state, and is related to the density of the superconducting component. This work failed to give a direct interpretation of this parameter, i.e. relate this wavefunction to physical variables. A microscopic theory of superconductivity was first provided by Bardeen, Cooper and Schreiffer (BCS) [15]. They proposed that electrons near Fermi surfaces can become weakly attractive despite the existence of a strongly repulsive

Coulomb force between them, this pair may then condense and form Cooper pairs. Cooper showed that an arbitrarily small attraction between electrons in a metal can cause a paired state of electrons to have a lower energy than the Fermi energy, which implies that the pair is bound. In conventional superconductors, this attraction is mediated by electron-phonon interaction.

A similar macroscopic approach of studying superfluidity was taken by Gross and Pitaevskii (GP equation), who described the ground state of a quantum system of identical bosons using the Hartree-Fock approximation (mean field theory). This assumed that the different particles would be interacting via contact interaction. One of the issues with this approach was that it assumed zero temperature, and so dissipation had to be added phenomenologically. Also, strong interactions as seen in superfluid helium make modeling experimental results harder.

The development of low temperature techniques ran concurrently with another series of developments, where the foundations of quantum mechanics were being laid. Sub-atomic particles like the neutron, proton and electron were found, and it was discovered that they had intrinsic angular momentum called spin. The spins were either integers or half-integers. Particles with half-integer spins were called fermions and particles with integer spins were called bosons. Two fermions cannot occupy the same state, so at low temperatures all quantum states up to the Fermi energy are filled. On the other hand, when cooled down to sufficiently low temperatures, bosons occupy the ground state of the system. This state of bosons occupying the lowest energy level is called Bose-Einstein condensation, which was first predicted in 1925.

Even though physical systems like superconductors and superfluids exhibited quantum degenerate behavior, only a small fraction of the constituent particles occupied the lowest ground state, a picture of the condensate consistent with the original description of Bose and Einstein. This depletion of the ground state was a result of strong interactions, which also made the system very difficult to model. The search for a dilute condensate had one constraint, a lower density required ultracold temperatures to reach a phase space density of over unity. These temperatures were made possible by a combination of laser cooling and RF evaporation techniques. BEC in dilute ultracold alkali gases were first demonstrated in 1995 [16, 17]. Since the realization of BECs, they have become a testbed for condensed matter theory.

The efforts to make a dilute condensate began by cooling of spin polarized hydrogen, and then was extended to dilute alkali gases (dilute means that the s-wave scattering length is much less than the inter-particle spacing). A condensate for dilute alkali gases was obtained before spin polarized hydrogen because of the following conducive properties:

- A hydrogen atom has a scattering length of $1.1 a_0$ (Bohr radius), while scattering length of sodium and rubidium is $52 a_0$ and $102 a_0$ respectively. The large scattering lengths for alkali gases makes evaporative cooling more efficient.
- The resonance lines of alkali atoms are readily accessible with diode and dye laser technology, compared with hydrogen which needed deep ultra-violet light source. The laser interaction provides sensitive spatial and temporal evolution of the atomic cloud.
- These interactions can be varied in a controlled manner through the choice of spin

state, density, atomic and isotopic species, and the application of external fields.

The formation of the Bose-Einstein condensate was confirmed by looking at the momentum distribution of the trapped atomic cloud. The momentum distribution can be obtained by turning off the traps and imaging the atoms in time of flight. The sudden narrowing of the momentum distribution is an indication of the macroscopic occupation of the ground energy state. Another change which occurs is the appearance of anisotropy in the atomic density distribution for some trapping configurations. Above the critical temperature for the condensate formation, atomic density distribution is isotropic as the kinetic energy is greater than the potential energy. Below the critical temperature, the kinetic energy is less than the potential energy, and the atomic density distribution tracks the anisotropy of the confining potential. Some have argued that a collection of BCS pairs is a form of Bose-Einstein condensate (BEC), this is strictly true only in the limit of strong interaction.

It should also be emphasized that being a superfluid does not mean the system is a condensate. Even though superfluidity and Bose-Einstein condensates are closely related, there remain subtle differences between the two phenomena. For example, in a uniform two dimensional system, a condensate cannot exist, though a superfluid state can exist at low enough temperatures. This transition is the Berezinskii-Kosterlitz-Thouless (BKT) transition, when thermal excitations break the vortex anti-vortex pairs formed at lower temperature [18]. It was only later that the existence of a condensate in 2d systems was shown for non-uniform potentials like a laser trap [19].

1.1 Overview of Fundamental concepts

1.1.1 Order parameter

The microscopic theory of large many body systems usually does not exist. A phenomenological approach is subsequently taken to study these systems by combining the important physical parameters into a field variable, often called the order parameter. Two common examples are the displacement field of ions from their mean position in a crystal and the local magnetization in a magnet. At a given point in the magnet, the sum total of all the fields from the local electrons decide the local magnetization. Taking into account all the local electrons is intractable, so an effective magnetization $M(x)$ is attached to a small region. The order parameter can be a vector, and all the physical variables can be mapped into it. For a system in equilibrium, the order parameter is uniform. When subjected to an external perturbation, the uniformity of the order parameter is broken and the internal dynamics of the system cause gradients in the order parameter. The gradient of the order parameter is an indication of the kinetic energy present in the system as the velocity is directly proportional to the gradient of the system.

This approach has been used to study both superfluids and superconductors, using the Gross-Pitaevskii equations for superfluids and Ginzburg-Landau equations for superconductors, as mentioned previously. The GL equations assume that the transition to superconductivity is a second order phase transition. After writing the free energy of the superconductor near the critical temperature, a minimization of

the free energy yields the GL equations. The Gross-Pitaevskii equation is obtained using Hartree-Fock and the pseudo-potential approximations. The Hartree-Fock approximation means that the many body wavefunction can be written as the product of single particle wavefunctions. The pseudo-potential means interaction arises due to contact interactions. The square of the amplitude of the order parameter gives the density of the quantum degenerate particles.

1.1.2 Healing length

The healing length is the characteristic length scale over which a macroscopic wave function returns to its background value after being subjected to a density perturbation. This definition holds true for both superfluids and superconductors. For a condensate, the healing length ξ is given by:

$$\xi = \sqrt{\frac{1}{8\pi n a_s}}, \quad (1.1)$$

where n is the number density and a_s is the s-wave scattering length. This length scale is obtained by comparing the kinetic energy to the interaction energy for a condensate.

1.1.3 Quantized Persistent currents

A counter-intuitive feature of superfluids is the presence of metastable persistent mass current states. Typically, a closed loop system is deployed to study these states since the other alternative is to set up a large 1d system, which is experimentally unfeasible. The most common of all closed loop geometries possible is the

toroidal trap, since the azimuthal symmetry allows the superfluid dynamics to be cast into a 1d problem. In this thesis, we will concentrate on toroidal traps. Since the superfluid can be assigned a macroscopic wave function (or an order parameter), the laws of quantum mechanics have to be satisfied. The wavefunction at a given location is single valued, so the phase drop in one complete rotation around the circumference in the absence of a weak link (density perturbation) can only be in integral multiples of 2π . This integer is called the winding number or the circulation state of the superfluid. This means that a superfluid in a toroidal geometry can only exist in states that have discrete angular momentum, irrespective of the velocity of a mechanical stirrer moving through the fluid. This is unlike a classical fluid, which can exist in a continuum of angular momentum states and will move with the same velocity as an external stirrer provided it is given enough time to reach equilibrium. The angular momentum spacing $\Delta\omega$ between different circulation states is decided by the mean radius of the toroidal trap:

$$\Delta\omega = \Delta n\Omega_0 = \Delta n \frac{\hbar}{mR^2} \quad (1.2)$$

where $2\pi\hbar$ is Planck's constant, m is the mass of a superfluid particle and R is the mean radius of the toroidal trap.

In the presence of a density perturbation in the toroidal trap, the phase drop across the density perturbation has to be taken into account. The phase drop across a density perturbation for a given current is called the current-phase relationship, and is helpful in characterizing the transport properties through the density perturbation. A density perturbation is commonly referred to as a tunnel junction if the length

scale if less than the healing length, and a weak link if the length scale of the density perturbation is much more than the healing length. The current phase relationship for a tunnel junction follows a sinusoidal relationship, while the relation is linear for a weak link. When the length of the density perturbation is between the tunnel junction and the weak link regime, the current phase relation can be modeled using a sum of a linear and a sinusoidal term [20].

1.1.4 Modeling superfluid flow

A useful concept to visualize the flow of a system described with a quantum mechanical wavefunction is the probability current, which is the flow of probability per unit time. The analogue of probability current in classical hydrodynamics is the mass current. If the wavefunction (ψ) is expressed as the product of a real amplitude R and a complex phase S ($\psi = R \exp(iSt)$), the probability current will become,

$$\frac{\partial \psi}{\partial t} = \frac{|R|^2 \nabla S}{m} \quad (1.3)$$

where m is the mass of a particle and t is the time. This transformation is known as the Madelung transformation [21]. This implies that any current is proportional to spatial derivative of the phase. In other words, a gradient of phase is necessary to sustain a probability current for a velocity field to exist. This means that the superfluid flow is irrotational like an ideal fluid. So a superfluid follows Euler's equation of an ideal non-viscous fluid, unlike a normal fluid with viscosity which follow the Navier-Stokes law. A simply connected superfluid can sustain angular momentum only by admitting line defects (vortices). The superfluid cannot sustain

solid body rotation, but a fluid with viscosity can.

1.1.5 Critical velocity and phase slips

A crucial difference between classical fluids and superfluids is the absence of viscosity in superfluids under ideal circumstances. An external object moving through a classical fluid will experience a drag force irrespective of the relative velocity between the external perturbation and the background fluid. On the other hand, an external object moving through a superfluid will experience no dissipation until the relative velocity between the superfluid and the stirring object exceeds a critical value, which is called the critical velocity. Once this critical velocity is exceeded, excitations are created in the superfluid. This creation of excitations can only occur if this event is allowed energetically. Landau used this argument and a Galilean transformation of energy and momentum of the superfluid to derive an expression for the critical velocity. If we assume that the energy and momentum of the superfluid in one frame is E_s and P_s respectively, then they are related to the energy and momentum in a second frame E'_s and P'_s by the following relations (we assume a relative velocity of V between the two frames and the mass of the particle to be m):

$$P'_s = P_s - mV \tag{1.4}$$

$$E'_s = \frac{(P_s - mV)^2}{2m} \tag{1.5}$$

Now let us assume that the first frame is the laboratory frame and the second

frame is the frame co-moving with the fluid, so the relative velocity is given by $-V$. We also assume that the ground state energy of the superfluid in the laboratory frame is $E_s = P_s^2/2m$ and an excitation with energy ϵ_0 has been created in the system. In the laboratory frame, the energy of the superfluid and the excitation is $E_0 + \epsilon_0$. In the second frame co-moving with the fluid, this will appear as:

$$E'_s = \frac{(P_s + mv)^2}{2m} + \epsilon_0 = E_s + \epsilon_0 + P_s v + \frac{1}{2}mV^2 \quad (1.6)$$

The above equations show that the creation of an excitation will increase the energy of the superfluid by ϵ_0 in the laboratory frame and by $\epsilon_0 + P_s v$ in the fluid frame. If the net change in energy is negative, then there will be a creation of excitations in the superfluid. Mathematically, it can be written as:

$$\epsilon_0 + P_s v < 0 \quad (1.7)$$

So an excitation has the most probability of being created in a region where the ratio of energy dispersion and the momentum magnitude is a minimum. This is the Landau's definition of the critical velocity:

$$v_c = \min \left(\frac{\epsilon_0}{P_s} \right) \quad (1.8)$$

The Landau criterion makes no assumption on the underlying mechanism which causes the excitation. The critical velocity for creating excitations in uniform systems is the Bogoliubov sound speed. The presence of a trapping geometry or non-uniformity brings down the critical speed for creating excitations. Feynman considered the case when the leading mechanism for energy dissipation in the superfluid system is the creation of vortex anti-vortex pairs. He considered the case when

a superfluid moving at constant velocity v through a channel of constant width d into a reservoir with a much larger width. There is a sharp edge where the channel and the reservoir meet. As the superfluid flows in the reservoir which has a much larger cross-sectional area, the velocity vector of a part of the superfluid may change direction. This momentum change is most likely to occur at the sharp edge. When this happens, vortices are shed to stabilize the flow. Thus the sharp edge serves as a nucleation point for vortices. Far away from the edges, these vortices decay into phonons and the energy is dissipated. By comparing the kinetic energy of fluid moving through the channel to the kinetic energy of the flow field of the vortices and anti-vortices, the critical velocity v_c will be:

$$v_c = \frac{\hbar}{md} \ln \left(\frac{d}{\xi} \right), \quad (1.9)$$

where $2\pi\hbar$ is the Planck's constant, m is the mass of one superfluid particle and ξ is the healing length of the condensate.

Another common geometry where the critical velocity can be estimated is when an obstacle is moved through a superfluid. In ref [22], the authors studied the effects of placing a hard disc in a superfluid with a constant relative velocity between the bulk superfluid and the disc. By assuming that the disc is impenetrable, the quantum pressure term can be neglected and the velocity at the surface of the disc is twice the velocity of the bulk superfluid. For this geometry, the authors found a critical velocity of $\sqrt{\frac{2}{11}} c_s = 0.42 c_s$, where c_s is the sound speed in the bulk. This work also performed numerical solutions of the GP equations, and found good agreements between the critical velocity and the theoretical estimate.

After the creation of atomic Bose-Einstein condensates [16,17], a new platform to study superfluidity became available. Soon after, efforts were made to measure the critical speed of creating excitations in the condensate [23]. The experiment involved scanning an obstacle through an elongated, simply-connected condensate. This geometry along with tight vertical confinement ensured that the vortex dynamics was effectively 2d. The obstacle was created using a blue-detuned laser beam, as a blue detuned laser beam repelled the atoms in the condensate. The obstacle was moved through the condensate by using an acousto-optic deflector. The obstacle was moved through different amplitude and frequency through the condensate, the velocity of the obstacle was a product of the amplitude and frequency. The heating of the condensate was investigated by looking at the thermal fraction of the cloud. The heating in the condensate was observed only after the obstacle velocity crossed a threshold, allowing one to make comparisons to the previous numerical study [22]. The formula presented in [22] overestimated the critical velocity found in the experimental paper, which could be explained by the fact that the laser beam is not an impenetrable surface. The use of a Feynman type argument gives an answer which is two times less than the experimental value. This tells that the energetics alone cannot lead to creation of excitations, this creation has to be supported by the dynamics as well. It also tells us that the critical velocity is an excellent tool to investigate what the relevant excitation is for a given geometry that is responsible for dissipation. This work [23] also repeated the critical velocity measurements in an atomic gas which was at a slightly higher temperature than the transition temperature for condensation. In this thermal cloud, the critical velocity at which significant

heating was observed was more than the sound speed. This showed that changing the temperature modifies the critical velocity, but no detailed characterization as a function of temperature was made.

Another experiment on critical velocity in oblate condensates studied the dependence of critical velocity on the ratio of laser beam diameter to the healing length and the intensity of laser beam relative to the chemical potential [24]. The healing length was varied by changing the atom number or the trapping frequencies. The authors investigated the effect of a soft boundary on the critical velocity by varying the intensity of the laser beam from much lower than the chemical potential to much higher than the chemical potential. They found that the critical velocity first decreases as the laser beam is ramped to the height of the chemical potential as expected, and then it increases. This can be explained by the fact that as the laser beam becomes more like a hard boundary, the density near the laser beam approaches the hard cylinder value, and the critical velocity increases again. The same group also measured how an increase in temperature increases the rate of decay of vortices [25–27]. The study of critical velocity has also been made in toroidal geometries as well, something that this thesis is interested in. The first measurement of the critical velocity in a toroidal trap beyond which decay of persistent current states was observed in [28].

The idea that quantum degeneracy begins to break down if an experimental parameter exceeds a critical value is not restricted to the critical velocity of an obstacle in elongated and toroidal condensates. The critical velocity has been measured in other systems as well: the critical velocity in a BEC-BCS crossover was

measured by passing a moving lattice through a condensate [29]. Similar to the existence of a critical velocity in superfluid, critical magnetic fields exist for type II superconductors, which allow the formation of magnetic vortices in the bulk of the superconductor. This is in contrast to type I superconductors, which expel the magnetic lines through the bulk. Type II superconductors have two critical magnetic field, 1st critical field beyond which they allow magnetic vortices to enter the bulk of the superconductor and the second one in which the superconductivity ceases to exist.

1.1.6 Phase Slips

We have seen earlier that the complex order parameter can be defined by an amplitude and a phase. When the order parameter of a superfluid approaches zero, the phase of the order parameter may show a sudden jump in multiples of 2π . These phase jumps are accompanied by either an excitation leaving or entering the system. The phase slip events are incoherent and provide a mechanism for superfluid and superconductors to dissipate energy even below their transition temperature in response to an external perturbation. For a superfluid, the external stimulus could be rotation or relative motion, while it could be magnetic fields in type II superconductors. These phase slips events are driven by thermal fluctuations at temperatures close to the critical temperature and by quantum fluctuations in the limit of low temperatures [30].

1.1.7 Hysteresis, energy landscape and particle interactions

A physical system is said to exhibit hysteresis when the response of the system is dependent on the history of the system. In other words, the response of the system to an external perturbation does not follow a strict one to one correspondence. This happens when for a given set of physical parameters, there exists multiple energy minima for the system. A common example is a ferromagnet. If we begin with a ferromagnet present in a zero magnetic field, the ferromagnet has an arbitrary magnetization direction, as all the spins inside the ferromagnet are oriented in a random direction without an external bias field. When the ferromagnet is placed in a strong magnetic field, the magnetization of the ferromagnet changes and tracks the external field. When the external magnetic field is removed, the magnetization of the ferromagnet does not change back to its original state, but continues to point in the same direction as the external field. Thus at zero field, the magnetization of the ferromagnet has multiple solutions, and the response depends on the history of the material. An abstract way to look at this is by defining the energy landscape, which is a mapping of all possible configuration of a system and the energy associated with them. For a ferromagnet, by changing the magnetization, different parts of the energy landscape are accessed with the magnetization as the control parameter.

We have seen earlier that superfluids in toroidal traps can sustain persistent current states. When we introduce a relative velocity between the superfluid and the toroidal trap (in case of superfluid helium physically moving the trap, or for a condensate moving a laser beam through it), the superfluid will at first be stationary

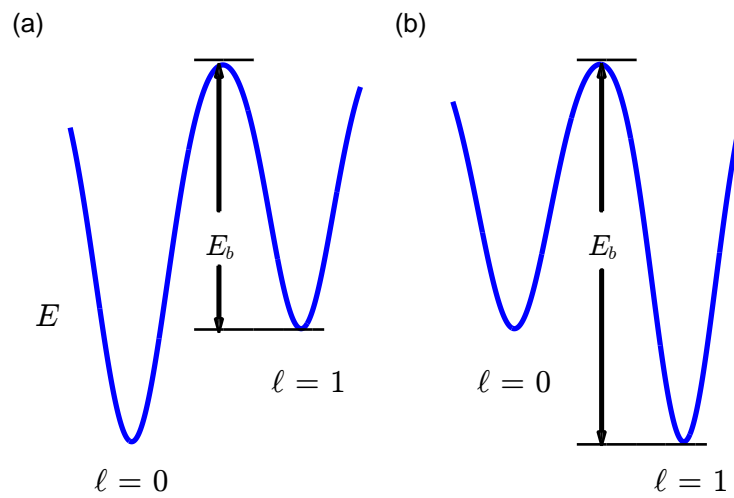


Figure 1.1: The energy landscape for a toroidal superfluid. In (a), the rest state $\ell = 0$ is the global energy minimum. In (b), the first circulation state $\ell = 1$ is the global energy minimum as an external rotating perturbation has been introduced in the system.

for velocity below v_c . At high enough relative velocity, the superfluid makes a transition to a persistent current state, and remains in this persistent current state even after the relative velocity between the trap and the superfluid is set to zero. Thus at the state of zero relative velocity, the superfluid can be in a state of rest or in a persistent current, depending upon the history of the system. Also, if one wants to return the superfluid to rest in the lab frame, the trap has to be rotated opposite to the circulation state. Hence we can view superfluidity as a hysteretic response to rotation. When viewed in terms of the energy landscape, the controlling parameter is the rotation speed and the circulation states of the superfluid are the minima of the system. When there is no circulation, the rest state is the lowest energy state, while imposing an external rotation can make the persistent current state lower in energy compared to the rest state (fig. 1.1).

By looking at figure 1.1, we see that the hysteresis is enabled by existence of energy barriers between the multiple local minima present in the energy landscape. A persistent current in the lab with no external rotation needs to be supplied with some energy so it can overcome the energy barrier and decay to the ground state, which is the rest state. Let us conduct a through experiment: we assume that all the particles in the superfluid are in the persistent current state $\ell = 1$, and there is just enough energy for one particle to overcome the energy barrier and move to the rest state $\ell = 0$. When this happens, the energy of the particle making the transition decreases, but the system pays a penalty in that the interaction energy decreases with the loss of a particle. If the interactions between the superfluid particles are strong enough, the loss of one particle from the $\ell = 1$ ends up increasing the total

energy of the system. In the absence of inter-particle interactions, a transport of one particle from state $\ell = 1$ to $\ell = 0$ lowers down the energy of the system, and is favored. This shows the key role played by inter particle interactions in stabilizing a persistent current state. In the work by [31], imperfections of the toroidal confinement were considered. A superfluid can move through these imperfections without any dissipation as the superfluid can screen out the impurities by a spatial change of the wavefunction, unlike an ordinary fluid. However, in ref [31], it is shown that if the inter particle interaction strength is less than the strength of the imperfections, no hysteresis and superfluid behavior is possible.

Hysteresis loops are also present in other physical systems. Hysteresis loops have been found during numerical investigations of Bloch waves for a condensate trapped in an optical lattice [32]. This work found that at high enough atomic densities, the lowest Bloch band showing the energy as function of lattice quasi-momentum becomes triple valued near the Brillouin boundary, giving rise to a “swallow loop” or hysteresis. Similar multi valued solutions were also found in two level non-linear Landau-Zener tunneling when the interaction strength was more than the coupling strength [33]. Hysteresis has also been observed experimentally. In superconductors, the current phase relation of an RF-SQUID was observed, which was found to be multi-valued [34]. The first demonstration of hysteresis in ultracold gases in a toroidal trap was given by [35].

1.2 Relevance of this work

1.2.1 Previous work done

The sodium ring lab has been studying the superfluidity of Bose-Einstein condensates in toroidal traps for the past decade. Several advances in the understanding of toroidal superfluids had been made before I joined the lab:

- The first demonstration of a persistent current state in an all optical toroidal trap and the use of a tunable weak link to control the current at the single quantum level was presented in [36]. The use of an all optical toroidal trap eliminated previous limitations in hybrid magnetic and optical traps [37,38], making lifetimes up to 40 s possible. This optical trap was created by superimposing red-detuned Gauss beam and a Laguerre-Gauss (LG_0^1) beam at 1064 nm. This potential also made the atomic distribution around the ring more uniform, with a atomic density distribution variation corresponding to a tenth of the chemical potential around the ring. There was a development of a new imaging technique called the partial transfer absorption imaging (PTAI), which gave more accurate information of density variation around the ring, as only a fraction of the atoms were transferred to a state resonant with the imaging light. Prior to this method, the high optical density of the condensate made it impossible to determined the density inhomogeneity around the ring. The critical velocity for creating excitations in the system was found to be 0.6 times the local sound speed.

- Observation of phase slips between persistent quantized circulation states was shown in [39]. A phase slip can be defined as a discontinuous phase jump in the condensate wave function. The phase slips were induced by rotating a weak link around the ring. This density perturbation was created by moving a blue detuned elliptic laser beam around the ring using a 2-axis acousto-optic deflector (AOD). The same AOD was used to imprint circulation states on the superfluid. This experiment was the atomic analog of the RF-superconducting quantum interference device (SQUID). The work also estimated the critical angular velocity for a circulation state change for a given weak link strength.

- First demonstration of hysteresis in an ultracold atomic gas system was made in [35]. In this work, the critical velocity for a transition from the circulation state 0 to 1 and then the transition state from 1 to 0 was measured respectively. The difference between these two circulation states normalized to the quantum of circulation gives the experimental size of the hysteresis loop. A theoretical estimate of the hysteresis loop was made by using the sound speed as the critical velocity. There was significant discrepancy between the experimental and theoretical values. This was attributed to the finite temperature effects, but the experiment lacked the ability to go down to lower temperatures, so the effect between hysteresis loop size and temperature could not be explored.

1.2.2 Results of this thesis

From the previous results, there remained unanswered questions on superfluid dynamics in toroidal traps. This thesis attempts to answer some of those questions. In this thesis, using both experimental and theoretical tools, we investigate multiple phenomenon related to BECs. The various experiments which have been explained in the individual chapters in this thesis are introduced below:

- **Determining the current phase relationship of the weak link:** The weak link in quantum degenerate systems allows coherent flow through them, unlike classical systems. This holds true for both superfluids and superconductors. The quantum transport properties through a weak link can be described by a single function called the current phase relation, i.e. the change in the phase of the wave-function across the weak link for a given current. This function is the analog of current-voltage relationship through a classic resistor. In the work mentioned previously [39], the current phase relation of the weak link in the superfluid was assumed to be sum of a linear and a sinusoidal term. While the experimental data gave good agreement with the theoretical model, there was no way to determine the current phase relationship directly. This problem was solved by using the target trap. Usually, the weak link is turned off before imaging in time of flight when the superfluid circulation state is to be determined. For determining the current phase relationship, the weak link is kept when the atoms are released in time of flight and then imaged. The displacement of the fringes at the weak link location is recorded, and by comparing to the spatial

spacing between two fringes (which corresponds to a phase jump of 2π), the current phase relation is obtained. This technique is very general, and can be extended to study of tunnel junction and excitations in the toroidal superfluid.

We also investigate the dynamics of the formation of spirals after release from the target trap. On the experimental side, the interference pattern after release from the target trap is imaged to multiple times of flight. On the theoretical side, the interferometer is characterized by placing a single particle in the interferometer, which exists in the superposition state of the toroidal and the disc state. This single particle picture can explain the formation of spirals. Also, the effect of mean field effects on the expansion dynamics is interrogated, and we found that mean field energies drive the expansion faster compared to the non-interacting case. More details can be found in chapter 3 and refs. [2,3].

- **Energy landscape of an atomtronic SQUID:** The excitation spectrum and the energy landscape of any system provide important information on the dynamics of the system when subjected to an external force. We probed the system using a harmonically driven weak link (density perturbation), both in position and intensity. The periodic movement of the weak link through the superfluid launches phonon wavepackets in the superfluid, which also display a periodic wavepacket. Collisions between shock waves were also observed. More details can be found in chapter 5 and refs. [4].

- **Development of metrological tools:** Any experiment on persistent current

states depends on the correct characterization of the persistent current state. The persistent current state can be measured by the presence of a hole in the atomic density distribution in the time of flight measurement, while the size of the hole indicating the charge of the circulation. This method posed multiple problems. First, at higher angular velocities of the weak link, external vortices would enter the annulus, making it impossible to determine if the off-axis vortex entered from outside or if it the product of the decay of a highly charged vortex. The second problem was that every time the ring dimensions changed, the hole size calibrations had to be performed again. The third problem was that the hole size gave no information on the chirality of the superflow. To make the circulation state determination faster and unambiguous, we added a disc shaped potential concentric with the toroidal trap. The combined trap is called the “target trap”. The interference between the disc and the toroidal condensate creates concentric circles when the toroidal superfluid is at rest and spirals when there is a persistent current in the toroidal superfluid. The number of spiral arms in the interference pattern yield the persistent current state and their chirality determines the direction of the persistent current state. This method does away with the need of calibrations every time the trap geometry is changed.

Even through the above technique works extremely well, the method still requires releasing the atomic cloud in time of flight. If a particular applications requires continuous measurements of the persistent current state of a sample, the desired measurement is impossible as all the atoms are lost in the time of flight measurement. To solve this problem, we developed a minimally destructive, Doppler

measurement of the superfluid flow in-situ. The Doppler effect, the shift in the frequency of sound due to motion, is present in both classical gases and quantum superfluids. This detection is performed by imprinting phonon modes on the condensate. A persistent current will drag the phonon modes along with it. The circulation state can be determined by the precession of the density maximum around the ring. More details can be found in chapter 5 and refs. [40].

- **Effect of thermal fluctuations on superfluid decay and critical velocity:** This experiment looked at the role of thermal fluctuations on the decay of quantized persistent currents and critical velocity for creating excitations. A recent paper [41] investigated the decay of persistent currents using two computational approaches: Gross-Pitaevskii (GP) and Truncated-Wigner approximation (TWA) simulations. GP simulations are done at absolute zero, while TWA simulations take thermal fluctuations into account. It was found that GP simulations predicted a deterministic decay of the superfluid current on a time scale of milliseconds, while TWA simulations found that the decay of the supercurrent was stochastic. More details can be found in chapter 6 and refs. [6].

- **BECs as a test bed for cosmology:** Given the length and time scale of cosmological events, it is impossible to replicate these conditions in the lab. To negate this, ongoing research has focused on making analogies between cosmology and laboratory systems like superfluids [42, 43]. Unlike superfluid helium, BEC superfluids can be held in all optical traps which makes it easier to subject the BEC superfluid

to dynamic potentials. Using a digital micromirror device, we can change the mean radius of the toroidal confinement, forcing the superfluid to follow the optical potential. Since the natural speed of information transfer in a condensate is the speed of sound, an expansion of the optical potential at a speed faster than the speed of sound allows us to make connections to the early expansion of the universe. More details can be found in chapter 7 and refs. [44].

Chapter 2: Experimental details

The basics of laser cooling and trapping can be found in a textbook like [45], while details specific to our experimental setup can be found in an earlier thesis from our group [1]. In the six years since, multiple upgrades and procedural changes have happened in the lab for enhanced performance and stability. This chapter summarizes those upgrades and changes, and focuses on the experimental steps during data acquisition.

2.1 Experimental setup

Any experiment involving a condensate begins by cooling down an atomic beam. This atomic beam is generated from an oven. The cooled atomic beam is then trapped in a magneto-optical trap, transferred to a magnetic trap and then evaporatively cooled to get a condensate. The condensates made in our lab typically consists of about a million atoms. The heart of any Bose-Einstein condensate experiment are the vacuum chambers, magnetic coils and the laser systems:

- **Vacuum system:** Our vacuum chamber consists of two parts separated by a gate valve. On one side of the gate valve is the oven, with a typical pressure of 2×10^{-7} torr. On the other side of the gate valve is the main chamber, where the BEC is

created. On the oven side, sodium ampoules are heated to a temperature of 220°C, which is more than the melting point of sodium (96°C). A fraction of sodium atoms in the vapor state is extracted using a nozzle, which is kept at 330°C. The nozzle is kept hotter than the oven to prevent the possibility of lumps of sodium blocking the nozzle. The extracted sodium atomic beam points towards the main chamber. To lessen the workload on the ion pump pumping the oven side, a cold cup is used. This cold cup provides a surface for the for the sodium atoms to stick which could not make their way to the main chamber. The sodium atoms which stick to the cold cup no longer contribute to the vapor pressure on the oven side. The cold cup is cooled using Peltier coolers. The external surface of the Peltier coolers is cooled using water cooling, unlike the previous generation of the experiment which used air cooling.

On the other side of the gate valve is the main chamber, which has ultra high vacuum (UHV). This is the part of the vacuum where the sodium atoms are trapped, and evaporatively cooled to make a condensate. The condensate resides in the center of a glass cell. The pressure reading in the main chamber using a gauge controller is 8×10^{-12} torr, which gives a vacuum limited lifetime of ≈ 25 s.

• **Magnetic coils:** The magnetic coils have remained unchanged during my time here. We use multiple magnetic coils during our experiment. The Zeeman slower coils help in slowing down the atomic beam coming from the oven by canceling the shift in atomic resonances due to Doppler effect. The quadrupole field coils provide the quadrupole field necessary for magneto-optical trapping, and later for magnetic trapping using much larger currents. Our experiment also needs a reverse Zeeman

slower magnetic coil, to cancel the residual field of the Zeeman slower at the center of the glass cell. The last set of magnetic coils needed is the time orbiting potential (TOP) trap, which is necessary for evaporative cooling (see section 2.2).

- **Lasers:** The laser used for cooling and trapping the atomic beam is a TA-SHG pro model from Toptica. This is a high power frequency doubled, tunable diode laser system, and provides us 1.2 W of power at 589 nm. The laser system is very easy to use, and needs a minimal warmup time of 5 minutes. This is a substantive improvement over the previous experimental configurations, which used two Coherent 699 ring dye lasers for generating the cooling and repump light, which at their peak performance would yield a combined total of only 0.8 W and were very cumbersome to align. The experiment also uses two other lasers: a 1064 nm laser and a 532 nm, both from IPG photonics. The 1064 nm laser is used for making a red-detuned sheet trap for vertical confinement (see section 2.2). The 532 nm laser is used for making a blue-detuned sheet, providing toroidal trapping potential and a laser beam to imprint circulation state on the atoms (see section 2.2).

2.2 Experimental steps

Here I briefly summarize the experimental steps currently used in our sequence:

- **Loading the magento-optical trap (MOT):** In this step, an atomic beam shutter between the source and the experimental chamber is opened up which allows a beam of hot sodium vapor aimed at the main vacuum chamber to come through a nozzle. A Zeeman slower and a reverse Zeeman slower is turned on, along with

a circularly polarized beam consisting of a beam of power of 40 mW red-detuned 390 MHz away from the D2 cycling transition of sodium. This D2 cycling transition is the transition between the ground state $|F = 2\rangle$ and the excited state $|F' = 3\rangle$. Mixed with this slower beam is another laser beam with repumping light tuned to the $F=1$ to the $F'=2$ transition and has around 20% the power of the slower beam (an energy level diagram of sodium atoms is shown in figure 2.1). The laser beams and the spatially varying magnetic quadrupole field necessary for a magneto-optical trap (MOT) is turned on simultaneously with the slower laser beams and coils. A typical MOT loading time in our experiment is 1.25 s, which can be increased or decreased depending on the number of atoms needed to run a particular experiment. We use a dark-SPOT MOT [46] configuration to increase the number of trapped atoms. The MOT repumper beam used in tandem with the MOT trapping beams is in the shape of a donut. Most of the sodium atoms are stored in the $F=1$ hyperfine state, which does not interact with the trapping beams.

• **Spin Polarization:** After trapping the atoms in a magneto-optical trap, we have to prepare to transfer the trapped atoms to a magnetic trap. For this purpose, the atomic beam shutter is closed down, and both the Zeeman slower and the reverse Zeeman slower magnetic coils are shut off. These steps are completed in 20 ms, during which time the power in the MOT beams is cut down by half, this stage is called the MOT handoff stage. Subsequently, the MOT repump beam is shut off by closing the repumper AOM and a shutter. With no MOT repumper light to pump atoms from the $F=1$ hyperfine state to the $F'=2$ hyperfine state, we can transfer the atoms trapped in the MOT to the $F=1$ hyperfine state. In the $F=1$ manifold,

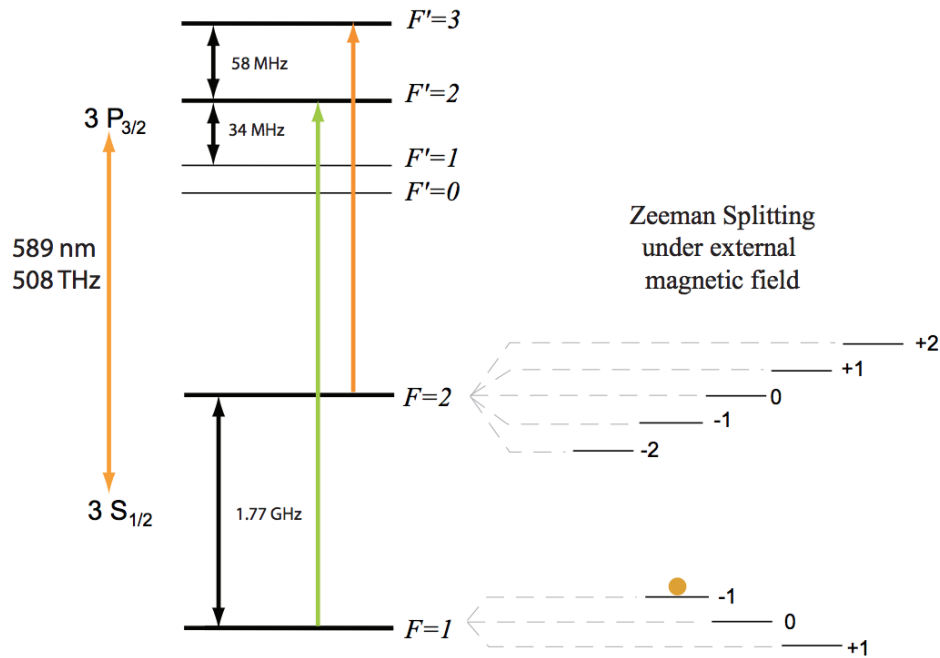


Figure 2.1: **This figure is taken from [1].** This figure shows the sodium D2 transition hyperfine structure. The $3S_{1/2}$ manifold makes the ground state and the $3P_{3/2}$ level makes the excited state manifold. The laser cooling and trapping is performed on the $F = 2$ to the $F' = 3$ cycling transition. An external magnetic field bias breaks the degeneracy of the hyperfine levels. The sodium atoms are transferred to the $|F = 1, m_F = -1\rangle$ state for magnetic trapping, which has been indicated by an orange dot.

the $F=1, m_F = -1$ state is magnetically trappable as it is a low field seeking state. While the $F=2, m_F = 1$ and $F=2, m_F = 2$ states are low field seeking states too, they are not used for magnetic trapping. There are two reasons for this: first we get a spin mixture in the trapped system and any non-stretched state like the $F=2, m_F = 1$ has a poor lifetime in a magnetic trap. This poor lifetime is a result of spin changing collisions, which may render an atoms in a spin state that is not magnetically trappable.

- **Transfer to magnetic trap:** Next, the current in the quadrupole magnetic field coils is ramped from 4.9 A to 82.5 A (the magnetic gradient is 1.2 G/(A-cm)), creating a deep magnetic trap for transferring the atoms from the MOT to this magnetic coils. In the next stage, we compress the quadrupole trap by ramping the current from 82.5 A to 250 A. This compressed quadrupole trap has a higher temperature but more importantly, a higher number density of atoms. This increased density will become important during the evaporation process, where elastic collisions at a fast rate are needed for the atoms to thermalize and cool down as radio frequency (RF) radiation induces forced evaporation.

- **Quadrupole RF evaporation:** The atoms in a magnetic trap are typically at a temperature of hundreds of μK . The phase space density under these conditions is still many orders of magnitude away from Bose-Einstein condensation. The atomic cloud can be cooled down further by using radio frequency (RF) induced evaporation. Evaporative cooling works on the following principle: in a given potential, the atoms having most kinetic energy can climb higher up the potential walls. If the potential depth is decreased, the most energetic atoms are lost, the remaining atoms

redistribute the energy by elastic collisions and the temperature of the remaining trapped atoms comes down. In our experiment, we lower down the walls of the trapping magnetic potential by sweeping the frequency of an applied RF field from 80 MHz to 10 MHz in 2.8 s using an Agilent 33250A function generator, with the amplitude kept constant at 632.5 mV. As the RF frequency is being swept, any atom that becomes resonant with the incident RF field undergoes a spin flip and is lost from the trap. As the RF frequency is being swept from higher frequency to lower frequency, the most energetic atoms lying at higher regions of the energy potential are lost first, which mimics evaporation. We apply RF radiation provided by an RF antenna which is powered by a 10 W RF amplifier.

- **TOP trap:** As we are cooling down the atoms, they lose kinetic energy. This implies that atoms have a greater probability of being found lower in the energy potential where they are trapped. One of the features of working with atoms trapped in a magnetic quadrupole field is the presence of a zero field in the center of the field distribution. As the depth of the magnetic field is turned down lower and lower to facilitate evaporation, the cooler atoms will have a greater probability of making their way to the lowest part of the energy potential, which is in a zero field configuration. Near the zero field, the atoms may experience random spin flips, which may send them into an anti-trapped state. This is detrimental to making large condensates, as the zero field in the magnetic trap allows the cooler atoms to escape continually. This loss can be prevented either by having a blue-detuned beam or by introducing a magnetic field bias. We did not choose the laser beam approach as aligning the laser beam to the magnetic field zero is not only difficult, but we also

have to contend with the fact that a blue detuned beam heats the cloud and that the position of the magnetic field may change during the day due to thermal cycling in the coils. We move the zero in the magnetic field by introducing two magnetic fields with an oscillation frequency of 20 kHz and 90 degrees out of phase with each other. These magnetic fields are created using two SRS frequency generators, whose signals are amplified using RF amplifier. As the magnetic fields are out of phase with each other, the resultant magnetic field keeps rotating at a speed faster than the trapping frequency of the atoms, which means the atoms are continually trying to track the ever changing field zero, but never reach it. This ensures trapping of even the cooler atoms in the magnetic trap. This setup is called the time-orbiting potential (TOP) trap. The TOP trap is turned on after the evaporation in the quadrupole trap is complete.

- **Death circle evaporation:** In this step, the strength of the magnetic field creating the TOP trap is instantaneously reduced, which means that the atoms with higher kinetic energy residing far way from the trap minimum are lost, which reduces the average kinetic energy in the trap leading to lower temperatures after thermalization.

- **TOP trap RF evaporation:** In this step, a forced evaporation of the atoms trapped in the TOP trap is carried out using RF radiation. The mechanism of this evaporation as the evaporation in the quadrupole trap. In this step, the RF knife edge from 13.6 MHz to 9.6 MHz. We are able to reach to temperatures down to 500 nK in the TOP trap, which is very close to the critical temperatures needed for condensation.

• **Transfer to red-detuned dipole trap and set the z bias:** The next step in our experimental sequence is to transfer the atoms from the TOP trap to an optical dipole trap. An optical dipole trap relies on the polarizability of atoms induced by electric fields to confine atoms. The red-detuned trap used in our experiment is produced using laser light at 1064 nm. The output light from a fiber is collimated using a lens, the resultant Gaussian beam is made incident on a cylindrical lens which elongates the Gaussian beam along a line into a “sheet”. This elongated beam is focused on to the atoms using a spherical lens. This setup is discussed in more detail in section 2.4.2. An optical dipole trap has multiple advantages. First, it can trap atoms independent of the magnetic substate of the atoms. Also, unlike a MOT which operates very close to resonance, the dipole trap is close to 500 nm detuned from the optical transition, which cuts down the scattering rate. We perform another stage of evaporation in the dipole trap by lowering the optical power. The power is ramped exponentially from its initial to final value in 3 s. This brings the cloud to a temperature of 100 nK. At this temperature, the thermal component constitutes a very small portion of the atomic cloud. A bias field of 1 G is kept on during evaporation, which is used to define the quantization axis of the atoms. Defining the quantization axis of the condensate is important for maintaining purity of the condensate and estimating the cross-sectional area of the atoms for imaging purposes. A figure of the experimental sequence showing various stages of evaporation has been shown in appendix A.

Our red-detuned dipole trap has several limitations. The first limitation comes from the shape of the trap. The red-detuned trap has an elongated shape to max-

imize the capture of atoms from the magnetic trap. For a given laser power, the trapping volume of an elongated laser beam is more than the volume of a focused Gaussian beam. This additional volume makes evaporative cooling sub-optimal, and the lowest temperature we can reach is 100 nK. The second limitation of our red-detuned dipole trap comes from etaloning in the glass cell. The main vacuum chamber is made from a glass cell. As the laser beam for making the dipole trap propagates, some of the laser light is back-reflected from the internal surface of the glass chamber. The back reflected light may interfere with the incoming laser light and make standing waves. The presence of such standing waves can easily be seen by presence of density striations in the atomic density distribution. These density modulations are unwanted. We minimize the affect of these modulations by ensuring that the red-detuned dipole trap enters the glass chamber at Brewster's angle.

- **Turn on the crossed dipole trap:** The atoms trapped in the red-detuned trap are in oblong shape with the maximal spatial extent of around 150 microns. We need this spatial dimension to ensure effective transfer of atoms from the TOP trap to the dipole trap. However, the ultimate goal is to trap atoms in a ring with a mean radius of 22 microns to study superfluidity. To make sure that this transfer occurs with maximum efficiency, we turn on a crossed red-detuned beam with similar beam diameter to the ring trap we have ultimately in mind. This results in atoms being confined in their entirety to a diameter of 50 microns.

- **Transfer to blue-detuned vertical trapping dipole trap:** To overcome the problems in the red-detuned sheet like interference fringes due to etaloning and to go to lower temperatures when needed, we have an additional optional step. We can

choose to transfer the atoms to a blue-detuned dipole trap where a blue-detuned dipole beam is passed through a pi-phase plate. Destructive interference leaves a notch in the beam, where atoms can reside. Since such a dipole trap can only provide vertical confinement, the crossed dipole beam is turned on along with the blue-detuned dipole beam at first. A key difference between a blue-detuned trap and a red-detuned trap is that the temperature of atoms in a blue-detuned trap will decrease if the intensity of the laser beam is increased, unlike a red-detuned trap. We have seen that for our experiment, the temperature of a blue-detuned trap decreases from 40(12) nK to 30(10) nK as the vertical trapping is changed from 518(4) Hz to 974(7) Hz. On the other hand, the temperature of a red-detuned trap increases from 85(20) nK to 195(30) nK as the vertical trapping is changed from 520(10) Hz to 985(4) Hz [6].

- **Transfer to toroidal trap:** Once the crossed dipole beam is turned on, the trapped atoms are disc shaped. The toroidal potential is turned on to full power using a linear ramp, followed by turning off the crossed dipole trap. The power used for the toroidal trapping potential is typically 1.5 times the spillover point. The spillover point is defined as the minimum power needed to transfer the entire condensate in the crossed dipole trap to the toroidal condensate.

- **Experiments and imaging:** To collect data after experiments, we use absorption imaging [47]. The atoms in the optical trap are in the $|F = 1, m_F = -1\rangle$ state. We use microwave radiation to transfer a fraction of the atoms to the $|F = 2, m_F = -2\rangle$ state, where they are imaged using a probe light. This variant of absorption imaging, where we only image a small fraction of the atoms is called the partial transfer

absorption imaging (PTAI) [1, 48]. We use PTAI to get an accurate description of the azimuthal density profile of the toroidal potential. Imaging all the atoms in the toroidal potential results in a high optical density. At these high optical densities, the density variations cannot be detected with high fidelity [1].

2.3 Electronics development

This section describes the various electronics projects executed by me for a more safe and reliable operation of the experiment.

2.3.1 Vacuum and Temperature Interlock

The vacuum chamber used in our laboratory was divided into two parts by a gate valve, one part was the oven side and the other part was the main chamber side. The oven side had the sodium source, and the main chamber side was where the BEC is made. The development of a vacuum interlock to separate the main vacuum chamber from the oven side was needed to prevent the contamination of the vacuum in the main chamber, should a leak occur on the oven side. This development was necessitated by an unfortunate incident in our laboratory, where a power outage and subsequent power restoration left a turbo pump disabled, poisoning the vacuum chamber with oil from the roughing pump. A interlock that would shut down the gate valve in the case of a vacuum breach and then open up only after human intervention was needed. I designed an interlock to implement this safety feature (A schematic to implement this interlock is shown in figure 2.2. A detailed set of

instructions on operating this interlock is provided in appendix [A](#)).

This device was installed on the experiment after testing, and proved to be very helpful. In over 4 years of operation, we had several occasions when the interlock was called into play. In one event, the TEC (thermo-electric cooler) performance degraded, bringing the temperature of the cold cup to -3 C, this meant that occasionally a chunk of sodium would settle on the ion pump on the oven side, shorting the electrodes and rendering the pumping speed to zero. This would cause the pressure in the oven side to rise by 5 orders of magnitude, so the vacuum interlock would shut down the gate valve. After baking the ion pump on the oven side, the deposited sodium on the ion pump would release and the pressure would come down to normal, but the gate valve would remain off till the clock button was hit.

A modification of the above circuit was made to monitor and interlock the temperature of the magnetic coils making the Zeeman slower of our experiment. Our Zeeman slower coil was only air cooled. If the duty cycle of the experiment was too fast, the slower would heat up and increase the pressure in the experimental chamber. To prevent this from happening, we wanted to turn off the slower coils should the temperature reach 50 C. We used a temperature switch as a signal to the flip flop and made a temperature interlock. The sensor used to generate a signal whether the temperature was above a threshold was generated by a thermo-couple switch with the part number LOVE TCS4011.

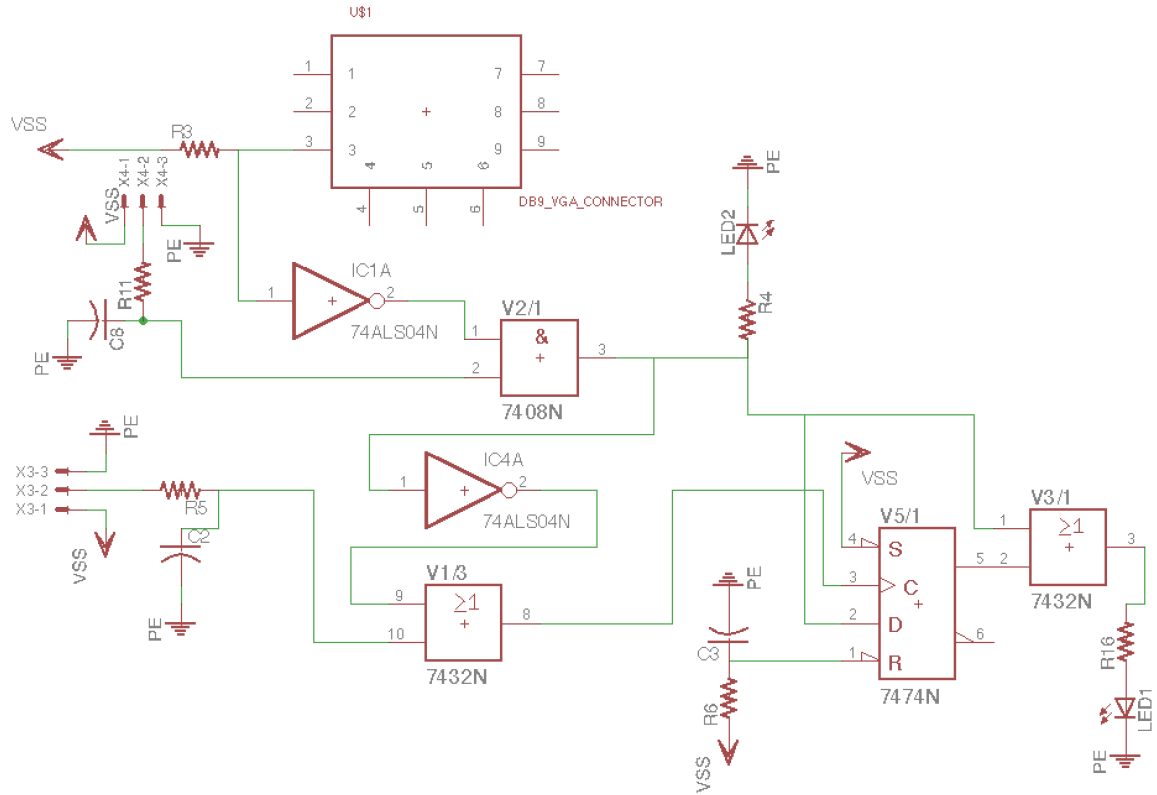


Figure 2.2: The schematic in this figure shows the implementation of a vacuum interlock. All the circuit components are digital, using components from the 7400 transistor-transistor logic (TTL) series. According to the naming convention: 7404 is a hex inverting gate, 7408 is a 2 input AND gate, 7432 is a 2 input OR gate and 7474 is a D flip-flop. The symbols VSS and PE denote a voltage of +5V and ground respectively. Any symbol beginning with R and LED shows a resistor and a light emitting diode respectively. The symbol DB9 shows the cable carrying info from the vacuum gauge controller to the vacuum interlock. Toggle switches are denoted by X3 and X4, X3 is the switch for disabling the interlock, while X4 is the switch for manually enabling the interlock again. The output of the AND gate V3/1 goes to the relay controlling the gate valve.

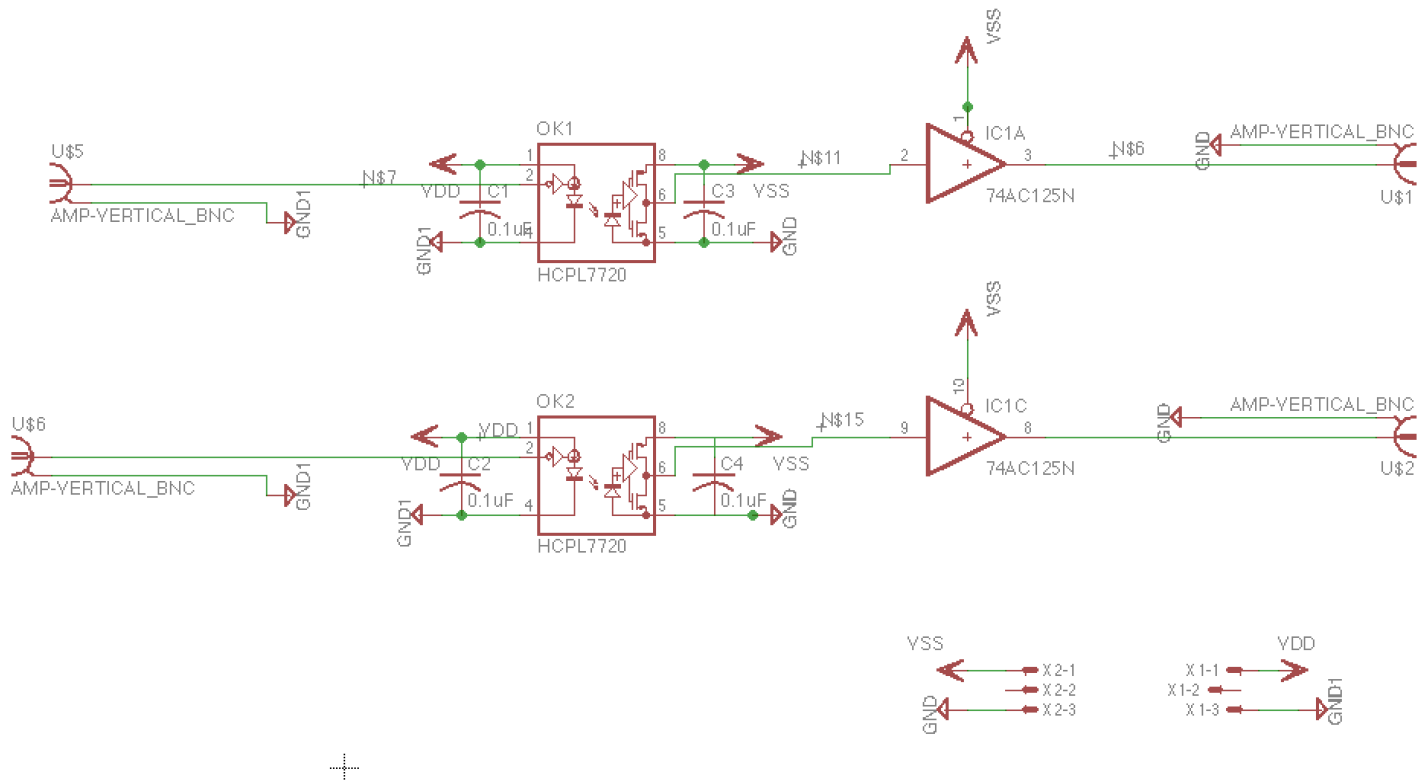


Figure 2.3: The schematic in this figure shows the implementation of a digital buffer. All the circuit components are digital. The input BNC signals $U\$5$ and $U\$6$ are shown to the left, while the output signals $U\$1$ and $U\$2$ are to the right. The optocouplers are depicted by the part number HCPL 7720. These optocouplers couple the input side to the output side optically, cutting down on the electrical noise and cross-talk between various channels. The part number 74AC125N shows a one input digital buffer, where the output tracks the input. The symbols VDD and VSS denote the +5V power supply to the input and the output side. The symbols GND and GND1 denote the ground connection to the input and the output side. The power supply to the input and the output side are kept separate to prevent noise coupling.

2.3.2 Digital Buffer

Efficient control of any experiment requires computer controlled switching on the scale of microseconds. These digital TTL signals are generated by a pulse blaster, a PCB board which creates multiple TTL signals. A breakout board is then used to send these signals to different BNCs for instrument control. There is a possibility of cross talk between various digital channels which may degrade the reliable performance of the experiment. A buffer box was build to prevent this electronic cross-talk from happening. A schematic circuit is shown in figure 2.3, which uses a combination of optocouplers (HPCL 7720) and digital buffers (74HC125). An optocoupler transfers signals by light, which prevents spurious voltages from affecting the system. A digital buffer on the other hand tracks the input if the control signal is held to high. Each signal line coming from the pulseblaster passes through a separate optoisolator, and two signals share one digital buffer. We saw no evidence of cross talk between two channels.

2.4 Optics Setup Development

2.4.1 Optical setup for ring potential

The main focus of thesis is to study superfluidity of a BEC trapped in a toroidal geometry. To get reliable experimental data, the toroidal potential needs to be stable and as smooth as possible in the azimuthal direction, so that irregularities in the potential do not dominate the physics that we want to study. We have gone through

several schemes to continually improve the quality of the toroidal confinement. Here are some of the techniques explored:

- **Diffraction grating and Vortex phase plates:** The first method of trapping sodium condensate in a toroidal confinement used a red-detuned laser beam. The toroidal red-detuned beam was first made by passing a Gaussian beam at 1064 nm through a diffraction grating. The second generation of the optical setup used an alternative method by passing the beam through a vortex phase plate. The vortex phase plate had a phase singularity, which converted a Gaussian beam to an Laguerre-Gauss LG beam. The phase singularity was generated by varying the thickness of a deposited polymer on a glass substrate, so different parts of the beam underwent different phase shifts when they were transmitted through the glass surface. Destructive interference created a hole at the center of the beam, which then propagated forward as a LG beam. The RPC photonics wave plate we use had multiple regions, each containing a phase singularity of varying charge. Each unique phase singularity could generate a beam with a different angular momentum beam (and a different hole size). This technique was abandoned as the azimuthal symmetry of red-detuned beams was sub-optimal.

- **Chrome deposited on glass:** The next step was to explore the symmetry of the potential created using a blue detuned trap. This was implemented by imaging a Gaussian beam transmitted through a glass surface that had a ring shaped chrome deposit. A beam transmitted through this amplitude mask has a hole in it the shape of a ring as the chrome surface is reflecting. This beam was imaged on the plane of the atoms. The atoms are repulsed by the blue-detuned light and they accumulate

in the dark regions, which is in the shape of a toroid. We have found that the potentials using a blue-detuned beam were smoother as compared to a red-detuned beam. This was because the atoms accumulated in the dark-regions, and thus are unaffected by the aberrations picked by a laser beam during propagation. Another advantage of this method was that new traps with various radii were created more easily, depending on the number on patterns created on a glass substrate. The disadvantage of this method was that focusing and the alignment of the toroidal trap with other traps is required every time a new geometry is chosen. This was very costly time wise, given that a replacement of the mask and alignment of the mask with other dipole traps could take hours. This also meant that we lacked the capability to dynamically change our potential. The blue-detuned light was at a wavelength of 532 nm.

• **Digital micro-mirror devices (DMDs):** The next advance in creating toroidal traps came with the arrival of digital micromirror devices (DMD) to make toroidal traps. This device is comprised of an array of microscopic mirrors, with one microscopic mirror corresponding to the pixel of an image to be displayed. The toroidal pattern is created after reflecting from the surface of a DMD. The mirrors can be turned by an angle of 4 degrees, which results in the light at the projection plane to be turned on or off. Since the device is digital, grayscale images are produced by half-toning. We have used both, devices DLP3000 and DLP7000 on our experimental setup, with the latter having more memory and faster upload rate of images, typically on the order of 500 μ s. This allows us to dynamically change the trap potentials to explore new physics, or program the image on the camera to make the

optical density distribution around the toroidal trap more uniform. We continued to use blue-detuned light for this iteration since it produces more uniform potentials. We have placed a DMD both in the imaging and the Fourier plane. We have used the DMD placed in the Fourier plane to create aberrations free potentials in our system. One caveat is that a DMD consumes more power than the methods described earlier, as most of the power is wasted in scattering (where the mirrors have been turned off) and diffraction into unwanted diffraction orders. For our experiment, only 10% of the light introduced in the DMD arm made its way to the plane of the atoms. The blue-detuned light was at a wavelength of 532 nm.

2.4.2 Red detuned dipole trap for vertical trapping

The red detuned optical dipole trap discussed in section 2.2 is used for storing the atoms after evaporation in a magnetic trap. The beam used for generating this potential is in shape of a sheet, generated by a cylindrical lens. The optical setup for shaping the red-detuned beam into a light sheet is shown in figure 2.4. The optical parts needed for making a light sheet include:

- **SM1Z:** This is a 2 axis translation stage from Thorlabs, on which an optical fiber is mounted. It is compatible with a 30mm cage Z-Axis. These two axis along with the base give us translational control of all the three directions. The optical fiber itself is from NKT Photonics with the part number LMA-PM-15FC / APC-PM-SMA 905. The fiber and the mounting stage are shown as ‘A1’ in figure 2.4.
- **LMH-10X-1064:** This is a high power MicroSpot focusing objective from Thor-

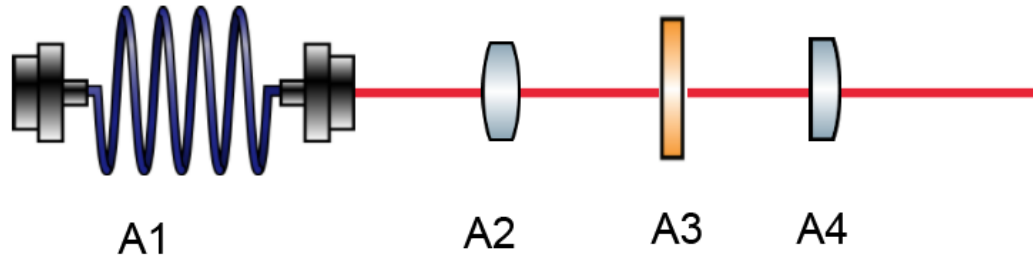


Figure 2.4: Setup for shaping a red-detuned Gaussian beam into a light sheet. The optical parts shown as A1,A2,A3 and A4 are a translation stage, focusing objective, half wave-plate and a cylindrical lens respectively. Their part numbers have been listed in section [2.4.2](#) .

labs, tuned to work at a wavelength of 1064 nm. The objective has a numerical aperture of 0.25, working distance of 15 mm and a magnification factor of 10. This objective collimates the beam coming out of the fiber. This objective is shown as ‘A2’ in figure [2.4](#).

- **WPH05M-1053:** This is a zero order half wave plate from Thorlabs, which is $1/2''$ in diameter. This is used to cleanup the polarization of the laser beam coming out of the optical fiber. This waveplate is shown as ‘A3’ in figure [2.4](#).

- **CLCC-25.4-20.3-1064:** This is a cylindrical plano-concave lens from CVI Optics. This lens has a focal length of -40 mm, diameter of 25 mm and a radius of curvature of 20.3 mm. This lens converts a Gaussian beam into an elongated beam (light sheet). This is shown as ‘A4’ in figure [2.4](#).

The light sheet is then steered by mirrors and then focused on to the atoms using a spherical lens of focal length 200 mm. All the optical parts listed above are mounted on a one axis translation stage. The entire assembly is placed in black cardboard box for safety. The red-detuned beam is intensity locked using scattered light.

2.4.3 Blue detuned potentials for vertical trapping

- **Optical setup:** As mentioned earlier, we use a blue-detuned dipole trap for vertical confinement (alternative called the blue-detuned sheet) when smoother potentials and lower temperatures are needed. When a red-detuned dipole trap is used for vertical confinement (alternative called the red-detuned sheet), atoms are transferred from the TOP trap to the red-detuned sheet. Atoms are cooled down further by evaporative cooling till the thermal fraction is negligible, the optical power of the red detuned is decreased in an exponential ramp. The condensate produced is transferred to a toroidal trap after turning on a crossed-dipole trap.

An evaporation sequence in a blue-detuned sheet differs from an evaporation sequence in a red-detuned sheet. We cannot perform an evaporation sequence and hold on to the resulting condensate in a blue-detuned sheet, as there is no radial confinement. To address this issue, a red-detuned crossed beam is also turned on during an evaporation sequence in a blue-detuned sheet. A condensate is produced by cutting down the power of the blue-detuned sheet and the crossed-dipole trap during an exponential ramp, which results in evaporative cooling. The condensate

can then be transferred to a toroidal trap. Note that we always perform the evaporation sequence when the atoms are present in a simply connected trap. We have observed that performing evaporation in a often results in spontaneous circulation states, which is undesirable.

The blue detuned sheet is generated by an IPG photonics fiber laser at 532 nm. The output light from a fiber is collimated and a cylindrical lens creates an elongated sheet beam. A schematic of the optical setup used to generate a blue detuned sheet trap is shown in figure 2.5. The part number of the optical components needed for the setup have also been indicated in figure 2.5.

• **Blue-detuned sheet alignment procedure:** The blue-detuned sheet has to be aligned to the red-detuned sheet for optimal transfer of atoms between the two atoms. As a first step, the pi phase plate is removed, and the collimating lens is adjusted till a sharp image of the sheet is formed on an auxiliary imaging camera. Then, the pi phase plate is but back in. The position of the red-detuned sheet is recorded on the horizontal imaging camera. The blue detuned potential sequence is run, and the position of atoms is recorded (see figures 2.6 anf 2.7 to know what a good alignment looks like). For alignment purposes, the atoms are released in time of flight by turning all other beams but the blue-detuned beam. There is no radial confinement, so the atoms expand radially. This allows us to measure the position of atoms in the blue-detuned trap with accuracy. If the blue-detuned trap is offset in position from the red-detuned trap, it can be moved in the right direction by adjusting the knobs of a steering mirror.

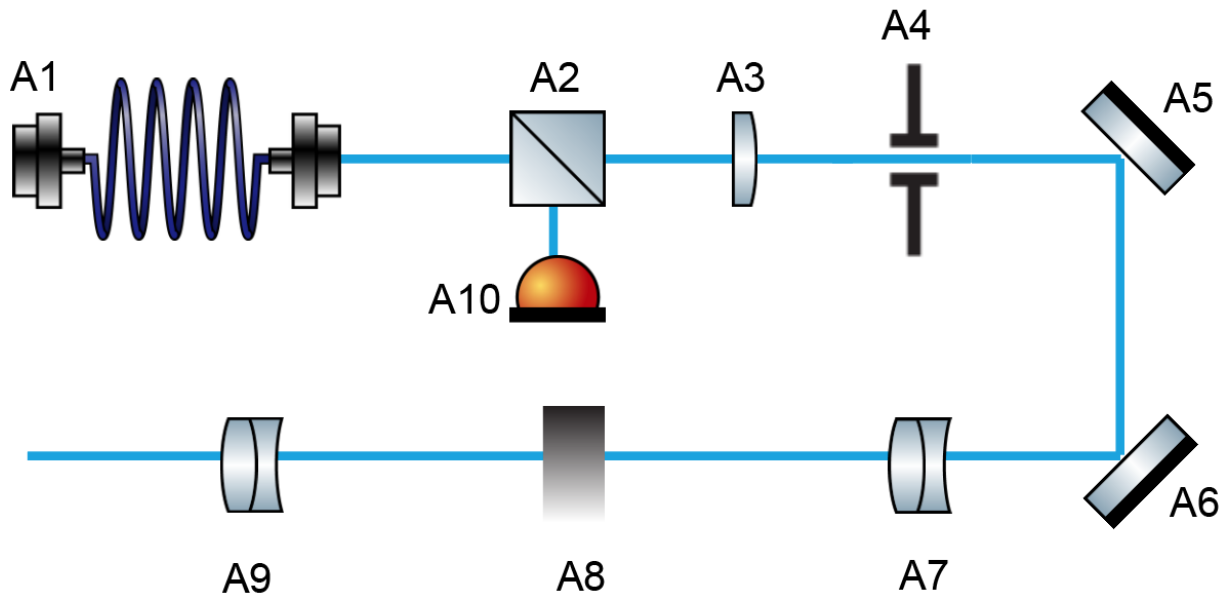


Figure 2.5: Optical parts labeled in the figure are: A1 is fiber mount with translational adjustments in both the x and the y axis (Thorlabs part number C110TME-A), A2 is a cage mounted polarizing beam splitter cube (Thorlabs part number CM1-PBS251), A3 is cylindrical lens of focal length 40 mm, A4 is an iris for alignment purposes, A5 and A6 are mirrors, A7 is an achromat of focal length 300 mm used to measure the power in the beam (Thorlabs part number AC508-300-A1), A8 is a pi phase plate, A9 is an achromat of focal length 200 mm and A10 is a photodiode to intensity lock the beam (Thorlabs part number PDA36A)

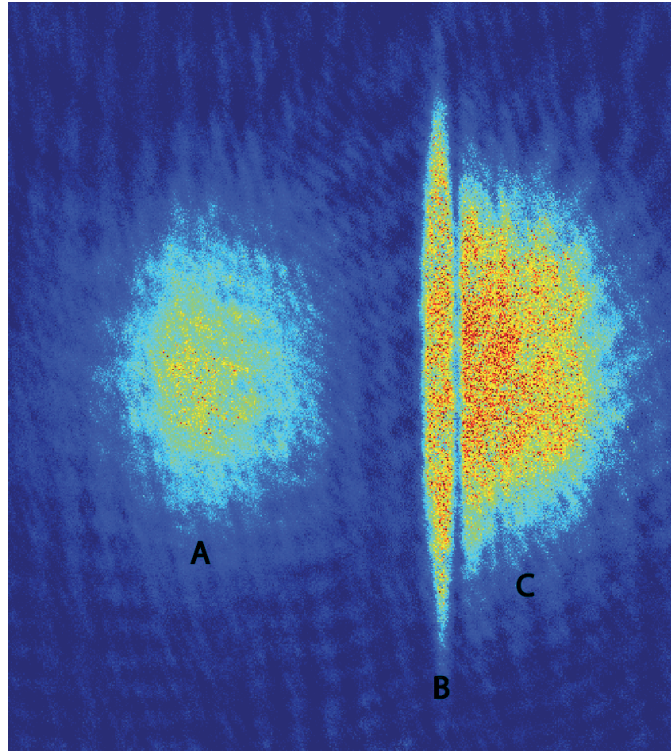


Figure 2.6: The above image is a false color absorption image of the atoms when they are are being transferred from the TOP trap to the blue-detuned sheet. This image shows a situation when the relative position of the TOP trap and the blue-detuned trap is adjusted for maximum transfer efficiency. The picture follows a false color scheme, dark blue and dark red represent regions of regions of lowest and highest atomic density respectively. In the picture above: three separate atomic clouds labeled as A,B and C can be seen. The atomic cloud on the left, shown as ‘A’, is a group of atoms that were transmitted through the blue-detuend sheet after being released from the TOP trap. The atomic cloud on the center, shown as ‘B’, is a group of atoms that were captured by the blue-detuend sheet after being released from the TOP trap. The atomic cloud on the right, shown as ‘C’, is a group of atoms that were reflected by the blue-detuend sheet after being released from the TOP trap. The gravitational field acts from the right to the left. This image was taken using horizontal imaging system.

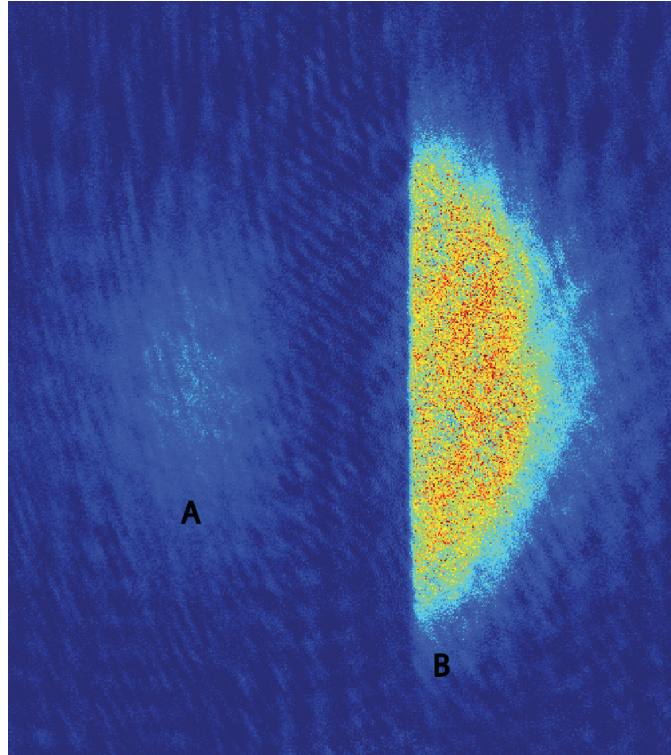


Figure 2.7: The above image is a false color absorption image of the atoms when they are being transferred from the TOP trap to the blue-detuned sheet. This image shows a situation when the relative position of the TOP trap and the blue-detuned trap is adjusted for minimum transfer efficiency. The picture follows a false color scheme, dark blue and dark red represent regions of lowest and highest atomic density respectively. In the picture above: two separate atomic clouds labeled as A and B can be seen. The atomic cloud on the left, shown as ‘A’, is a group of atoms that were transmitted through the blue-detuned sheet after being released from the TOP trap. The atomic cloud on the right, shown as ‘B’, is a group of atoms that were reflected by the blue-detuned sheet after being released from the TOP trap. No atoms were trapped in the sheet trap, and hence cannot be seen in the time of flight images. The gravitational field acts from the right to the left. This image was taken using horizontal imaging system.

2.4.4 Imprinting a circulation state

In the previous subsection, we described the methods to obtain a toroidal condensate. We use this trapped condensate to study superfluidity. One of the important questions in superfluidity is the decay of persistent currents. The study of persistent current decay requires us to have the ability to imprint circulation states deterministically on the toroidal condensate. The earlier generations of the experiment used a Raman transfer process between a LG_0^1 and a Gaussian beam to transfer the toroidal condensate from one circulation state to another [49]. However, all the experiment in this thesis use a focused, blue-detuned laser beam to imprint a circulation state. This laser beam is moved around the toroidal potential using a two-axis acousto-optic deflector (AOD). This AOD is used to move the laser beam around the toroidal potential typically at an azimuthal frequency of 1 Hz and at a radial frequency of 8 kHz. The azimuthal frequency is chosen to transfer all the atoms from the ground state to the 1st circulation state. The radial frequency is chosen to create a time averaged potential, which can mimic the motion of a mechanical object dragging the superfluid across the cross-section of the toroidal potential.

Chapter 3: Interferometric Measurement of the Current-Phase Relationship of a Superfluid Weak Link

In this chapter, we study how the circulation state of the persistent current can be determined interferometrically and show a measurement of the current phase relationship for a weak link inserted in a toroidal condensate. This chapter also looks at the how these interference patterns evolve in time. The content of this chapter is based on these published works [3, 50].

1) “Interferometric Measurement of the Current-Phase Relationship of a Superfluid Weak Link”, S Eckel, F Jendrzejewski, A Kumar, CJ Lobb and GK Campbell, *Physical Review X*, 4, 031052

2) “Self-heterodyne detection of the in situ phase of an atomic superconducting quantum interference device”, R Mathew, A Kumar, S Eckel, F Jendrzejewski, GK Campbell, M Edwards, and E Tiesinga, *Physical Review A*, 92, 033602

3.1 Overview

A common approach in experimental physics is to vary a physical quantity and record the response of the experimental sample under investigation, allowing the construction of a functional response of the sample. For example, when studying electronics, two commonly used components are resistors and diodes. The current flowing through these components can be recorded as a function of the applied voltage difference. The behavior of these components are in sharp contrast. The current flowing through a resistor is linearly proportional to the voltage applied for metallic conductors, with the constant of proportionality known as the conductivity of the resistor. For a diode, the current flowing through it as a function of the voltage applied is an exponential. Since the current in these components occurs due to movement of the electrons, the current-voltage relation presents information on the transport of electron through these components.

3.1.1 Tunneling in quantum degenerate systems

The current transport in superconductors differs from normal metals as it is Cooper pairs that participate in the transport, and not individual electrons. While it was initially thought that the Cooper pairs cannot be transported through normal metal, Josephson calculated that when two superconductors are connected with a region with a weak link, there can be flow of supercurrent through the weak link by quantum tunneling [51]. This weak link could be a normal metal, a superconductor with lower cross-sectional area or even an insulator. He predicted that the current

flowing across the weak link would depend on the phase difference of the wavefunction of the two superconductors. He predicted that for a weak link narrower than the healing length, the current flowing would be a sinusoidal function of the phase difference. The current phase relation thus plays a similar role to the current voltage relationship in electronic components like resistors and diodes. The time evolution of the phase difference depends on the voltage difference across the weak link.

Soon after the experimental proof of Josephson tunneling, researchers started using these junctions for making sensitive magnetometers. In these magnetometers, a superconductor in the shape of a ring was constructed with either one or two weak links. The device with one weak link in the superconducting loop was called the radio frequency superconducting quantum interferometric device (rf-SQUID) [34]. As the magnetic field incident on the rf-SQUID is changed, the current changed to conserve the fluxoid conservation [34]. As the current reaches its maximum value (critical current), there is a phase slip and a magnetic flux quantum enters the loop. This can be used to characterize the magnetic field very accurately. It was also found that the current phase of the depleted region separating two superconductors is not always sinusoidal: when the depletion region is much greater than the healing length, the current phase relation is linear. The region of linear current phase relation is also known as the phase slip regime. It was also found that for certain value of the critical current, the current phase could be multiple valued, or the system would be hysteretic. Later, loops with two depleted regions were also used for better sensitivity.

Once the tunneling of superconducting Cooper pairs across weak links was

demonstrated, efforts were also made to observe these effects in other macroscopic quantum degenerate objects like superfluids. The first demonstration of oscillating mass currents across a weak link separating two reservoirs of superfluid ^3He was made in [52]. In a superfluid, the chemical potential difference across the weak link acts as the voltage difference. The first demonstration of a continuous transition of the current phase relationship from linear to sinusoidal was shown in superfluid helium [53].

3.1.2 Phase coherence of BECs

The realization of dilute alkali BECs gave physicists access to one more macroscopic quantum degenerate system. Soon efforts began to see Josephson effects in BECs, where two BECs would be separated by a repulsive laser beam, which creates the depleted superfluid density region. Some of the first theoretical work looking at these effect in BECs [54] predicted that a BEC Josephson like junction will not only exhibit the a.c. and d.c. analogues of Josephson junction, but also exhibit effects like macroscopic self-trapping due to interaction between the condensate atoms. The presence of a.c. and d.c. Josephson effects in a BEC was shown in [55]. The existence of self trapping in a single Josephson junction was shown in [56]. Predictions were also made about the current phase relation of a BEC flowing through a weak link [57].

This thesis focuses on the study of a weak link in a toroidal condensate, which is analogous to the case of a rf-SQUID. Previous experimental data in our lab

[58] has shown good agreement to theoretical models by assuming that the current phase relation for our system is the sum of a linear and a sinusoidal term. As an example, this model is able to explain how the persistent current state of the toroidal superfluid changes as a function of the drive frequency of the weak link [58]. However, the current phase relationship for a superfluid BEC flowing through a weak link in a toroidal trap could not be measured directly in this work [58]. The current-phase relationship for superconductors and superfluids has been measured before. We implement an interferometric technique to determine the current phase relation of our weak link directly. In addition, we also implement a technique which allows a one-shot determination of the circulation state, without extensive calibrations every time we changed the geometry of the ring trap. To do that, we add a phase reference to the toroidal trapping geometry, which is formed by a disc of atoms. There is no connection between the atoms in the ring and the disc. As the atoms cannot tunnel through the barrier between the disc and the ring traps, their phases are independent of each other. This chapter explains the experimental and analytical procedure used to extract the current phase relation.

3.2 Experimental setup

For this experiment, the atoms were trapped in a combination of toroidal and a disc trap. This combined potential is called the “target” trap. This trapping potential was created by using two crossed laser beams: one of the laser beams was a red-detuned sheet shaped laser beam and the other beam was a blue-detuned

intensity masked which had been masked with a toroidal potential. The mask was made from chrome deposited on glass substrate. The blue-detuned weak link was generated using a Gaussian shaped repulsive potential with a $1/e^2$ full width of $6 \mu\text{m}$. This beam was scanned radially around the mean radius of the toroid at a high frequency of 8 kHz, so the atoms felt a time averaged potential across the cross section of the ring. This scan rate was much faster than the timescale associated with the chemical potential of the BEC, which was ≈ 3 kHz. The same Gaussian beam was also used to imprint a circulation state by moving the beam around the ring. The ring potential had a mean radius of $22.4(4) \mu\text{m}$ with a radial Thomas-Fermi width $\approx 6 \mu\text{m}$. The total number of atoms in the combined target potential was 8×10^5 , with about a quarter of them in the disc trap. The radial trapping frequency of the toroidal trap was ≈ 390 Hz, the vertical trapping frequency is ≈ 500 Hz. To prepare the toroidal condensate in a well defined persistent current state with a fidelity of 0.95, the beam generating the weak link was ramped to an intensity of $U = 1.2\mu_0$ in 300 ms, kept constant for 400 ms, and then ramped down to zero in another 300 ms. The stirring was done at a constant rate of ± 0.95 Hz, which was slightly more than the quantum of circulation in the ring. These values were found empirically. To investigate the current phase relation, the weak link was added again and moved at different speeds. In this stage, the weak link was raised to a strength U less than the chemical potential. The laser beam making the weak link was raised to its final strength in 300 ms, kept constant for another 700 ms. At this point, all the traps were turned off and the atomic density distribution imaged in time of flight. We imaged the plane of the radial confinement using absorption

imaging.

3.3 Analysis of the Interferogram

3.3.1 Extracting the winding number

All the time of flight images end up in the destruction of the atomic cloud, so we get one data point per experimental run. Over the course of the day, we often take over thousand spiral images a day. Analyzing these interferometric patterns by the hand is tedious and prone to human errors, so an image processing algorithm was needed to automate this process. Further, to determine the current phase relation of the weak link, the exact shift of the spirals in the radial direction cannot be assigned by the eye. Another algorithm had to be developed to automate the current phase extraction as well. This algorithm has been explained in detail in the paper [50], here we list the important steps:

- 1) An optical density distribution image of the atoms in time of flight is extracted from the three images acquired for absorption imaging. A phase component analysis (PCA) is used to mitigate the effect of background fluctuations on the image quality, and the atom number is extracted using the knowledge of the cross sectional area of the atoms.

- 2) A low pass filter with a Gaussian half width of $1/e^2$ width of 2 pixels is applied to the image. This smooths out all the fluctuations on the length scale of a single pixel. Since the resolution of the imaging system is ≈ 5 pixels, this smoothing out does not smear out the recorded signal.

- 3) Next, a high pass filter with Gaussian half width of $1/e^2$ width of 8 pixels is applied to the image. This filtering removes the fluctuations which occur in the background on much larger scales.
- 4) The resultant filtered figure is then converted from a Cartesian coordinate system (x-y) to a polar coordinate system ($r - \theta$) with the radius and the azimuthal angle as the coordinates. We now have a discrete set of radii and azimuthal positions for which we have a filtered atomic density distribution data.
- 5) For each azimuthal position, we take a Fourier transform of the atomic density distribution with respect to the radial position. This yields the spatial frequency spectrum for a given azimuthal position. This procedure is repeated for each azimuthal position, and the average of the spatial frequency spectrum with respect to the azimuthal position is found. The spatial frequency with the maximum value corresponds to the average spacing between two interference fringes.
- 6) Next, the magnitude and the phase of the maximum spatial frequency is found as a function of the azimuthal angle. The change in this phase $\Delta\phi$ as we complete a revolution around the ring (cover a distance of 2π azimuthally) is determined. This phase is equal to $2\pi m$, where m is the circulation state of the superfluid.

3.3.2 Extracting the current phase relation

The interference between a persistent current state and a phase reference disc yields only azimuthal fringes when the weak link is turned off during time of flight.

When the weak link is turned on during time of flight, both azimuthal and radial fringes appear. To characterize the drop in phase across the weak link, we repeat steps 1 to 5 as before and then these additional steps are performed:

7) The two most dominant dark fringes closest to position of the weak link are identified. The maximum spatial frequency is recorded, and then the phase of these fringes is determined. This phase gives important information on the position of the relative minima of the fringes. The fringe tracing is done by using these minima. To prevent large scale of fluctuations in the extracted phase because of the weak link, this fringe tracing is stopped $\pm 5^\circ$ away from the position of the weak link.

8) Once the radial coordinates $r(\theta)$ of these fringes are extracted, we fit the radial positions to the weak link using the function $r(\theta) = c_1\theta^2 + c_2\theta + c_1 + c_d\Theta$, where Θ is the Heaviside function and c_d is the strength of the Heaviside function. Since the 1d azimuthal velocity in the bulk of the condensate is effectively constant, we expect the phase to have a linear profile along the bulk, the Heaviside function takes the phase drop across the weak link into account and the quadratic term takes the curvature of the spirals into account. This curvature may arise due to non-uniform 1d density around the ring or an incorrect center used for coordinate transformation.

9) Each fringe spacing, $|F_m|$, is equivalent to a phase difference of 2π , so the lateral displacement of the fringes c_d divided by the fringes spacing gives the phase jump α because of the weak link, where $\alpha = 2\pi c_d/|F_m|$. The fringe spacing is determined from the predominant Fourier component.

3.4 Theoretical model

We use local density approximation (LDA) for our analysis, which assumes that the density of a condensate is uniform locally. This assumption holds true when the length scale over which the density changes is greater than the healing length of the condensate. When LDA holds, the density distribution for stationary superfluids in the presence of an external potential is given by a Thomas-Fermi type of solution:

$$gn_{3d} = \mu - V(r, \theta, z), \quad (3.1)$$

where n_{3d} is the three dimensional atomic density, $V(r, \theta, z)$ is the confining potential, μ is the chemical potential and g is the interaction strength between two superfluid atoms assuming only s-wave collisions [1]. By integrating along the radial and the vertical degrees of freedom, we obtain a general relation:

$$\mu = b\sqrt{n_{1d}(\theta)} + V(\theta), \quad (3.2)$$

where $n_{1d}(\theta)$ is the number density along the azimuthal direction, $V(\theta)$ is the azimuthal potential and b is a numeric constant. The numeric constant b is determined by the trapping frequencies, the mean radius of the ring, and the interaction parameter g . In the presence of superfluid flow, the above equation has to be modified to take the kinetic energy of the flow into account. The modified chemical potential becomes:

$$\mu = \frac{1}{2}mv(\theta)^2 + b\sqrt{n_{1d}(\theta)} + V(\theta) \quad (3.3)$$

The above equation 3.3 is analogous to the Bernoulli equations for classical

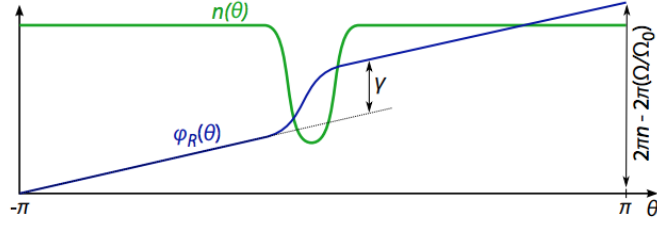


Figure 3.1: **Figure taken from [2].** Example of a possible phase/density profile around the ring. The phase profile has been evaluated in a frame co-rotating with the weak link. The green curve shows the density and the blue curve shows the phase. As we are in the rotating frame, the phase accumulated around the ring by the velocity (as measured in this frame) must be equal to $2\pi(\Omega/\Omega_0) - 2\pi\ell$, where ℓ is the circulation state. The additional phase drop due to the weak link γ is also shown in the figure.

fluids, which states that the sum of pressure, kinetic and potential energy of a fluid remains constant. In contrast, the above equation is valid for superfluids only when the quantum pressure term can be neglected and the chemical potential remains constant throughout the ring. This relationship can be used to solve for the velocity and density at all points around the ring. To obtain the azimuthal distribution of density and velocity, we transform ourselves in the frame of the weak link. The advantage of this Galilean transformation is that the azimuthal density distribution becomes time independent, as the perturbing potential is now stationary. The current flowing through the weak link is given by $I_{wl} = n_{1d}(\theta)v_r(\theta)$, where $v_r(\theta)$ is the azimuthal velocity in the frame rotating with the weak link. The current through the cross-section of the toroidal potential is a constant by the

continuity relation. If the weak link is rotating with a weak link Ω , then the velocity in the rotating frame is related to the lab frame by the Galilean transformation $v(\theta) = v_r(\theta) + \Omega R$, R is the mean radius of the ring. Since the velocity of the superfluid is proportional to the gradient of the phase, the phase ϕ around around the ring as a function of angle is given by:

$$\phi(\theta) = \frac{m}{\hbar} \int_{-\pi}^{\theta} (v(\theta')) R d\theta' = \frac{m}{\hbar} \int_{-\pi}^{\theta} (v_r(\theta') + \Omega R) R d\theta' \quad (3.4)$$

The contribution to the total phase from the second term $(m/\hbar) \int \Omega R^2 d\theta$ is the Sagnac (Peirels) phase. As shown in the figure 3.5, if we suppose the phase starts at 0 when $\theta = -\pi$ it must equal $2\pi\Omega/\Omega_0 - 2\pi\ell$ when $\theta = \pi$ to ensure that the full wavefunction is single valued.

3.5 Non-quantization of the angular momentum

While the circulation state of a toroidal superfluid is always quantized, the angular momentum associated with the flow is only quantized in the absence of a weak link. To prove this, we consider the special case when the superfluid is in the $\ell = 0$ circulation state and that the kinetic energy of the superfluid is small, which is true in the Thomas-Fermi approximation. This means that the azimuthal density distribution is independent of the flow velocity and is only dependent on potential around the ring. The angular momentum due to the superfluid flow around the ring is given by:

$$L = \oint m R n_{1d}(\theta) v(\theta) R d\theta \quad (3.5)$$

To compute the velocity distribution, the current through the weak link is calculated first using the constraint that the total phase drop around the ring will be zero for a $\ell = 0$ circulation state:

$$\frac{m}{\hbar} \int_{-\pi}^{\pi} \left(\frac{I_{wl}}{n(\theta)} + \Omega R \right) R d\theta = 0 \quad (3.6)$$

Since the current through the weak link will be a constant, the current will depend on the azimuthal average of the density distribution around the ring:

$$I_{wl} = -\frac{\Omega R}{\langle 1/n_{1d} \rangle}, \quad \text{with } \langle 1/n_{1d} \rangle = \int_{-\pi}^{\pi} [1/n(\theta)] \left(\frac{d\theta}{2\pi} \right) \quad (3.7)$$

This means that the velocity in the lab frame will be $v(\theta) = I_{wl}/n(\theta) + \Omega R$

$$L = mR \oint \left[-\frac{\Omega R}{\langle 1/n_{1d} \rangle} + n_{1d} R \Omega \right] \quad (3.8)$$

$$L = mR^3 \Omega \oint \left[-\frac{1}{\langle 1/n_{1d} \rangle} + n_{1d} \right] \quad (3.9)$$

Since $\langle n_{1d} \rangle \neq 1/(1/\langle n_{1d} \rangle)$, the angular momentum around the ring is non-zero, even though the superfluid is in the circulation state $\ell = 0$ with a net phase drop of 0 radians around the ring.

3.6 Experimental results

For finding the persistent current state, the atoms are released in time of flight. As the trap is turned off, the potential energy is released into kinetic energy and both the ring and the disc condensates expand radially. When the two clouds meet, they interfere. Assuming that the wavefunction of the toroidal condensate and the disc condensate are represented by the ψ_r and ψ_d respectively. An interference pattern

between these wavefunction will yield the pattern proportional to $(\psi_r^* + \psi_d^*)(\psi_r + \psi_d) = \psi_r^*\psi_r + \psi_r^*\psi_d + \psi_d^*\psi_r + \psi_d^*\psi_d$. The last term, which is the self interference term of the disc condensate does not produce any interference. The interference term between the ring and the disc $P_{rd} = \psi_r^*\psi_d + \psi_d^*\psi_r$ produce interference fringes when they expand such that they can overlap. The first term results when the ring condensate interferes with itself $P_r = \psi_r^*\psi_r$. This happens when the ring expands such that the width of the ring approaches the value of the radius of the ring. Then the opposite sides of the ring can interfere. Since the formation of P_r occurs at later times (shown later in the chapter), they are below the detection threshold of our imaging system.

We first consider the case when there is no persistent current flow in the ring and both the condensates are at rest before being released. We observe that the interference fringes in this case are concentric circles. As the condensates are released from the trap, they pick up an additional phase due to their motion, which is predominantly in the radial direction. We assume that the phase of the disc is ξ_d^b before the expansion and it picks up an additional phase of ξ_d^a during the expansion. Similarly, the the phase of the ring condensate is ξ_r^b before the expansion and it picks up an additional phase of ξ_r^a during the expansion. An interference fringe is formed at those radial locations where the phase difference between the two condensate is a integral multiple of 2π , i.e. $\xi_d^a + \xi_d^b - \xi_r^a - \xi_r^b = 2k\pi$, where k is an integer. Since there is no azimuthal variation in phase of both the disc and ring, the radial distance atoms from separate points of the ring have to travel to reach a site of constructive interference is also the same. Hence the interference pattern consists of concentric

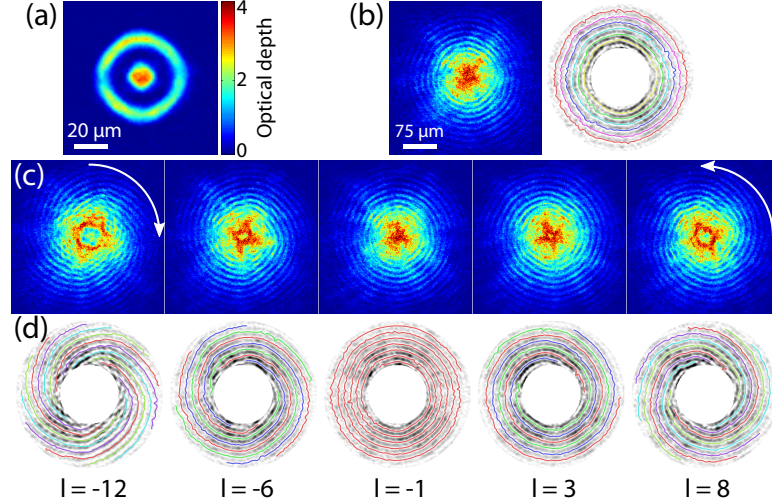


Figure 3.2: **Figure taken from [2].** (a) *In-situ* image of the ring and disc BECs. The dimensions can be estimated using the scale bar shown in the figure. (b) Example interferogram after 15 ms time-of-flight (left) when there is no current in the ring. Traces of the azimuthal interference fringes extracted from an image processing algorithm have been drawn as a guide to the eye (right). (c) Interferograms for various winding numbers, where the arrow indicates the direction of flow. (d) Traces of the interference fringes to guide the eye and count the number of spiral arms. The extracted winding number is also shown.

circles. The spacing between any two fringes corresponds to a phase difference of 2π .

We next consider the case when there is a persistent current state in the toroidal condensate. In this case, the phase ϕ varies linearly around the ring as a function of the azimuthal position θ . The relation is given by $\phi = \ell\theta$, where ℓ is the circulation state of the superfluid. We assume that the azimuthal variation of the condensate 1d number density and velocity are minimal. The persistent

current causes a uniform phase gradient across the ring trap in the absence of a weak link. Since there is linear variation in the phase around a ring as a function of the azimuthal angle, the radial distance for a given fringe also changes approximately linearly as function of the azimuthal angle. This variation yields a spiral (Fig. 3.2). This gives us the capability to find the chirality and the persistent current state in one shot.

The interference patterns are changed significantly when a density perturbation (weak link) is kept on when releasing the atoms in time of flight. For these experiments, the weak link has a strength less than the chemical potential. In this case, the atoms on either side of the weak link expand azimuthally towards each other and interfere, causing additional set of interference patterns to appear (see figure 3.3). We will use the following nomenclature from now on: if we track an interference fringe and the density minimum associated with the fringes moves azimuthally, we call it an azimuthal fringe. If the minimum moves radially, the fringe is called a radial fringe. If a given radial fringe is traced through the weak link, the lateral displacement of the fringe with respect to the fringe spacing can be used to find the phase drop across the weak link. We assume that the phase picked up by the flow of the current around the ring is given by α , and that the mass current flowing through the bulk condensate is $I_{bulk} = (n_{1d}\hbar\nabla\phi)/m = (n_{1d}\hbar\alpha)/(m2\pi R)$. Here I_{bulk} is the mass current through the bulk condensate, n_{1d} is the 1d number density, m is the mass of one superfluid atom, R is the mean radius of the toroidal potential and $\nabla\phi$ is the gradient of phase of the wavefunction. The mass current of a superfluid in its first persistent current ($I_0 = n_{1d}\Omega_0 R$), where $\Omega_0 = \hbar/(mR^2)$ is

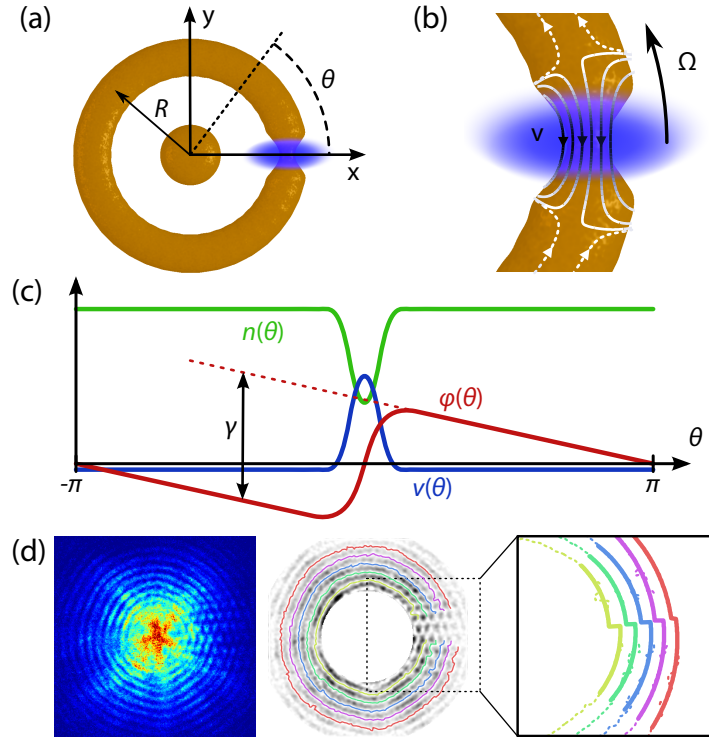


Figure 3.3: **Figure taken from [2].** (a) Schematic of the atoms in the trap with a weak link applied. The coordinate system used throughout is shown; $\theta = 0$ corresponds to the \hat{x} axis. (b) A close up of the weak link region. When the weak link is rotated at Ω , atoms flow through the weak link as shown by the stream lines. Larger velocities along the stream lines correspond to darker lines. (c) The resulting density $n(\theta)$, velocity $v(\theta)$, and phase $\phi(\theta)$ as a function of angle, with the phase drop γ across the weak link shown. (d) Method of extracting the the phase from an interferogram (left). First, we trace the interference fringes around the ring (center) and then fit the discontinuity across the region where the barrier was (right).

the angular velocity of the first circulation state. The current flowing in the bulk when normalized by the mass current of a superfluid in its first persistent current ($I_0 = n_{1d}\Omega_0 R$) state is given by $I_{bulk}/I_0 = \alpha/(2\pi)$. We measure I_{bulk} as a function of the rotation rate, Ω , of the weak link for multiple strengths of the weak link. Measurements for four such weak link strengths are shown in figure 3.4. We see that at two weak link strengths, there is a change in the circulation state (or a phase slip) and I_{bulk}/I_0 as a function of rotation rate of the weak link is multiple valued, which ceases to be the case as the weak link strength is increased. The gray lines shown in 3.4 correspond to the solid body rotation limit, in which the weak link has a strength greater than the chemical potential. In this limit, the superfluid cannot penetrate the weak link and is dragged along with the same speed as the weak link.

We see from the above plots that even when the superfluid is in a persistent current state of $\ell = 0$, when the weak link is rotated there is still a mass flow. As the the weak link is rotated around the ring, the number of atoms that flow through the weak link depends on the density difference in the weak link and the bulk of the superfluid. As the phase drop around the ring must still be zero (the superfluid is in the persistent current state $\ell = 0$), there must be some current in the weak link which cancels the effect of fluid flow through the weak link. Once the bulk mass current has been determined, we can find the current through the weak link in the frame of the weak link to be $I_{wl} = n_{1d}R\Omega - I_{bulk}$, while the phase drop across the weak link γ will be $\gamma = -2\pi I_{bulk}/I_0 = -\alpha$. Using these relations together, we can find the current phase relation of the weak link, as shown in figure 3.5. We find that the current phase relation for our weak link is linear, as our weak link is about

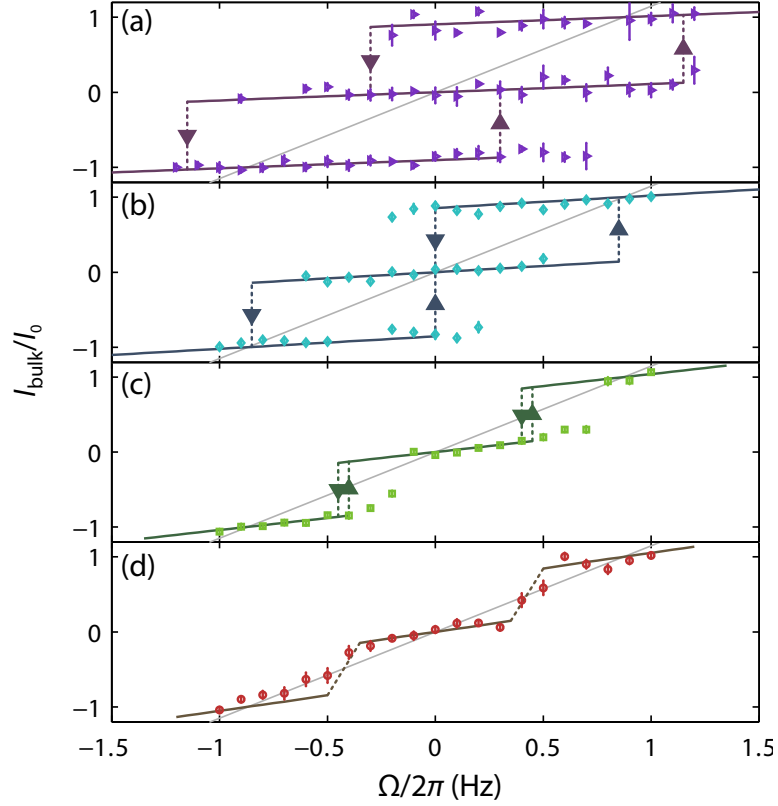


Figure 3.4: **Figure taken from [2]**. Plot of the normalized current around the bulk of the ring, $I_{bulk}/I_0 = \alpha/2\pi$, vs. the rotation rate Ω of the weak link for four different weak link potential strengths U : (a) $0.45 \mu_0$, (b) $0.6 \mu_0$, (c) $0.7 \mu_0$, (d) $0.8 \mu_0$. The solid lines are the prediction of local density approximation (LDA) model. The dashed, vertical lines show the predicted transitions between the different winding number branches. The thin, gray, diagonal lines represent the limit of the solid body rotation, when all the atoms in the condensate move around the bulk of the ring with the weak link, i.e., $I_{bulk} = n_{1d}R\Omega$.

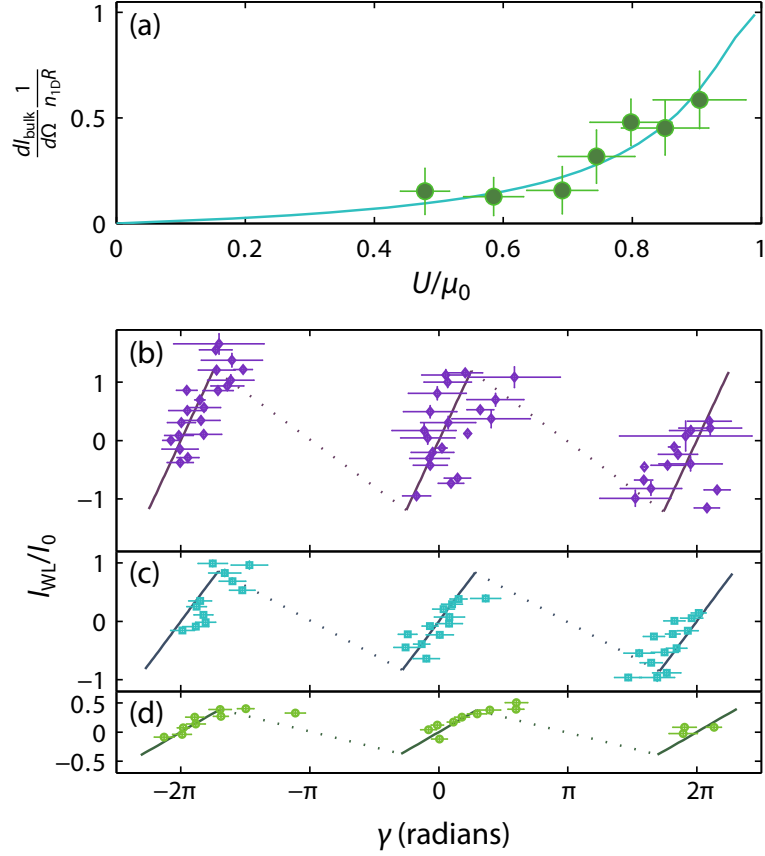


Figure 3.5: **Figure taken from [2].** (a) Derivative of the initial bulk current $dI_{bulk}/d\Omega$ vs. U , normalized to the expected value in the limit where $U/\mu_0 \geq 1$, $n_{1d}R$. The solid line shows the prediction of the LDA model. (b)–(d) Extracted current-phase relationships from the data in Fig. 3.4, for three different weak link potential strengths U : (b) $0.45 \mu_0$, (c) $0.6 \mu_0$, (d) $0.7 \mu_0$. γ is the phase across the weak link and I_{WL} is the current through it, normalized to $I_0 = n_{1d}R\Omega_0 \approx 5 \times 10^5$ atoms/s. The solid curves represent the prediction of our theoretical model. The dashed lines merely guide the eye by connecting the multiple branches of the current-phase relationship.

an order of magnitude greater than the healing length. Hence we are far away from the Josephson junction regime where the healing length is of the same order of the weak link and the current phase relation is sinusoidal.

3.7 Tracking the time evolution of spirals

The previous sections explain how a ‘target trap’ interferometer allows a single shot determination of the persistent current state, and the current phase relationship of a weak link. However, limitations of the experiment prevent us from answering the following questions:

- A typical ‘target trap’ interferometer uses 8×10^5 atoms. What is the minimum number of atoms needed to make an interferometer? In an actual experiment, we observe that we cannot make a multiply connected trap for low atom numbers.
- What happens to the interference patterns at long time of flight? In the actual experiment, the atomic cloud begins to fall outside the field of view of the imaging system after 30 ms time of flight.
- What is the role of interatomic interactions in the interferogram? We do not have the capability to turn off the interatomic interactions for sodium atoms in our experiment, which arise predominantly from s-wave collisions.

To answer these questions, our theoretical collaborators applied both numerical and analytical asymptotic expansion techniques to the problem of a single atom placed in an interferometer. While the details of their work can be found in ref. [3], we summarize the important results from their work:

1) They placed a single atom in the ‘target trap’ interferometer. The wavefunction of a single atom was a coherent superposition of the wavefunction of the toroidal and the disc potential. The expansion of the condensate was first followed numerically by solving the Schrodinger equation. The confining potential was turned off, so it was easier to solve the time propagation in the momentum space, where the kinetic energy appears as a phase factor. The wavefunction in the $r - \theta$ space was Fourier transformed to the momentum space, the phase factor for the kinetic energy is applied and the wavefunction was Fourier transformed back to the $r - \theta$ space. The numerical simulations showed the emergence of spirals as soon as the toroidal and the disc wavefunctions overlapped.

2) They found using analytical estimates that the toroidal wavefunction as a function of time was given by:

$$\chi_S(r, \theta, t) = \left[e^{-(r-R)^2/[2\sigma_S^2(t)]} \varphi_S(\theta) + e^{-(r+R)^2/[2\sigma_S^2(t)]} \varphi_S(\theta + \pi) \right] / (\mathcal{N}_2(t)\sqrt{r}), \quad (3.10)$$

where R was the initial mean radius of the toroid, $\varphi_S(\theta)$ was the in-situ toroidal wavefunction, \mathcal{N}_2 was a normalization constant, σ_S was the initial mean width of the toroid and $\sigma_S(t)$ was the width of the toroidal wavefunction as a function of time. The width as a function of time was given by $\sigma_S^2(t) = \sigma_S^2 + i\hbar t/m$. At small times of flight, the first term of equation 3.10 was the dominant term, while at later times of flight, both the term were contributing. The first term by itself lead to spirals in the time of flight, while the second term lead to rings in the interference pattern. The rings emerged in the time of flight when the width of the toroidal condensate became

comparable to its radius. While the rings were seen in numerical simulations, they could not be seen in actual experimental data.

The analytical results also showed that the spacing between any two fringes δ showed a linear dependence on the time of flight t , i.e. $\delta = 2\pi\hbar t/mR$. We took experimental data at multiple times of flight to verify this prediction. This set of data was taken without any circulation state state imprinted on the toroidal condensate. The spacing between radial fringes at any given time of flight was extracted using the techniques described previously. The experimental results, along with the values from the numerical simulations and analytical estimates have been plotted in figure 3.6.

3) Previous work has shown that an interacting BEC will expand faster than a non-interacting cloud [59, 60]. We found this to be true even for our system. While the analytical estimates were derived for the case of a single atoms placed in the ‘target trap’ interferometer, the numerical simulations were performed using GP simulations. These simulations calculated the initial wavefunction using the Thomas-Fermi approximation. In this approximation, the kinetic energy of the atoms is much less than the interaction energy and is neglected.

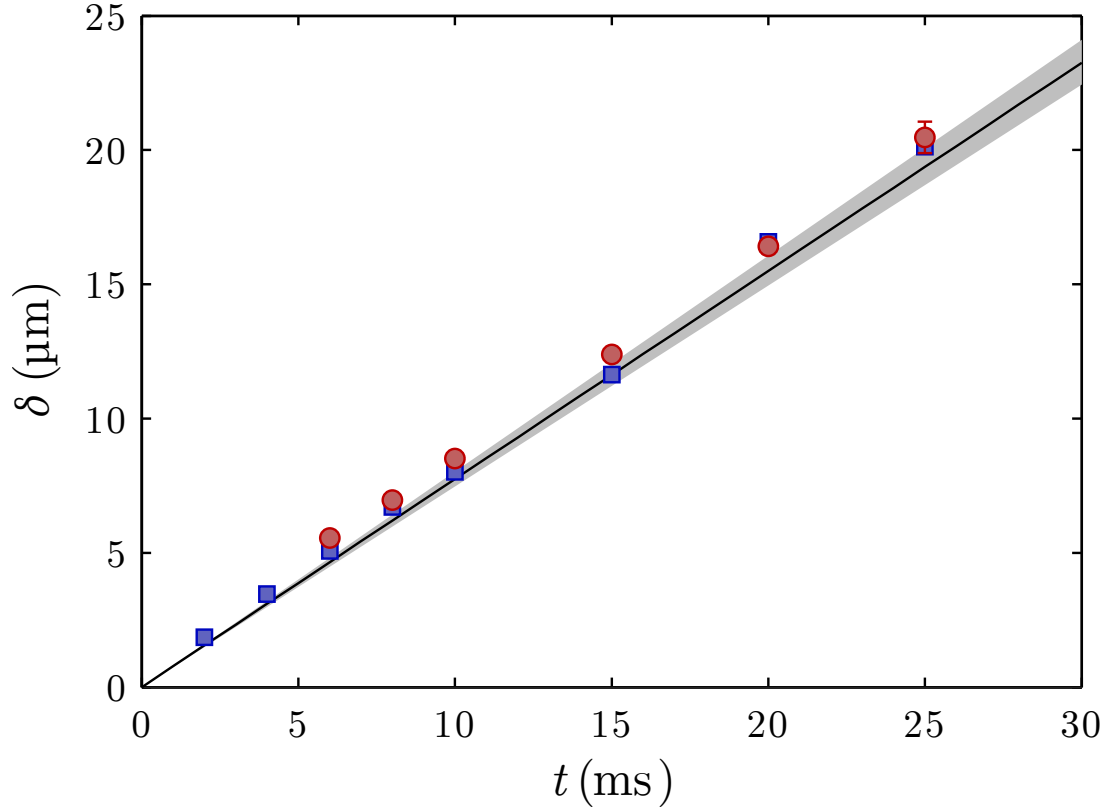


Figure 3.6: **Figure taken from [3]**. The radial spacing between azimuthal fringes is shown as function of time. The experimental data is for a condensate with no circulation state and weak link present before releasing the atoms in time of flight. The experimental, GPE and single-particle fringe spacings are shown by red dots with one-standard deviation statistical error bars, blue markers and a black line, respectively. The value of R has a uncertainty, which arises from the fit function. This uncertainty is shown by the shaded region around the blackline.

Chapter 4: Resonant wavepackets and shock waves in an atomtronic SQUID

In this chapter, we study the excitation spectrum of a toroidal Bose-Einstein condensate superfluid with a weak link. We measure the excitation spectrum by introducing a density perturbation (alternatively called a weak link) in the confining potential, and driving the weak link harmonically in either intensity or spatial position. The resonance frequency is determined by looking at the atomic loss spectrum at various drive frequencies. This work has been previously described in the published work [4].

“Resonant wavepackets and shock waves in an atomtronic SQUID”, Yi-Hsieh Wang, A Kumar, F Jendrzejewski, Ryan M Wilson, S Eckel, GK Campbell, and CW Clark, New J. Phys. 17, 125012.

I contributed to the experimental data acquisition and the analysis.

4.1 Overview

In the previous chapter, we looked at the current phase relationship of a weak link in a toroidal BEC superfluid. A single weak link in the toroidal confinement is the equivalent of a radio frequency superconducting quantum interferometric device (RF-SQUID) in superconductors. The RF-SQUID is used as a magnetic field sensor. The analog of a superfluid with a weak link is a rotation sensor. Experimental signatures of these systems include quantized persistent currents [49], phase slips [61], hysteresis [62] and a well defined current phase relationship [50]. Devices with two density depleted weak links are also widely used, and are known as direct current superconducting quantum interferometric device (dc-SQUID) Analogs of the dc-SQUID have also been shown to exist in toroidal superfluids [55,63]. Experiments have shown both the ac and the dc Josephson junction effect in superfluids, and the presence of resistive flow above a critical mass current.

An important quantity in the study of superfluids is the existence of a critical velocity, beyond which dissipation sets in. Experiments with two weak links have found that the critical velocity is equal to the sound speed [63], which is in agreement with the zero temperature Gross-Pitaevskii theory. On the other hand, experiments with one weak link find a critical velocity which is a fraction of the sound speed [62]. Other variables like temperature may also affect the critical velocity, since an increase in temperature increases the thermal fraction which leads to more dissipation. This points out that the mechanism of creating excitations in each system can be different, and a knowledge of the excitations spectrum of a

system is required for a thorough understanding of the dynamics of a given system. This knowledge may be instrumental in the design of new atomtronic devices. For example, a phonon interferometer was shown recently [64], along with a means of detecting the circulation state of a superfluid in-situ without releasing it in time of flight [40].

We can probe the excitation spectrum of a toroidal superfluid by harmonically driving a density depleted weak link. This weak link has a similar geometry to previous studies of our lab [50, 62, 65]. The harmonic drive of the weak link can be induced either by changing the intensity of the laser beam or by changing the azimuthal position of the laser beam. As the spatial profile or the position of the weak link changes as a function of time, a mass current is induced. These displaced atoms are launched as phonon waves in the bulk of the superfluid away from the weak link. An intrinsic frequency of interest is the orbital angular frequency of the phonon. The orbital frequency of the phonon is the number of revolutions a phonon makes around the ring in a unit time. The phonon speed and the geometry of the ring trap (i.e. the circumference) determine the orbital frequency. The phonon speed depends upon the chemical potential, which depends upon physical variables like the vertical and radial trapping frequency and the atom number. When the frequency of the harmonic drive of the weak link matches any of the resonance frequencies of the system, the coupling of energy between the superfluid and the weak link is increased. As atoms gain more and more energy during a long enough drive, they may eventually escape the toroidal trap. We expect more atom losses at the resonant frequencies. For our experiment, the intensity of the beam providing the

radial confinement is factor of ≈ 2 more than the spillover point, i.e. the threshold at which the radial trapping beam is just strong enough to capture all the available atoms. The exact location of the resonance can be obtained by a fit to the atom number remaining in the trap after modulation as a function of the modulation frequency. The loss of atoms from the trap points to heating in the system, which arises from the deposited kinetic energy being dissipated. The dissipation arises due to the interplay between the anisotropy of the trap and the nonlinear interaction of the BEC. It has been shown that mode coupling plays a major role in the system dynamics [66–69]. The energy transfer due to mode coupling and mean-field effects work in different ways. The anisotropy of the trap spreads the response over two main frequencies, which are the radial and the vertical trapping frequency. On the other hand, the mean field interaction of the BEC couples all modes of interaction to one another.

As shown in figures 4.6 and 4.7, we identified multiple resonant frequencies while studying the one weak link system, using both intensity and spatial modulations. We find that some of these resonances occur at integral multiples of the orbital frequency while some of the resonances occur at half-integral multiples of the orbital frequency. At these frequencies, the weak link periodically adds energy to a phonon wavepacket during each oscillation cycle. We will now see the mechanism of how these resonances arise in a one weak link system.

4.2 A simple model of resonant wavepacket generation by an oscillating weak link

The phonon wavepackets can be described as a superposition of low lying Bogoliubov excitations (see [4] and section 4.4 for details). Since any phonon wavepacket consists of a linear superposition of multiple Bogoliubov modes, these modes can travel away from their source of origin without any dispersion. This holds true only for low strengths of the density perturbation. As the perturbation strength increases, the linear approximation breaks down and nonlinear effects are seen [70]. Some of these features include dark solitons, vortices and vortex rings. These nonlinear excitations can travel at a speed less than the sound speed. Nonlinear interactions may also lead to excitations that travel at a speed greater than the speed of sound. These excitations are known as shock waves. Since a ring condensate is a periodic system with respect to the azimuthal coordinates with no ends, the phonon wavepackets created travel around the system. The orbital period, T , of a single wavepacket establishes a characteristic frequency, $\nu = 1/T = c/(2\pi R)$, where c is the speed of sound in the bulk condensate and R is the mean radius of the toroidal trap. We launch phonon wavepackets in the ring by two means, by either changing the intensity of the weak link or by changing the azimuthal position. The excitations spectra for these drives is measured as a function of the drive frequency. The mechanism of the resonance depends on the type of drive, we will now look at intuitive pictures of how these resonances arise.

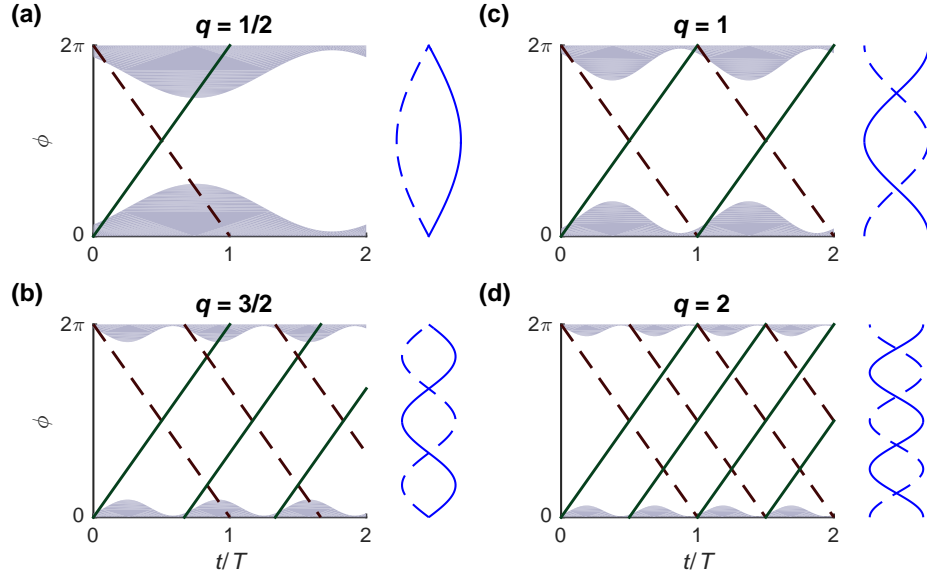


Figure 4.1: **Figure taken from [4].** Trajectories of wavepackets in a ring when the strength of the weak link is modulated. The grey shaded areas represent the density depleted region, which changes as a function of time, t . The strength of the weak link oscillates with a frequency of $\nu_q = q\nu$: (a) $q = 1/2$; (b) $q = 3/2$; (c) $q = 1$; (d) $q = 2$. Here, ν is the orbital frequency of the phonons. The solid and dashed lines indicate the ring azimuthal coordinates, ϕ , of the centers of the wavepackets. The blue lines show the standing-wave-like density modulation created by the phonon wavepackets as they travel around the ring and overlap.

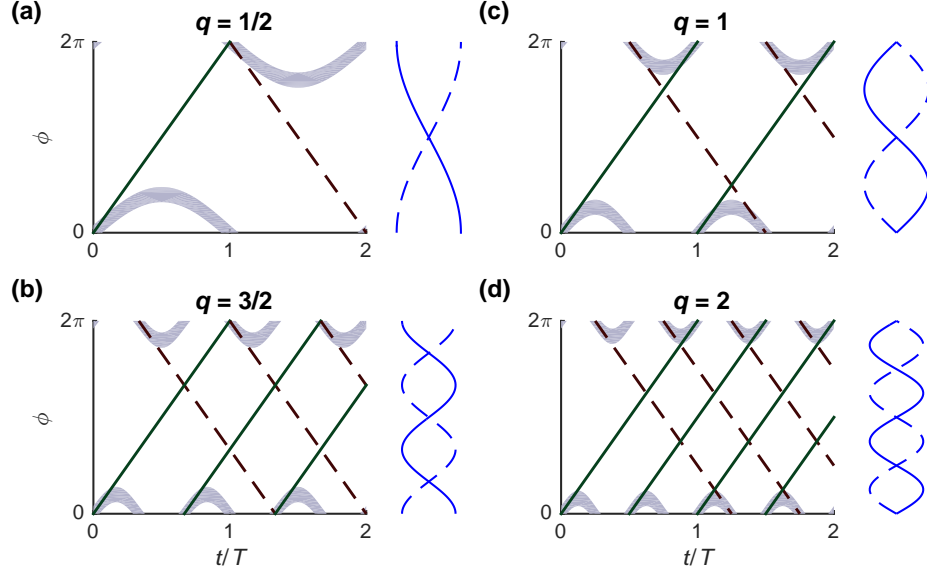


Figure 4.2: **Figure taken from [4].** Trajectories of wavepackets in a ring when the position of the weak link is modulated harmonically. The frequency of the modulation is given by $\nu_q = q\nu$, where (a) $q = 1/2$; (b) $q = 3/2$; (c) $q = 1$; (d) $q = 2$. Here, ν is the orbital frequency of the phonons. The grey shaded areas represents the density depleted region of the weak link, whose azimuthal position changes as a function of time, t . The solid and dashed lines indicate the azimuthal coordinate, ϕ , of the centers of the wavepackets. The blue lines show the standing-wave-like density modulation created by the phonon wavepackets as they travel around the ring and overlap.

We first consider the case when the weak link is modulated in intensity around a mean positive value. The azimuthal position of the weak link is left unchanged. A schematic of the above situation is shown in figure 4.1, where the grey shaded region represents the density depleted region of the superfluid ring due to the weak link. The area encompassed by the grey region expands and contracts harmonically, which shows that the intensity of the laser beam making the weak link is changing as a function of time. As the perturbation strength increases, the superfluid density at the weak link decreases and the displaced superfluid atoms are launched as phonons. These phonons then travel away from the weak link into the bulk of the condensate. The phonons are launched symmetrically, and subsequently travel around the ring in opposite directions. The phonons after an orbital time period T will complete one revolution around the ring and arrive back at the weak link. If the phonons arrive back at the position of the weak link after completing a revolution just as the rate of change of the strength of the weak link reaches a maxima, the newly launched phonon wavepacket coincides with the incoming phonon wavepacket. This implies that when the harmonic drive frequency ν_q is an integral multiple of the orbital frequency, there will be a resonance. This means that $\nu_q = q\nu$, where q is an integer and ν is the orbital angular frequency of the phonon. The orbital angular frequency of the phonon can be evaluated by the following relation: $\nu = 2\pi R/c_s$, where R is the mean radius of the radial trap and c_s is the sound speed. On the other hand, when the intensity of the laser beam generating the weak link is decreasing as a phonon wavepacket approaches the weak link having completed a revolution around the ring, atoms will be removed from the wavepacket and the phonon wavepacket

will lose energy. This is the case when q is half an integer. Some of these cases have been shown in figure 4.1 : where panels (a) and (b) show nonresonant cases with $q = 1/2$ and $3/2$, and panels (c) and (d) show the resonant case with $q = 1$ and 2 .

The second method that we use to probe the excitation spectrum of the ring superfluid is to drive the weak link harmonically in the azimuthal coordinate. In this situation, the intensity and hence the shape of the weak link remains constant, but the azimuthal position is varied in time. As the weak link moves, it pushes the atoms in front of it, launching them into a phonon wavepacket when the weak link is moving at its fastest speed. In this case, a phonon is launched into only one direction, depending upon the direction of motion of the weak link. The wavepacket then travels around the ring. If the drive frequency is an integral multiple of the orbital frequency, the newly launched phonon and the incoming phonon completing a revolution are traveling in opposite directions. These wavepackets negate the effect of one another, and no buildup of energy can take place. On the other hand, if the drive frequency of the weak link is a half integral multiple of the orbital frequency, the phonon wavepacket after completing one revolution around the ring will get a fresh momentum kick from the weak link and will continue to move around the ring. This situation has been shown in figure 4.2. Panels (a-d) correspond to $q = 1/2, 1, 3/2,$ and $2,$ respectively. The corresponding standing waves are shown on the right of each panel.

As pointed out earlier, a modulation in the strength of the weak link launches symmetric phonon waves, which then move around the ring in clockwise and anti-

clockwise direction. As these traveling phonon wavepackets overlap, they create a region with higher density at the position of the overlap and a lower density region away from the overlap position. This variation of density is similar to a standing wave. To visualize these regions, there are dashed and solid blue lines on the right side of panels (a)-(d) in the figure 4.1. When q takes integral values, the standing wave pattern density pattern propagates like a cosine function $\cos(q\phi) \sin(2\pi\nu_q t)$, while the standing wave takes a sine pattern $\sin(q\phi) \sin(2\pi\nu_q t)$ when q takes half integer values. When q takes half integer values, the possible standing wave configurations resembles the Schrodinger equation solution of a particle in a box. Hence the sine wave solutions are referred to as ‘box modes’. These ‘box modes’ have zero value at the boundaries. On the other hand, when q takes integer values, the standing density waves resemble the wavefunction of a particle on a ring. Hence these modes with a cosine like solutions are referred to as ‘ring modes’. Thus we see that a harmonic drive using intensity modulation is resonant with the ‘ring modes’ and non-resonant with the ‘box modes’. For position-modulation excitation, the box modes are resonant and the ring modes are nonresonant.

We would like to point out that all the above arguments about the ‘box mode’ have assumed that a phonon wavepacket is completely reflected after being kicked by the weak link, as its position is modulated harmonically. However, this assumption breaks down when the intensity of the perturbation is so low that most of the phonon wavepacket is transmitted. The speed of sound in the weak link region decides whether the phonon wavepacket will be reflected or transmitted. If the intensity of the laser beam making the weak link is high, the density in the weak

link region will be low and so will the local sound speed. In this case, there will be mismatch between the atom density (and hence the local sound speed) in the bulk and the weak link, which leads to reflection of the wavepacket. An analog situation exists in optics, where the reflection coefficient R at the interface between two media is $R = (n_1 - n_2)^2 / (n_1 + n_2)^2$, where n_1 and n_2 are the index of refractive index of the two media. When the intensity of the weak link is low, the reflectivity is very low and most of the phonon wavepacket makes it way through. Thus a position modulated drive with a weak link of low intensity will begin to resemble the drive of a ‘ring mode’ where the phonon wavepacket gains in energy only when it is transmitted. Thus, one should expect a change in the resonance condition for a position-modulated barrier: as the strength of the weak link is increased, the resonance shifts from integer to half-integer values of q .

4.3 Experimental Parameters

The toroidal confinement of the condensate BEC is formed in a crossed optical dipole trap with the same procedures as in Ref. [50]. The vertical confinement is created by a red detuned laser beam and the radial confinement is created by imaging an intensity mask on the plane of the atoms [71]. The sodium condensate is created in the $|F = 1, m_F = -1\rangle$ state. The intensity mask consists of a ring trap and a disc trap concentric with the ring trap. These two potentials together are called the “target” trap [50]. The ring shaped condensate has a mean radius of $22(1) \mu\text{m}$ and a Thomas-Fermi full-width of $\approx 8 \mu\text{m}$. The disc-shaped condensate,

which is left unperturbed during the experiment, serves as a reference to check atom number stability. This prevents atom losses due to technical noise being incorrectly identified as a resonance. The radial trapping frequency of the ring condensate is $\omega_\rho/2\pi = 400(20)$ Hz, while the trapping frequency of the red-detuned beam providing vertical confinement is $\omega_z/2\pi = 542(13)$ Hz. The average number of atoms in the target trap is $\approx 7 \times 10^5$, with $\approx 80\%$ of atoms in the toroid and the remaining $\approx 20\%$ in the central disc. The atom number fluctuations from one cycle of the experiment to another fluctuates around its mean by up to 10% (2σ). We measure the atomic density using *in-situ* partial transfer absorption imaging [48].

We create the weak link potential by using a focused, blue-detuned Gaussian beam. The $1/e^2$ full-width of the Gaussian is $\approx 5 \mu\text{m}$. The weak link is created using a blue-detuned beam at 532 nm, which create a repulsive potential, depleting the condensate density locally where the beam is incident. An acousto-optic deflector (AOD) controls the position of the beam. By changing the power applied to the AOD, we can control the intensity of the beam. To create a radially-elongated weak link, the AOD scans the beam rapidly in the radial direction at 2 kHz. The resulting time-averaged potential is a wide, flat potential barrier with an effective width of $\approx 15 \mu\text{m}$. This creates an effective paddle which can push the superfluid around the ring.

For the experiments here, we manipulate the weak link in a variety of different ways. For the experiments described in Sec.4.5 (and shown in figure 4.1), the weak link is first applied adiabatically to the BEC, so as to not generate excitations. The weak link beam's intensity is ramped on linearly over 300 ms. During this linear

ramp, the azimuthal position of the weak link is fixed. After the intensity reaches its final value, the weak link position is oscillated in the azimuthal direction, or its intensity is modulated as a function of time. For the experiments described in Sec. 4.6 (and shown in figure 4.2), the weak link beam is turned on suddenly while it remains in a fixed azimuthal position. The fastest response time of the AOD is around $100 \mu\text{s}$, which is a result of the servo that controls the intensity of the weak link beam.

4.4 Bogoliubov - de Gennes description of elementary excitations of a BEC

In parallel to experiments to determine the resonant frequencies of the toroidal superfluid, one can also make numerical estimates of the resonance frequencies using a mean-field based approach [72, 73]. While the calculations specific to our experiment have been described in detail in [4], a summary is provided here for completeness. The condensate density can be determined by using the order parameter $\Psi_0 = \langle \hat{\Psi} \rangle$, where $\langle \rangle$ denotes the spatial average. Here $\hat{\Psi}$ is a quantum field operator:

$$\hat{\Psi} = \Psi_0 + \delta\hat{\Psi}, \quad (4.1)$$

where $\hat{\Psi}_0$ is the quantum field operator for the condensate atoms and $\delta\hat{\Psi}$ is the field operator for the non-condensate atoms. In linear response theory, the field operator

of the non-condensate atoms can be used to determine the elementary excitations of the system. The time evolution of the condensate wave function is obtained by using a time-dependent Gross-Pitaevskii equation (TDGPE),

$$i\hbar\frac{\partial}{\partial t}\Psi_0(\mathbf{r},t) = \left[-\frac{\hbar^2}{2M}\nabla^2 + V(\mathbf{r}) + g|\Psi_0(\mathbf{r})|^2\right]\Psi_0(\mathbf{r}), \quad (4.2)$$

where $V(\mathbf{r})$ is the trapping potential, M is the mass of one sodium atom, and $g = 4\pi\hbar^2 a/M$ is a measure of the interaction strength between the two atoms. The magnitude of g depends on the s-wave scattering length between two sodium atoms, $a = 2.5$ nm. The time dependent ground state solution of the GPE in a stationary potential is given by

$$\Psi_0(\mathbf{r},t) = \sqrt{n(\mathbf{r})}e^{-i\mu t/\hbar} \quad (4.3)$$

where $n(\mathbf{r})$ is the density of condensed atoms, and μ is the chemical potential. The linear theory holds only when the non-condensed atoms are a small fraction of the total number of atoms. The non-condensed field operators then satisfy the equations:

$$i\hbar\frac{\partial}{\partial t}\delta\hat{\Psi}(\mathbf{r},t) = \left[-\frac{\hbar^2}{2M}\nabla^2 + V(\mathbf{r}) + 2gn(\mathbf{r}) - \mu\right]\delta\hat{\Psi}(\mathbf{r},t) + g\Psi_0^2\delta\hat{\Psi}^\dagger. \quad (4.4)$$

We solve this equation in a Bogoliubov-de Gennes framework [72, 73], and expand $\delta\hat{\Psi}$ in terms of the creation and annihilation operators a_i and a_i^\dagger ,

$$\delta\hat{\Psi} = \sum_i \left(u_i e^{-i\omega_i t} a_i + v_i^* e^{i\omega_i t} a_i^\dagger \right), \quad (4.5)$$

where ω_i are the resonance frequencies and u_i, v_i are the Bogoliubov amplitudes of the i^{th} excitation. These amplitudes satisfy the Bogoliubov-de Gennes (BdG)

equations:

$$\begin{aligned} \left[\hbar\omega_i + \frac{\hbar^2}{2M}\nabla^2 - V(\mathbf{r}) - 2gn(\mathbf{r}) + \mu \right] u_i(\mathbf{r}) &= gn(\mathbf{r})v_i(\mathbf{r}) \\ \left[-\hbar\omega_i + \frac{\hbar^2}{2M}\nabla^2 - V(\mathbf{r}) - 2gn(\mathbf{r}) + \mu \right] v_i(\mathbf{r}) &= gn(\mathbf{r})u_i(\mathbf{r}). \end{aligned} \quad (4.6)$$

The spectrum of the elementary excitations for the condensate can be obtained by numerically diagonalizing eqs. (4.6). A simple solution to the above equations exist when the external potential is turned off and the condensate has uniform density. In this case, the Bogoliubov amplitudes are given by [73], $u_{\mathbf{k}}(\mathbf{r}) = u_{\mathbf{k}}e^{i\mathbf{k}\cdot\mathbf{r}}$ and $v_{\mathbf{k}}(\mathbf{r}) = v_{\mathbf{k}}e^{i\mathbf{k}\cdot\mathbf{r}}$, where \mathbf{k} is the wave vector. These are plane wave solutions and hence represent a continuous spectrum of elementary excitations. The energy of excitations is given by:

$$\hbar\omega_{\mathbf{k}} = \sqrt{\epsilon_{\mathbf{k}}^2 + 2\epsilon_{\mathbf{k}}gn}, \quad (4.7)$$

where $\epsilon_{\mathbf{k}} = \hbar^2k^2/2M$ is the kinetic energy of a free quantum particle of mass M . For small k , the frequencies $\omega_{\mathbf{k}}$ are linear in k , i.e. $\omega_{\mathbf{k}} \approx k\sqrt{gn/M}$. A small magnitude of the wavevector implies large wavelengths. The energy of excitation at low wavenumbers is given by $\omega = ck$, displaying linear dispersion. These excitations may be viewed as phonons. The ratio of the excitation energy and the wavenumber yields the sound speed, $c = \sqrt{gn/M}$.

In an actual experiment, a condensate is confined to a potential. Coming back to our experiment, the superfluid is trapped in a toroidal potential, which has the form

$$V(\mathbf{r}) = \frac{1}{2}M\omega_z^2z^2 + V_G \left(1 - e^{-2(\rho-R)^2/w_\rho^2} \right), \quad (4.8)$$

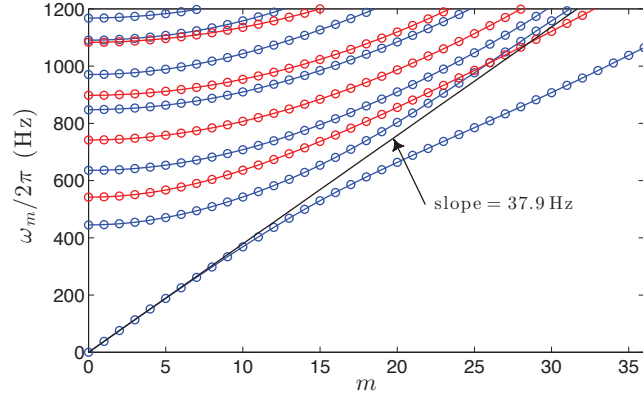


Figure 4.3: **Taken from [4].** The BdG spectrum for the elementary excitations of a ring condensate. The blue (red) curves correspond to the excitation modes that are even (odd) in the axial (z) direction. The lowest branch represents the excitations in the azimuthal direction, the frequency of which is linear at small m (denoted by the black line). The slope determines the orbital frequency of sound $\nu = 37.9(2)$ Hz.

The weak link is not included in the calculations for the Bogoliubov spectrum. In equation 4.8, the first term accounts for the harmonic confinement in the vertical direction (trapping frequency of $\nu_z = 542$ Hz) and the second term accounts for the trapping in the radial direction around a mean radius of $R = 22.4 \mu\text{m}$ and a $1/e^2$ half-width, $w_\rho = 5.5 \mu\text{m}$. The depth of the radial trapping potential is $V_G = 266\text{nK} \times k$, where k is the Boltzmann constant. These parameters have been chosen as they best match the experimental data. The ground state of the condensate is symmetric about the z direction, which reflects the symmetry of the trapping potential. The ground state wavefunction has a azimuthal dependence which scales as $\sim e^{im\phi}$, where $\phi = \arctan(y/x)$ is the conventional azimuthal angle of a two-dimensional coordinate

system and m is an integer, denoting the mode number. The lowest energy solution scales as $\omega_m \sim m\sqrt{g\bar{n}/MR^2}$, where \bar{n} is the mean condensate density and R is the mean radius of the ring [74]. These solutions show that there exists a family of discrete phonon-like modes that propagate azimuthally with the characteristic speed of sound of the ring condensate,

$$c = \sqrt{g\bar{n}/M}. \quad (4.9)$$

Fig. 4.3 shows the calculated the energy spectrum of elementary excitations by solving the BdG equations. The linear dependence at small m is clear. Using the experimental parameters of Sec. 4.3, a linear fit at small values of the mode number m provides a phonon orbital frequency of $\nu = 37.9(2)$ Hz.

4.5 Driving and Probing the Excitations

According to the BdG calculations shown in the previous section, the orbital frequency of phonons for the experimental parameters of our system is 37.9 Hz. We performed experiments to confirm these calculations. As mentioned earlier, the drive can take two forms. The harmonic drive results from a modulation of intensity of the weak link, which takes the form $V_b(t) = V_0 + V_a \sin(2\pi\nu_q t)$. Here $V_0/\mu = 0.54(5)$ is the mean strength of the weak link as a fraction of the chemical potential, $V_a = 0.95 V_0$ is the modulation amplitude as a fraction of the mean value of the weak link, and $\nu_q = q\nu$ is the frequency at which the weak link strength is modulated. The uncertainty in the weak link strength comes the the uncertainty in the chemical potential. The intensity of the laser beam is locked to the desired value

using a servo loop. During the experiment, the weak link is turned on in 300 ms. The chemical potential of the atoms in the ring sets an intrinsic natural timescale on which the system responds to an external perturbation. The turn on time of the weak link should be much larger than this intrinsic timescale to ensure adiabaticity, creating as few excitations as possible. To measure the time evolution of the density in the ring, the drive frequency is set to both integer and half integer values of the orbital angular frequency. The variable used to characterize the density evolution is the 1d number density around the ring as a function of the azimuthal angle. The 1d number density at a given time is normalized with the 1d number density when the weak link was absent. We use both numerical and experimental methods to study this time evolution. In numerical simulations, the 1d number density is obtained by integrating the density along the vertical and the radial directions. In the experimental data, 1d number density is obtained by integrating the density along the radial direction, and the absorption images integrate the optical density along the vertical direction. Figure 4.4 shows the time evolution: panel a-d show the numerical time evolution for $q = 1/2, 3/2, 1, 2$ respectively, while panel e shows the experimental time evolution for $q = 1$. The experimental data is for a time $t \approx 15.5T$ to $t \approx 19T$, since the standing wave patterns observed during resonance takes some time to form in a real experimental setup. As mentioned earlier, in the case of $q = 1$ and $q = 2$, the ‘ring modes’ are on resonance. The experimental data (Fig. 4.4e) shows the resonant $q = 1$ mode, which is consistent with the GPE simulation (Fig. 4.4c). In all of the images, red shows regions of higher relative density compared to a unperturbed trap, while the blue shows regions of lower

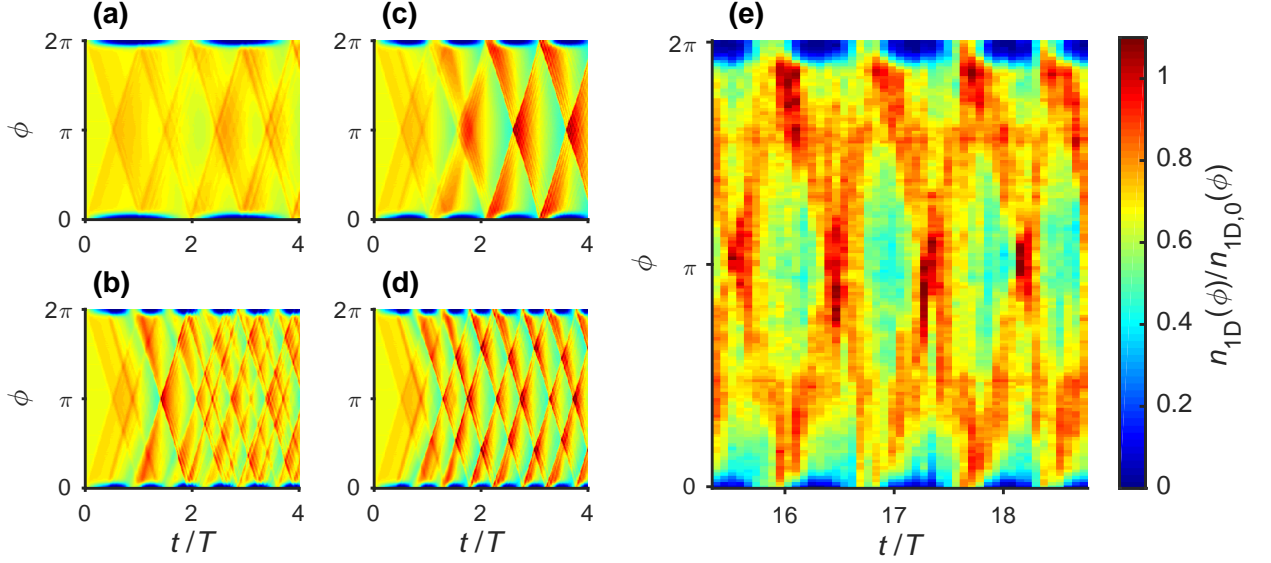


Figure 4.4: **Figure taken from [4].** Time evolution of phonon wavepackets generated through amplitude modulation of the barrier (see Fig. 4.1). The normalized 1D density (colorbar) shows wavepackets, or localized regions of high density, moving around the ring (azimuthal coordinate ϕ) with time t . The density also shows the barrier oscillating at $\phi = 0$ with frequency $\nu_q = q\nu$. Modes with $q = 1/2$ (a) and $q = 3/2$ (b) are nonresonant; modes with $q = 1$ (c and e) and $q = 2$ (d) are resonant. This corresponds to the ‘ring’ modes.

relative density.

The second method to drive the toroidal superfluid is to change the position of the weak link in a harmonic way, such that the azimuthal position of the weak link is given by $\phi_b(t) = \phi_0 + \phi_a \sin(2\pi\nu_q t)$, where $\phi_0 = 0$ is the average position of the maximum height of the barrier, ϕ_a is the amplitude of modulation, and $\nu_q = q\nu$ is the drive frequency. We keep the amplitude of the harmonic modulation such that the maximum velocity reached during oscillation is independent of the drive

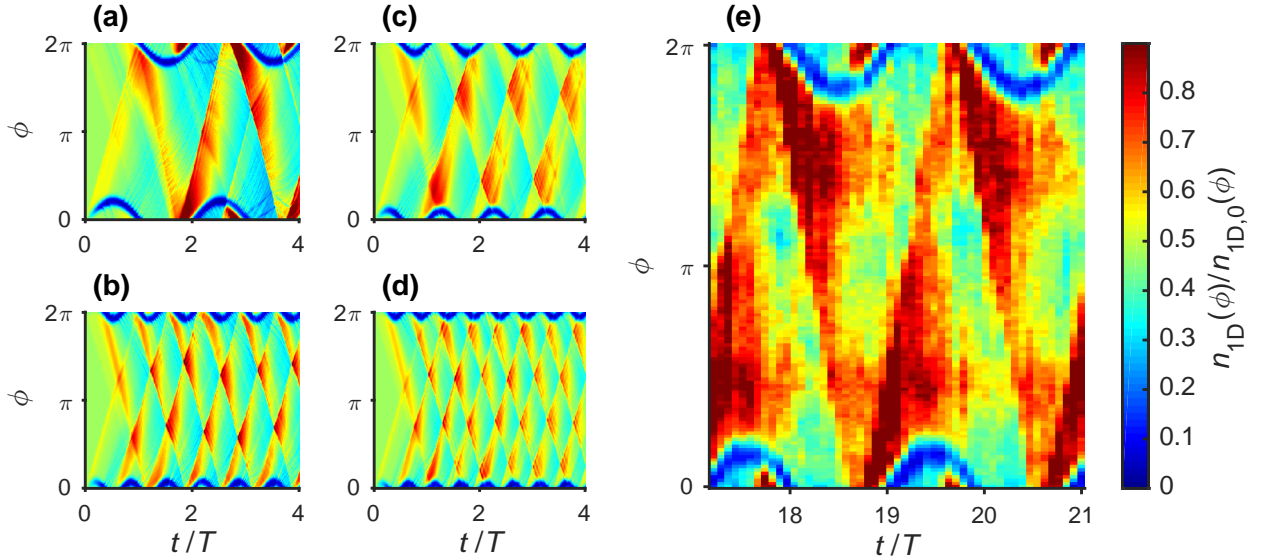


Figure 4.5: **Figure taken from [4].** Time evolution of phonon wavepackets generated through position modulation of the barrier (see Fig. 4.2). The normalized 1D density (colorbar) shows wavepackets, or localized regions of high density, moving around the ring (azimuthal coordinate ϕ) with time t . The density also shows the barrier oscillating about $\phi = 0$ with frequency $\nu_q = q\nu$. Modes with $q = 1/2$ (a and e) and $q = 3/2$ (b) are resonant; modes with $q = 1$ (c) and $q = 2$ (d) are nonresonant. This corresponds to the ‘box’ modes.

frequency. We keep this maximum angular velocity to be $2\pi\nu_q\phi_a = 80$ rad/s. The time evolution of the numerical simulations and the experimental data is shown in 4.5. Panels a-d are results of the numerical simulation, which show the time evolution with the parameter $q = 1/2, 3/2, 1$ respectively. Panel (e) in the figure shows the time evolution for the case $q = 1/2$. The intensity of the weak link is kept fixed at $V_0/\mu = 0.65(7)$, where μ is the chemical potential. As explained in the previous section, the energy of the phonon wavepacket is amplified when the drive frequency is half integer multiple of the orbital frequency. In this case, the direction of the motion of the weak link launching a new phonon and a phonon completing a revolution around the ring are the same.

In figures 4.5 and 4.5, we looked for the appearance of resonances due to the harmonic driving by looking at the appearance of standing waves in the 1d density profile. Next, we looked for another signature of resonances, i.e. the loss of atoms from the trap. When the drive frequency matches the resonance, the weak link adds kinetic energy to the atoms and they may leave the trap once they gain enough energy. While the time evolution data presented above was for time scales on the order of $20 T$, the loss spectra was taken by keeping the modulation (in frequency and position) on for much longer, on the order of 2 s, which corresponds to $\approx 50 T$. We count the number of atoms remaining in the ring trap and compared them to the atoms in the ring trap before the modulation begins. This procedure is repeated for a range of frequency, enabling us to obtain an atomic loss spectra. We also monitor the number of atoms in the disk trap to make sure the loss features are not due to technical noise. The atom loss spectra for the weak link strength modulation is

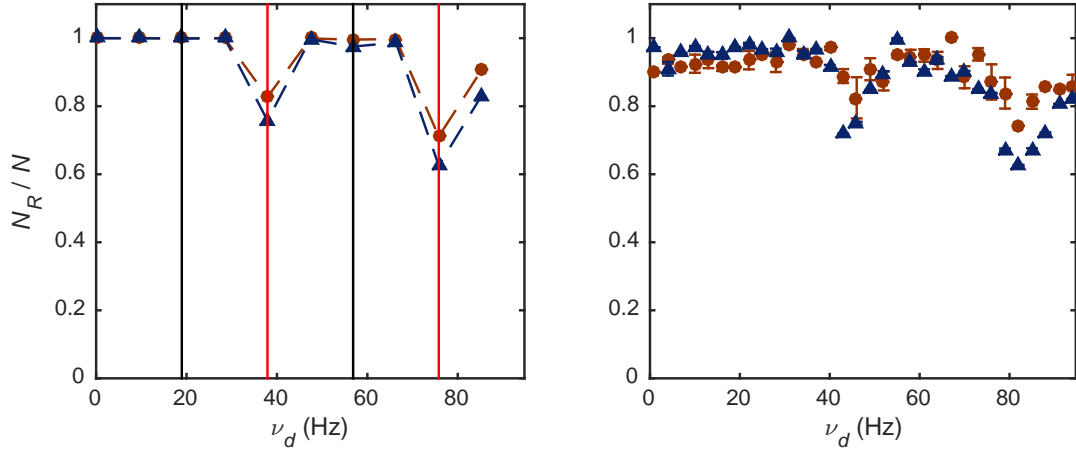


Figure 4.6: **Figure taken from [4].** Atomic loss spectra for an intensity modulated weak link. The numerical simulations are on the left and the experimental values are on the right. These results are for a weak link with a mean strength of $V_0/\mu = 0.30(2)$ (blue triangles) and $V_0/\mu = 0.50(4)$ (red circles). The y axis is the fraction of atoms N_R/N that remain in the trap after 2 s of excitation. The vertical black (red) lines correspond to the resonant frequencies of the box (ring) modes. The dashed lines are a guide to the eye.

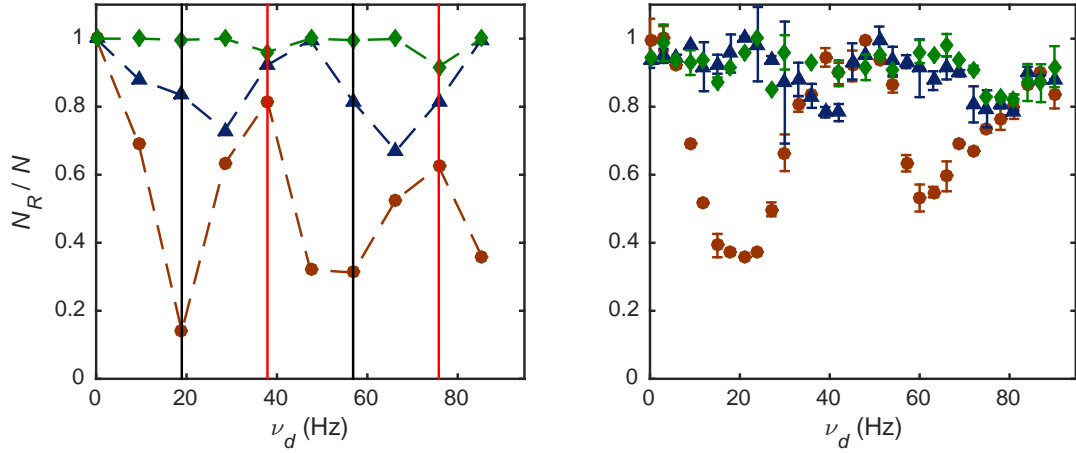


Figure 4.7: **Figure taken from [4].** Atomic loss spectra for a position modulated weak link. The numerical simulations are on the left and the experimental values are on the right. These results are for weak link heights of $V_0/\mu = 0.15(1)$ (green diamonds), $V_0/\mu = 0.30(2)$ (blue triangles), and $V_0/\mu = 0.60(4)$ (red circles), with ν_d being the drive frequency. The y axis is the is the fraction of atoms N_R/N that remain in the trap after 2 s of excitation. The vertical black (red) lines correspond to the resonant frequencies of the box (ring) modes. The dashed lines are a guide to the eye.

shown in figure 4.6.

The modulation of the weak link strength was done at two different mean weak link strengths, $V_0/\mu = 0.30(2)$ and $0.50(4)$, even though the oscillation strength is kept constant at $V_a = 0.25V_0$ (Here, as before, the uncertainty applies only to the experiment.). We confirm that both the experimental and numerical atomic loss spectra show resonance peaks at drive frequencies corresponding to $q = 1$ and $q = 2$. The location of the peaks in the experiment indicates $\nu \approx 41$ Hz, slightly larger than that predicted by theory. This small discrepancy may be due to uncertainty in atom number, trapping frequencies, or other experimental parameters. In contrast, the position modulation atomic loss spectra (shown in figure 4.7) was taken by taking the data at a weak link strengths of $V_0/\mu = 0.15(1)$, $0.3(2)$, $0.6(4)$. As V_0 is increased, both the experiment and the simulation show initial peaks at $q = 1$ and $q = 2$ that shift to $q = 1/2$ and $q = 3/2$. This corresponds to a transition from the ring modes being resonant to the box modes being resonant.

4.6 Generation of supersonic shock waves

While we have used standing phonon waves and atomic loss spectra to measure the sound speed for our system, other groups have used different experimental techniques to measure the sound speed. One of these techniques involves turning on a laser beam in the middle of a cigar shaped condensate [75]. In this paper, a repulsive potential is switched off in under 1 ms, which is timescale shorter than that associated with the chemical potential. The sound speed was then measured from

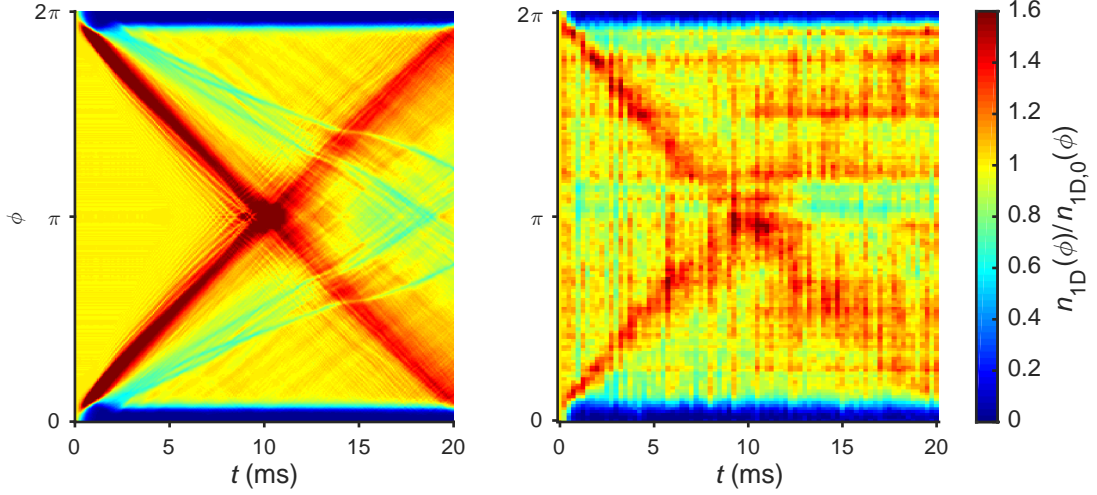


Figure 4.8: **Figure taken from [4].** The above figure shows the azimuthal 1d density normalized to the background density for a supersonic flow in a BEC. To create the shock wave, the weak link is turned on non-adiabatically with a $100 \mu\text{s}$ ramp. The normalized density is shown vs. time. The numerical solution is on the left and the experimental measurement is on the right.

the propagation of the density wave in the body of the condensate. The measured speed of the density wave launched showed good agreement with the Bogoliubov theory. We repeated the same experiment in attempt to measure the sound speed in our system, and found that a rapidly turned on laser beam launches two counter-propagating density waves with an orbital frequency of $\nu \approx 50 \text{ Hz}$, which is about 25% greater than the orbital frequency of sound. This was a clear signature of supersonic flow in our system, which caused shock waves in the superfluid. Due to the periodic nature of the toroidal geometry, we could also observe the collisions between two shock waves.

The formation of supersonic flow [70, 76–81] and shock waves is a widely stud-

ied phenomenon in a condensate, both experimentally and numerically. A recent experiment reports the experimental observation of analogue Hawking radiation for a supersonic flow in a BEC [82]. The presence of shock waves in BECs was predicted by [83–85], while they were shown to exist experimentally in [86, 87]. The results in the papers above show that as a laser beam is turned on rapidly, density waves are launched. The density profile of the atoms participating in the density wave can be modeled as a Gaussian. The work by [85] showed that when a laser impulse is used to launch a density wave, the maxima of the density wave will move faster than the minima of the density wave. This causes the density profile to become asymmetric and become tilted towards the direction of propagation. This steepening of the density profile gives rise to a shock wave. These shock waves are dispersive, and may break up into excitations like solitons and vortex rings.

The experimental parameters were used for a TDGPE calculation, the results of which are presented in the left panel of figure 4.8. The simulations show that the leading density waves traveling at supersonic speeds, while secondary density waves traveling at the sound speed. The simulations also show that the shock waves maintain much of their shape after collision, which is not the case in the experiment. The simulations also show some density waves moving at a speed lower than the sound speed, which may be gray solitons. We do not see this in the experimental data either.

4.7 Summary

We have investigated the excitations of a ring-shaped condensate with a perturbation modulated in both position and amplitude. This perturbation, in the form of a weak link, generates phonon wavepackets that travel around the ring at the speed of sound. These wavepackets have an orbital angular frequency $\nu = c/(2\pi R)$. We find that these wavepackets are resonant with an amplitude-modulated perturbation if the perturbation's frequency is an integer multiple of orbital frequency of the phonon, ν . For position modulation, the wavepackets are in resonance if the frequency of the perturbation is a half-integer multiple of ν . The difference in these cases corresponds to the symmetry of the drive: an amplitude modulation creates two oppositely moving wavepackets at the same time, whereas position modulation creates two oppositely moving wavepackets at points in its motion that are out of phase by π . By looking at atom loss as a function of drive frequency, we verify these resonance conditions.

This work has implications for other atomtronic devices. For example, one should be able to induce a Shapiro resonance [88, 89] in ultracold atoms by driving a weak link perturbation in a way similar to that done here. In addition, phonon modes can be excited and controlled for future applications, such as phonon interferometry [64] and the detection of circulation states of a ring [40]. In the strongly reflecting regime, phonon wavepackets undergo similar time evolution as particles in a shaken box [90, 91], and thus could be useful for future studies of quantum chaos and Fermi acceleration [92, 93].

Chapter 5: Minimally destructive, Doppler measurement of a quantized, superfluid flow

In this chapter, we study how the circulation state of the persistent current can be determined without releasing the toroidal condensate in time of flight. We use the Doppler effect, the shift in the frequency of sound due to motion, for this measurement. We imprint phonon modes on the condensate. A persistent current shifts the frequency of the phonon modes due to the Doppler effect. This frequency shift will cause a standing-wave phonon mode to be ‘dragged’ along with the persistent current. The content of this chapter is based on the following published work [5].

1) “Minimally destructive, Doppler measurement of a quantized flow in a ring-shaped Bose-Einstein condensate”, A Kumar, N Anderson, W D Phillips, S Eckel, G K Campbell, and S Stringari, *New Journal of Physics*, 18, 025001 (2016).

I contributed to the experimental data acquisition and analysis.

5.1 Overview

Ring-shaped Bose-Einstein condensates (BECs) use topology to exploit one of the key features of a BEC: superfluidity. In particular, the topology supports superfluid persistent currents [94]. As a result, a ring-shaped condensate forms the basis of several so-called ‘atomtronic’ devices: simple circuits that resemble counterparts in electronics [49,61,62,65,95]. The addition of one or more rotating perturbations or weak links into the ring can form devices that are similar to the rf-superconducting quantum interference device (SQUID) [49,61,62] and dc SQUID [65,95]. Operation of these devices typically requires measuring the persistent current. Here, we present a technique for measuring the persistent current of a ring that uses the Doppler effect and, unlike other methods, is done *in-situ* and can be minimally destructive.

Superfluids can be described using a macroscopic wavefunction (or order parameter) $\psi = \sqrt{n}e^{i\phi}$, where n is the density of atoms and ϕ is phase of the wavefunction. In this picture, the flow velocity is given by $v = (\hbar/m)\nabla\phi$, where m is the mass of the atoms and \hbar is the reduced Planck’s constant. Because the wavefunction must be single valued, the integral $\oint \nabla\phi \cdot dl$ must equal $2\pi\ell$, where ℓ is an integer called the winding number. This quantization of the winding number forces flows around a ring of radius R to be quantized with an angular velocity $\Omega_0 = \hbar/mR^2$. Thus, the angular flow velocity must satisfy $\Omega = \ell\Omega_0$.

In addition to supporting bulk persistent flows, the BEC also serves as a medium in which sound can travel. Because of the trap’s boundary conditions, only certain wavelengths of sound are permitted. These phonon, or Bogoluibov, modes

are the lowest energy collective excitations of the condensate [96, 97]. In this work, we excite a standing wave mode with wavelength $\lambda = 2\pi R$, as shown in Fig. 5.1(a-b). Such a standing wave is an equal superposition of clockwise and counterclockwise traveling waves with the same wavelength. In the presence of a background flow, the Doppler effect shifts the relative frequencies of the two traveling waves. This shift causes the standing wave to precess, as shown in Fig. 5.1(c). Here, we use this precession to detect the background flow velocity of the superfluid. This method is analogous to earlier techniques, where the precession of a quadrupole oscillation was used to measure [98, 99] the sign and charge of a quantized vortex in a simply connected, harmonic trap, as suggested in Refs. [100, 101].

In a ring-shaped condensate, two other methods have been used to measure the background flow velocity by determine the winding number ℓ . Both are inherently destructive because they require that the BEC be released from the trap. First, sufficient expansion of the condensate can yield a hole at the center of the cloud whose size is quantized according to ℓ [102–105]. Second, experiments releasing both a ring and a reference condensate produce spiral interference patterns that indicate ℓ [50, 106].

Our method of detecting rotation by the Doppler effect is sufficiently precise to distinguish adjacent values of ℓ . However, it is minimally disruptive: it requires only exciting a sound wave and imaging the resulting density modulation. By imaging the density modulation using a minimally destructive imaging method (such as dark-field dispersion imaging [107], phase contrast imaging [108], diffraction-contrast imaging [109], partial transfer absorption imaging [48], or Faraday imag-

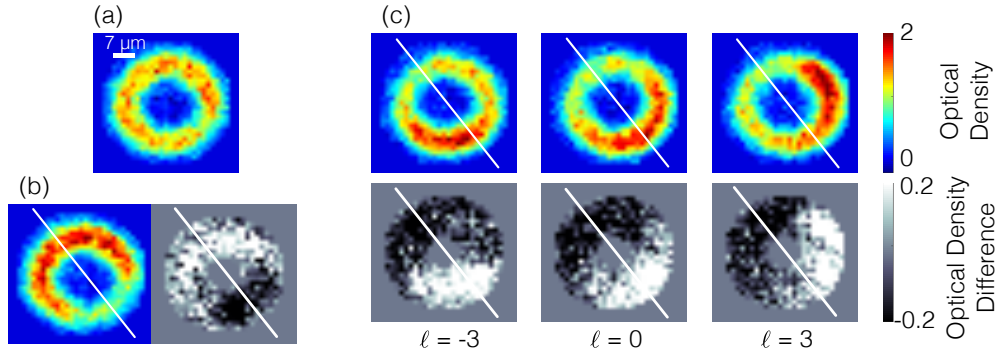


Figure 5.1: **Taken from [5].** (a) Image of the ring condensate *in-situ* without an applied perturbation. (b) A sinusoidal perturbation excites a standing-wave superposition of counterpropagating phonon modes. The white line intersects the ring at the maximum and minimum of the perturbation. The left image shows the density; the average density is subtracted from the right image. These images show the resulting density modulation, 100 μ s after the perturbation has been removed. (c) Full density (top) and average-subtracted-density (bottom) images taken 9.1 ms after removal of the perturbation. The density modulation rotates relative to the initial perturbation in the presence of superfluid flow. The winding numbers are shown below the images.

ing [110]) one can create a winding number measurement that is also minimally destructive. Such measurements could allow easier implementation of experiments where rings are stirred by weak links more than once, such as hysteresis experiments. By measuring the winding number in a minimally destructive way, the quantum state of the ring can be known after each stage of stirring. One can use multiple minimally-destructive winding number measurements to increase the sensitivity of a rotation sensor based on the atomtronic rf-SQUID. Our system [62] has a sensitivity of ≈ 0.1 Hz for a measurement done once every ≈ 30 s, which includes creating the condensate, stirring, and measuring the winding number. This leads to an effective sensitivity to rotation of ~ 5 Hz/ $\sqrt{\text{Hz}}$. By repeating stirring and winding number measurement on a single condensate using a minimally-destructive technique (which yields the same information as a destructive measurement), the sensitivity improves by $\sqrt{N_{\text{meas}}}$, where $N_{\text{meas}} \approx 10$ is an achievable number of minimally-destructive measurements.

Finally, it is possible to use this technique to detect rotations of the inertial frame of the condensate itself, using the Sagnac effect¹. Ref. [64] measured the noise level associated with such an excitation-based rotation sensor, finding a sensitivity in their system of roughly 1 (rad/s)/ $\sqrt{\text{Hz}}$. However, their experiment was not configured to produce rotation, so the effect was not measured experimentally. Here, we demonstrate the feasibility of this idea, by detecting the quantized rotation of

¹ We note that unlike the ring-shaped condensate considered here, not every mode in a simply connected condensate is sensitive to both a rotating frame and to vorticity. In particular, the dipole oscillation mode is sensitive to a rotating frame but not sensitive to vorticity [100].

the superfluid in the ring itself.

5.2 Theory

To understand the Doppler effect and its effect on phonons in the ring, let us first consider a standing-wave phonon mode in the absence of a persistent current. To simplify the calculation, let us consider the equivalent problem of a 1D gas of length $2\pi R$, where R is the radius of the ring, and let us impose periodic boundary conditions. A standing wave mode can be generated by a perturbation of the form $V = V_0 \cos(q\theta)$, where q is a positive integer, V_0 is the amplitude of the perturbation, and θ is the azimuthal angle. This perturbation generates a modulation in the density of the form $n_{1D}(\theta) = n_{\text{eq}} + \delta n \cos(q\theta)$, where n_{eq} is the equilibrium density without the perturbation and δn is the amplitude of the density modulation. Upon sudden removal of the perturbation, the density $n_{1D}(\theta)$ is projected onto the spectrum of phonon modes. The initial density modulation is then described by the superposition of two counterpropagating modes $\cos(\omega(q_{\pm})t - q_{\pm}\theta)$. Here, q_+ indicates a mode traveling counterclockwise and q_- indicates a mode traveling clockwise. In the absence of a persistent current the two modes have equal frequency: $\omega(q_{\pm}) = \omega_0$. Consequently, the density modulation will oscillate in time, $\delta n(t) \propto \cos(\omega_0 t) \cos(q\theta)$, without exhibiting precession.

The presence of the current will remove the degeneracy between the two modes through the Doppler effect. The frequency of the two modes, in the presence of a

superflow of velocity $v = \ell\Omega_0 R$, will be given by

$$\omega(q_{\pm}) = \omega_0 \pm \frac{q}{R}v. \quad (5.1)$$

The density modulation is then proportional to

$$\begin{aligned} & \cos[q_+\theta - \omega(q_+)t] + \cos[q_-\theta + \omega(q_-)t] \\ &= \cos\left[q\left(\theta - \frac{v}{R}t\right)\right] \cos(\omega_0 t) \end{aligned} \quad (5.2)$$

and hence evolves in space. The azimuthal location ϕ_m of an anti-node of this density standing wave precesses around the ring as

$$\frac{d\phi_m}{dt} = \frac{\ell\hbar}{mR^2}. \quad (5.3)$$

Measurement of $\phi_m(t)$ would consequently provide a direct measurement of ℓ . We note that $d\phi_m/dt$ does not depend on ω_0 ; therefore, the speed of sound and the details of the phonon dispersion curve are not relevant in predicting the precession.

While the above arguments may seem to apply only to a ring, they can easily be generalized to any quasi-one-dimensional geometry. In such a case, the shifts in the phonon frequencies will still be given by Eq. 5.1, but with a v that may or may not be quantized. For an infinite one-dimensional channel, for example, the flow is not quantized. However, two equal but oppositely directed phonon wavepackets (similar to those generated in Ref. [4]) traveling in the channel will move with different velocities in the presence of a background flow. The use of a ring allows for a straightforward means of detecting the frequency shift: precession of a phonon standing-wave mode.

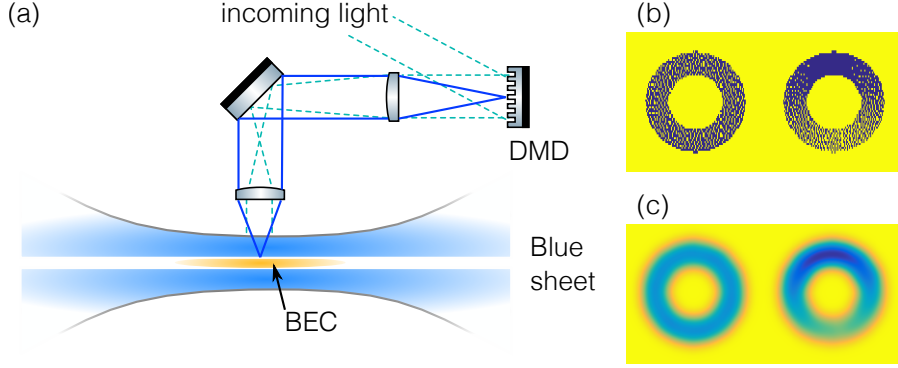


Figure 5.2: **Taken from [5].** (a) Schematic of the setup used to trap the atoms and create the double ring potential and sinusoidal perturbation. A DMD is illuminated with blue-detuned light and is imaged onto the atoms using a telescope (solid lines) , which ensures that incoming collimated beams remain collimated after they emerge from the telescope (dashed lines). (b) The halftoned patterns \parallel written to the DMD for the bare ring potential (left) and the perturbed ring potential (right). (c) After convolution with the point-spread function of the imaging system, the potentials formed are smooth, and show a clear sinusoidal perturbation (right).

5.3 Experimental details

We create a ^{23}Na condensate in a crossed-optical dipole trap, as shown in Fig. 5.2a. A blue-detuned double sheet beam, formed by focusing a TEM_{01} mode tightly along the vertical direction, provides vertical confinement. Confinement in the horizontal plane is generated using another blue detuned beam that is shaped using a Texas Instruments LightCrafter 3000 digital micromirror device (DMD) ².

²The identification of commercial products is for information only and does not imply recommendation or endorsement by the National Institute of Standards and Technology.

We position the DMD in our imaging system to directly image the surface of the DMD onto the atoms. (This method is similar to the photomask method used in Ref. [71], with the DMD replacing the photomask.)

The DMD generates a double ring trap. These experiments use only the inner ring, which is shown in Fig. 5.1(a). In general, our condensates contain $\approx 7 \times 10^5$ atoms, with approximately 5×10^5 in the outer ring and 2×10^5 in the inner ring. The outer ring, with mean radius $31(1) \mu\text{m}$ ³, can be used as a phase reference to measure the winding number of the inner ring [111]. The inner ring has a chemical potential of $\mu/h = 3.1(6)$ kHz. The vertical trapping frequency is $1020(30)$ Hz and the radial trapping frequency in the inner ring is $310(10)$ Hz.

In order to generate a persistent current in our ring, we apply a rotating potential generated by a blue-detuned beam steered by an acoustic-optic deflector (AOD). A previous paper [62] describes this stirring technique. We verify that this produces the desired ℓ state 95% of the time by performing a fully-destructive interference measurement [50]. The phase winding in the inner ring can be measured by interfering the inner ring with the outer ring condensate, which serves as a phase reference. Fig. 5.2(d) shows a typical interference pattern, which indicates $\ell = -1$. (We note that the chirality of these spirals for a given sign of the winding number is opposite of those in Ref. [50], because the reference condensate is on the outside rather than the inside of the ring.)

In addition to generating the static trap, the DMD can also produce perturba-

³Unless stated otherwise, uncertainties represent the 1σ combination of statistical and systematic errors.

tions to the potential. However, because any individual mirror is binary (either on or off), potentials that require intermediate values require a form of grayscale control. We achieve such control by using Jarvis halftoning [112]. Because the point-spread function of our imaging system (in the plane of the atoms, $\approx 6 \mu\text{m } 1/e^2$ full-width) is much larger than the DMD pixel size (in the plane of the atoms, $\approx 0.5 \mu\text{m}$), the potential at any given location is the convolution of the binary values of all the nearby pixels with the point spread function. For example, Fig. 5.2(b) shows a halftoned pattern written to the DMD for generating a sinusoidal perturbation of the form $V_0 \sin(\theta)$ ⁴. Convolution with the point-spread function generates the desired sinusoidal potential, as shown in Fig. 5.2(c).

We empirically find that a perturbation of $V_0 \approx 0.4\mu$ applied for 2 ms is sufficient to excite the first phonon mode without perturbing the flow state of the ring. The speed with which our perturbation can be turned on and off is limited by the refresh rate of our DMD to 250 μs . To image the resulting density modulation *in-situ*, we use partial transfer absorption imaging (PTAI) [48], which is a type of minimally-destructive imaging [113]. In general, we transfer approximately 5% of the atoms into the imaging state. Despite the method being minimally destructive, none of the experiments contained in this work use repeated imaging on the same condensate.

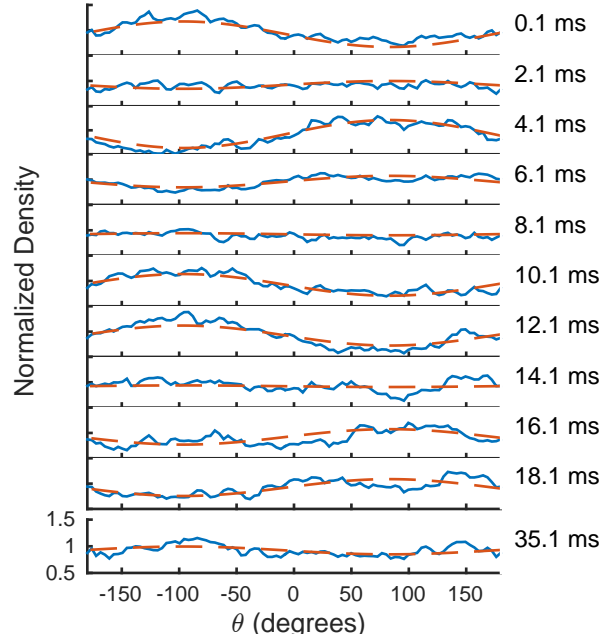


Figure 5.3: **Taken from [5].** Plot of the normalized 1D density of the ring $n_{1D}(t, \theta)/n_{0,1D}(\theta)$ (see text) vs. angle, for different times after the perturbation. The solid blue lines show the experimental data and the red dashed lines show the fit to the data. Each trace represents one shot of the experiment. For these data, there is no persistent current present ($\ell = 0$).

5.4 Results

To detect rotation accurately in the ring, the behavior of the phonon mode in the absence of a persistent current must first be understood. To this end, we apply our perturbation to the inner ring and observe the resulting oscillation in the phonon mode, without a persistent current ($\ell = 0$). Shown in Fig. 5.3 is the normalized 1D density $n_{1D}(t, \theta)/n_{0,1D}(\theta)$, where $n_{1D}(t, \theta)$ is the 1D density measured a time t after the perturbation was applied and $n_{0,1D}(\theta)$ is the 1D density separately measured with no perturbation applied. The density n_{1D} is determined via $\int n_{2D}(t, r, \theta) r dr$, where the 2D density $n_{2D}(t, r, \theta)$ is determined from imaging followed by interpolated conversion into polar coordinates. The Bogoliubov mode oscillates with time in the ring, but is also damped (as discussed below). At $\theta \approx \pm 90^\circ$, maxima and minima appear immediately after the perturbation. At these angles, clear oscillations are seen as a function of time. At the nodal points $\theta \approx 0^\circ, 180^\circ$, oscillations are expected to be absent in a perfectly uniform ring.

We fit the data to the function $ae^{-t/\tau} \sin(\omega t + \phi_1) \sin(\theta + \phi_2) + c$, where a , τ , ω , $\phi_{1,2}$, and c are fit parameters. The average best fit value of the oscillation frequency is 79.3(3) Hz. We can estimate the frequency of this fundamental phonon mode as $\omega_0 = c_s/R$, where c_s is the speed of sound. Using the speed of sound for a narrow channel $c_s = \sqrt{\mu/2m} = 5.3(5)$ mm/s [74] yields $\omega_0/2\pi = 74(7)$ Hz, in good agreement with the average best fit value. The average best fit value of the decay constant is $\tau = 25.6(1)$ ms, so that by 100 ms, the oscillation amplitude is

⁴The halftoning is more evident if one zooms in on Fig. 2b.

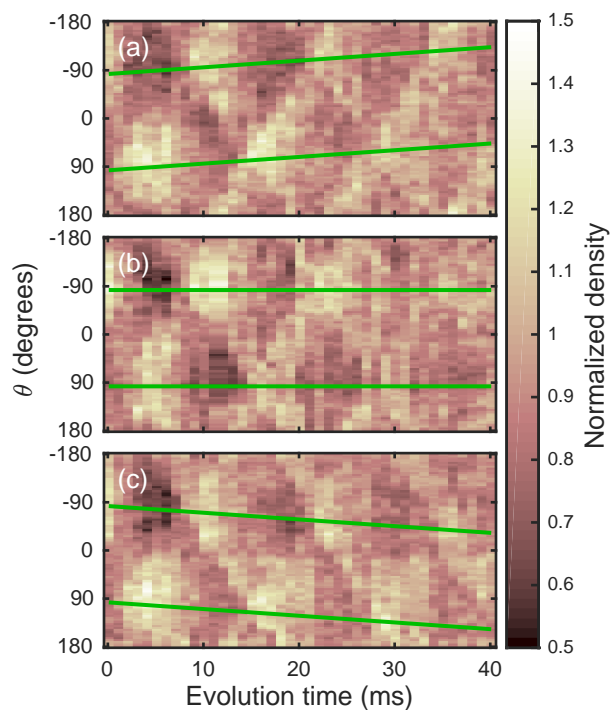


Figure 5.4: **Taken from [5]**. Plot of the normalized 1D density as a function of azimuthal angle and hold time after the perturbation. The three panels correspond to having different persistent currents in the ring: (a) $\ell = -1$, (b) $\ell = 0$, and (c) $\ell = 1$. For each time and winding number, there is one experimental shot (i.e., there is no averaging). The green lines show the expected precession of the antinodes of the standing wave, according to Eq. 5.3.

diminished well below the noise.

The decay of oscillation could be caused by a number of effects, including Landau damping and Beliaev damping, i.e., four-wave mixing. We expect Landau damping to thermalize our excitations by scattering from other, thermal, phonons [114]. In this case, we expect that the quality factor $Q = \omega\tau$ will be independent of the mode number q [64]. By contrast, damping via four-wave mixing, called Beliaev damping, will result in a strong dependence of Q on mode number [64,115]. Landau damping should also depend on the temperature, while Beliaev damping should depend on the density, but we have not explored these dependencies ⁵. Nevertheless, we observe a Q for the $q = \pm 1$ mode superposition of 12.8(6). We also investigated the decay of the $q = \pm 2$ mode, which has a Q of 13.8(4), agreeing within the uncertainties with the Q for the decay of the ± 1 . Therefore, Landau damping appears to be favored over Beliaev damping as the dominant damping mechanism.

Having studied the relevant features of the phonon mode without a persistent current, we can now use Eq. 5.3 to predict the precession of the anti-nodes and nodes in the presence of a persistent current. The antinode initially at $\theta = -90^\circ$ reaches maximum density at approximately 10, 24, and 35 ms; the antinode initially at $\theta = 90^\circ$ reaches maximum density at approximately 5, 17, and 29 ms (see Fig. 5.4) ⁶. At these times, the location of these antinodes is determined by Eq. 5.3. Shown in

⁵Furthermore, it is not clear if the phonon spectrum in one-dimension will fulfill momentum conservation in a four-wave mixing process.

⁶The maximum contrast of the standing wave does not occur at time $t = 0$ because of the details of how the perturbation is applied.

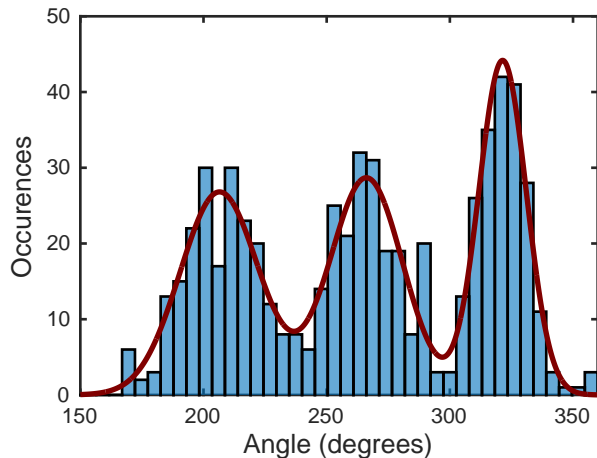


Figure 5.5: **Taken from [5]**. Histogram of the number of occurrences of measured precession angles of one of the antinodes of the standing wave at $t = 35.1$ ms. The red curve is a fit of three, independent Gaussians. These Gaussians correspond to three different winding numbers: $\ell = -1$, $\ell = 0$, and $\ell = 1$ (left to right).

Fig. 5.4(a), (b), and (c) are the cases where the winding number in the ring prior to the perturbation was $\ell = +1$, 0, and -1 , respectively. Given the radius of the ring, we expect that these peaks should move at rate of $\ell\hbar/mR^2t = [\ell \times 1.25(7) \text{ deg/ms}]t$. This rate is shown by the green lines in Fig. 5.4, and follows the peaks well.

To detect a flow velocity with sufficient precision to distinguish between adjacent winding numbers using a single image, one needs to balance the observation time with the signal to noise ratio. While the angular deflection grows linearly with time, the amplitude of the oscillation, and thus its signal to noise, decreases roughly exponentially with time. Empirically, we find that time $t = 35$ ms is the best compromise; here, the difference in deflection for $\Delta\ell = 1$ is expected to be $\approx 45^\circ$. To test our ability to determine a given winding number with a single image,

we fit the maximum of the density profile for 614 individual repetitions initialized with winding numbers $\ell = 0, -1$ or 1 . We bin the results to form a histogram, shown in Fig. 5.5. The histogram shows three clear peaks, which we fit to Gaussians. Each corresponds to one of the three winding numbers. Each has a slightly different width because of the compression or expansion of the phonon wave in the azimuthally varying density profile of the ring.

We can use the Gaussian fits to predict the confidence with which we can assign a winding number. Given the strong overlap of adjacent Gaussians, we have a confidence of $\approx 90\%$ of identifying a $\ell = -1$, and a confidence of $\approx 95\%$ of identifying an $\ell = 1$ state. These confidences can be made better by attempting to make the ring more uniform to keep the form of the oscillation well defined. This might improve the fitting algorithm and decrease the noise. In addition, if the condensate were colder, the damping of the phonon mode should be reduced. This would allow for longer interrogation times and therefore more angular displacement between adjacent ℓ states.

For this this method of measuring winding number to be minimally destructive, one must use a minimally destructive imaging method [113]. Previous experiments [116] show that such imaging methods do not perturb the flow state of BECs. In addition, the perturbation one applies to the condensate must also be minimally disruptive. The observed fast decay helps to ensure this. Perhaps most important, the application of the perturbation must not change the winding number. To verify this, we measured the winding number that results from stirring at multiple different rotation rates using our destructive interference technique. (This produced

data similar to those in Ref. [61].) We then repeated this experiment, but after stirring, applied our sinusoidal perturbation, allowed 100 ms for the ring to settle, and measured the winding number again. The data show no significant change in the winding number as a result of the application of the perturbation.

One might ask if going to higher modes, particularly $q = \pm 2$, would yield better sensitivity to rotation. The frequency of the oscillation increases as q , and because the quality factors of the modes are the same, the time at which one achieves a given signal-to-noise ratio scales as $t \sim q^{-1}$. Because the precession angle scales as $\sim t$, these two factors cancel. However, one might be able to better determine the angular position of the maxima because the width of the oscillation peaks decreases as q^{-1} . Further work is needed to verify these scalings.

5.5 Conclusion

We have demonstrated a minimally destructive *in-situ* method of measuring winding number in a ring-shaped Bose-Einstein condensate. This technique can be used as an excitation-based Sagnac interferometer [64] †. Because of its non-destructive behavior, this method can be applied to a variety of ring experiments, and may possibly be used to increase the sensitivity of atomtronic rotation sensors, by being able to repeat the measurement of winding number many times on a single condensate.

Chapter 6: Temperature induced decay

In this chapter, we study how temperature affects the lifetime of a quantized, persistent current state in a toroidal Bose-Einstein condensate. When the temperature is increased, we find a decrease in the persistent current lifetime. Comparing our measured decay rates to simple models of thermal activation and quantum tunneling, we do not find agreement. We also measured the size of the hysteresis loops in our superfluid ring as a function of temperature, enabling us to extract the critical velocity. The measured critical velocity is found to depend strongly on temperature, approaching the zero-temperature mean-field solution as the temperature is decreased. This indicates that an appropriate definition of critical velocity must incorporate the role of thermal fluctuations, something not explicitly contained in traditional theories. The content of this chapter is based on the following published work [6].

1) “Temperature-induced decay of persistent currents in a superfluid ultracold gas”, A. Kumar, S. Eckel, F. Jendrzejewski, and G. K. Campbell, *Physical Review A*, 95, 021602(R) (2017).

I contributed to the experimental data acquisition and analysis.

We study how temperature affects the lifetime of a quantized, persistent current state in a toroidal Bose-Einstein condensate (BEC). When the temperature is increased, we find a decrease in the persistent current lifetime. Comparing our measured decay rates to simple models of thermal activation and quantum tunneling, we do not find agreement. We also measured the size of hysteresis loops size in our superfluid ring as a function of temperature, enabling us to extract the critical velocity. The measured critical velocity is found to depend strongly on temperature, approaching the zero temperature mean-field solution as the temperature is decreased. This indicates that an appropriate definition of critical velocity must incorporate the role of thermal fluctuations, something not explicitly contained in traditional theories.

6.1 Overview

Persistent currents invoke immense interest due to their long lifetimes, and they exist in a number of diverse systems, such as superconductors [12, 117], liquid helium [118, 119], dilute ultracold gases [49, 94, 120] and polariton condensates [121]. Superconductors in a multiply connected geometry exhibit quantization of magnetic flux, [122] while the persistent current states in a superfluid are quantized in units of \hbar , the reduced Planck constant. To create transitions between quantized persistent current states, the critical velocity of a superfluid (or critical current of a superconductor) must be exceeded. In ultra-cold gases, the critical velocity is typically computed at zero-temperature, whereas experiments are obviously performed

at non-zero temperature. In this work, we experimentally investigate the role of temperature in the decay of persistent currents in ultracold-atomic, superfluid rings (Fig. 1a).

In the context of the free energy of the system, different persistent current states of the system (denoted by an integer ℓ called the winding number) can be described by local energy minima, separated by energy barriers (here, we concentrate on $\ell = 0$ and $\ell = 1$ shown in Fig.1(b)) [31, 35]. The metastable behavior emerges from the energy barrier, E_b , between two persistent current states. For superconducting rings, the decay dynamics have been understood by the Caldeira-Leggett model [123]: the decay occurs either via quantum tunneling through the energy barrier or thermal activation over the top of the barrier. When first investigated in superconductors [30, 124–126], the decay rate from the metastable state Γ was fit to an escape temperature T_{esc} by the relation $\Gamma = \Omega_a \exp(E_b/k_B T_{esc})$, where k_B is the Boltzmann constant. In the context of the WKB approximation in quantum mechanics or the Arrhenius equation in thermodynamics, Ω_a represents the “attempt frequency”: i.e. how often the system attempts to overcome the barrier. The $\exp(E_b/k_B T_{esc})$ represents the probability of surmounting the barrier on any given attempt. The probability and thus the escape temperature in quantum tunneling is independent of temperature, while for thermal activation, the escape temperature tracks the real temperature (Fig 6.1(c)). For our superfluid ring, the energy barrier E_b is much greater than all other energy scales in the problem, hence the lifetime of the persistent current is much greater than the experimental time-scale. However, the height of the energy barrier and the relative depth of the two wells can be

changed by the addition of a density perturbation [35]. The density perturbation may induce a persistent current decay even if its strength is less than the chemical potential [28, 35].

In this thesis, we measure the decay constant of a persistent current for various perturbation strengths and temperatures. We also measure the size of hysteresis loops which allows us to extract the critical velocity, showing a clear effect of temperature on the critical velocity in a superfluid.

The preferred theoretical tool for modeling atomic condensates is the Gross-Pitaevskii (GP) equation, which is a zero-temperature, mean-field theory. Recent experiments exploring the effect of rotating perturbations on the critical velocity of toroidal superfluids have found both agreement [63] and significant discrepancies [28, 35] between experimental results and GP calculations. Several non-zero temperature extensions to GP theory have been developed, including ZNG [127] and c-field [128] [of which the Truncated Wigner approximation (TWA) is a special type]. To explore the role of temperature in phase slips in superfluid rings, Ref. [41] studied condensates confined to a periodic channel using TWA simulations. In addition, recent theoretical [129–135] and experimental [136] works explored a similar problem of dissipative vortex dynamics in a simply-connected trap.

Our experiment consists of a ^{23}Na Bose-Einstein condensate (BEC) in a target-shaped optical dipole trap [2] [Fig. 6.1(a)]. The inner disc BEC has a measured Thomas-Fermi (TF) radius of $7.9(1) \mu\text{m}$. The outer toroid has a Thomas-Fermi full-width of $5.4(1) \mu\text{m}$ and a mean radius of $22.4(6) \mu\text{m}$. To create the target potential, we image the pattern programmed on a digital micromirror device (DMD)

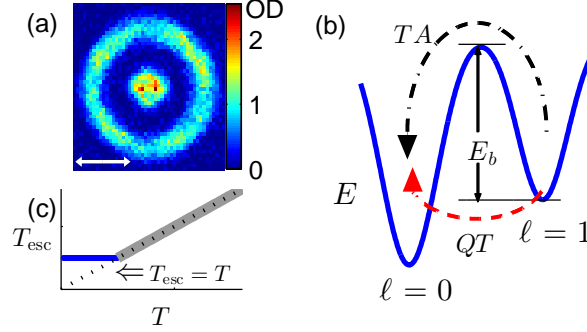


Figure 6.1: **Taken from [6].** Target shaped condensate, energy landscape and effective escape temperature (color online). a) *In situ* image of trapped atoms, with 5% of the total atoms imaged [7]. Experiments are performed on the ring-shaped BEC and the resulting winding number ℓ is read out by interfering the ring condensate with the disc-shaped BEC in time of flight. The disc-shaped BEC acts as a phase reference. (b) Energy landscape showing the stationary state, $\ell = 0$, and the persistent current state, $\ell = 1$, as minima in the potential. The energy barrier E_b needs to be overcome for a persistent current to decay from $\ell = 1$ to $\ell = 0$. The decay can be induced either via thermal activation (TA), or quantum tunneling (QT). (c) Crossover from quantum tunneling to the thermally activated regime. The escape temperature T_{esc} (see text) first remains constant (horizontal blue line) and then becomes equal to the physical temperature T (slanted gray line). A dotted line acts as a guide to the eye depicting $T_{esc} = T$.

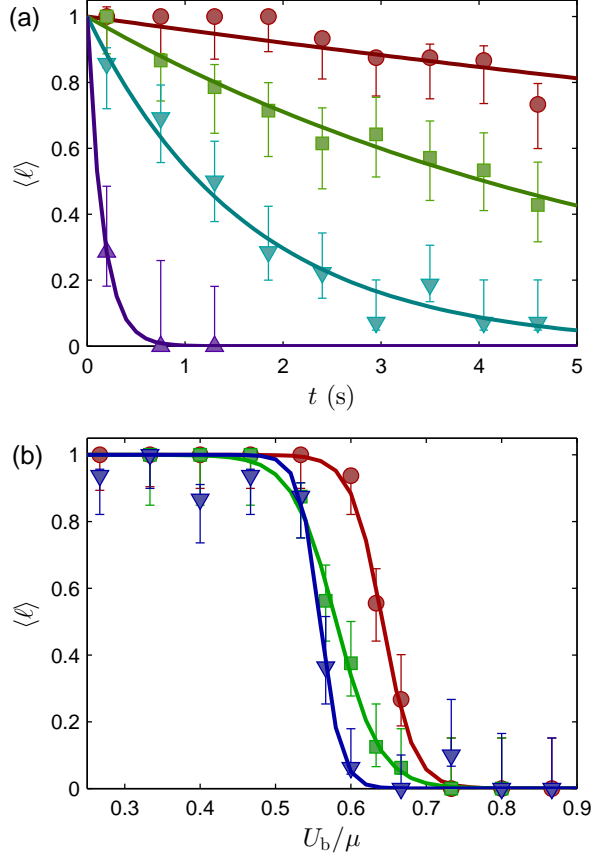


Figure 6.2: **Taken from [6].** (color online). (a) Average measured winding number $\langle \ell \rangle$ vs. t , the duration for which a stationary perturbation is applied. The four data sets correspond to different strengths of the stationary perturbation U_b : $0.50(5)\mu$ (circles), $0.53(5)\mu$ (squares), $0.56(6)\mu$ (inverted triangles) and $0.59(6)\mu$ (triangles). Here, μ is the unperturbed chemical potential. The temperature of the superfluid was $85(20)$ nK. The solid curves show exponential fits. (b) The average measured winding number $\langle \ell \rangle$ vs. U_b for fixed t : 0.5 s (circles), 2.5 s (squares) and 4.5 s (inverted triangles). The solid curves show a sigmoidal fit of the form $\langle \ell \rangle = [\exp((U_b/\mu - \zeta)/\alpha) + 1]^{-1}$. The temperature of the superfluid was $40(12)$ nK.

onto the atoms while illuminating it with blue-detuned light. This allows us to create arbitrary potentials for the atoms. Vertical confinement is created either using a red-detuned TEM₀₀ or a blue-detuned TEM₀₁ beam. The potential generated by the combination of the red-detuned TEM₀₀ beam and ring beam is deeper than that of blue-detuned TEM₀₁ and ring beam; thus the temperature is generally higher in the red-detuned sheet potential. We use this feature to realize four different trapping configurations with temperatures T of 30(10) nK, 40(12) nK, 85(20) nK and 195(30) nK but all with roughly the same chemical potential of $\mu/\hbar = 2\pi \times (2.7(2) \text{ kHz})$. (See supplemental material for details about temperature and trapping configurations.) Finally, a density perturbation is created by another blue-detuned Gaussian beam with a $1/e^2$ width of 6 μm and can be rotated or held stationary at an arbitrary angle in the plane of the trap [58].

To probe the lifetime of the persistent current, we first initialize the ring-shaped BEC into the $\ell = 1$ state with a fidelity of 0.96(2) (see Supplemental material). A stationary perturbation with a strength $U_b < \mu$ is then applied for a variable time t ranging from 0.2 s to 4.6 s. To compensate for the 25(2) s lifetime of the condensate, we insert a variable length delay between the initialization step and application of the perturbation to keep the total time constant (Without this normalization, a 25(2) s lifetime would cause an atom loss of $\approx 20\%$ in 4.7 s, changing the chemical potential by $\approx 10\%$). At the end of the experiment, the circulation state is measured by releasing the atoms and looking at the resulting interference pattern between the ring and disc BECs [?, 35]. For each temperature, four different perturbation strengths are selected. The perturbation strengths are chosen such

that the lifetime of the persistent current state is varied over the entire range of t . The measurement is repeated 16-18 times for each combination of U_b , T and t . The average of the measured circulation states $\langle \ell \rangle$ gives the probability of the circulation state surviving for a given set of experimental parameters.

Figure 6.2(a) shows $\langle \ell \rangle$ vs. t for $T = 85(20)$ nK and four different U_b . We fit the data to an exponential $\exp(-\Gamma t)$. GP theory predicts either a fast decay (< 10 ms) or no decay, depending on the precise value of U_b/μ [41]. By contrast, we see from Fig. 6.2(a) that Γ changes smoothly from $4.1(6) \times 10^{-2} \text{ s}^{-1}$ to $6.2(8) \text{ s}^{-1}$ as U_b is changed from $0.50(4)\mu$ to $0.59(5)\mu$. Thus we are able to tune the decay rate by over two orders of magnitude by changing the magnitude of perturbation by $\approx 0.1\mu$, in qualitative agreement with TWA simulation results [41]. This confirms that the decay of a persistent current is a probabilistic process, in contrast to the instantaneous, deterministic transitions seen in GPE simulations [41].

To explore whether a longer hold time shifts or broadens the transition between persistent current states, we measured the average persistent current as a function of U_b while keeping t constant. Figure 6.2(b) shows this measurement for three different t : 0.5 s, 2.5 s and 4.5 s. We fit this data to a sigmoidal function of the form $\langle \ell \rangle = [\exp((U_b/\mu - \zeta)/\alpha) + 1]^{-1}$ to extract estimates of the width α and center ζ of the transition ¹. We see that changing the perturbation strength by $\approx 0.2\mu$ decreases $\langle \ell \rangle$ from one to zero. The width α is essentially unchanged as we change t from 0.5 s to 4.5 s, though the center of the sigmoid ζ shifts by $\approx 0.1U_b/\mu$. We also

¹the extracted center and FWHM of the transition are independent of the form of the sigmoidal function chosen

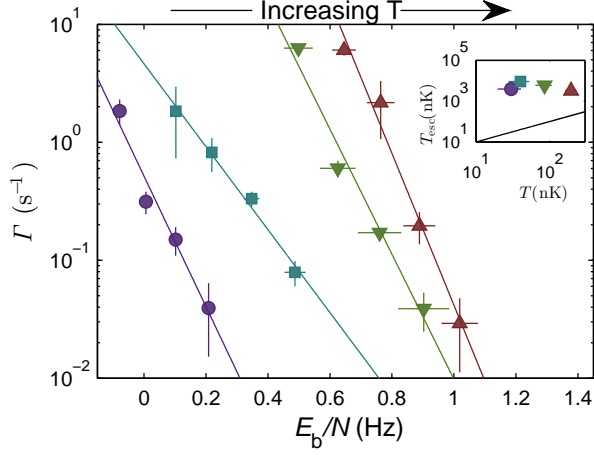


Figure 6.3: **Taken from [6].** (color online). Measured decay rate of the persistent current Γ as a function of perturbation strength U_b for four different temperatures: 30(10) nK (circles), 40(12) nK (squares), 85(20) nK (inverted circles) and 195(30) nK (triangles). The solid lines are fits of the form $\Gamma = \Omega_a \exp(E_b/k_B T_{esc})$, where E_b is the energy barrier, k_B is the Boltzmann constant, and T_{esc} and Ω_a are fit parameters. The inset shows the extracted T_{esc} as a function of measured physical temperature: 30(10) nK (triangle), 40(12) nK (square), 85(20) nK (circle) and 195(30) nK (inverted triangle). The solid line shows $T_{esc} = T$.

took similar measurements at a temperature of 85(20) nK (not shown). The width α remains essentially independent of t even at higher temperatures. For a hold time $t = 0.5$ s, we found a center $\zeta = 0.50(4)U_b/\mu$ at $T = 85(20)$ nK; by contrast, we obtain $\zeta = 0.64(4)U_b/\mu$ for a $T = 40(12)$ nK. This indicates that an increase in temperature makes a phase slip more probable even with smaller U_b .

To understand if the decay of the persistent current is thermally activated or quantum mechanical in nature, we first must understand the nature of the energy

barrier, E_b , that separates the two states. To estimate the size of E_b , we consider excitations that connect the $\ell = 1$ to the $\ell = 0$ state. In the context of a one-dimensional ring, a persistent current decay corresponds to having either thermal or quantum fluctuations reduce the local density, producing a soliton that subsequently causes a phase slip [137]. For rings with non-negligible radial extent, TWA simulations suggest that a vortex passing through the annulus of the ring (through the perturbation region) causes the transition [41]. Because of the narrow width of our ring, we expect that a solitonic-vortex is the lowest energy excitation that can connect two persistent current states [138–143]. An analytical form for the energy of a solitonic vortex is given by [139, 140]:

$$\epsilon_{sv}(U_b/\mu) \approx \pi n_{2D} \frac{\hbar^2}{m} \ln\left(\frac{R_\perp}{\xi}\right) + \frac{1}{2} m N_c \left(\frac{\hbar}{2mR}\right)^2 \quad (6.1)$$

where N_c is the total number of condensate atoms in the ring, ξ is the healing length, R_\perp is the Thomas-Fermi width of the perturbation region and n_{2D} is the maximum 2D density in the region of the perturbation. The first term is the energy of a solitonic-vortex while the second term is the kinetic energy of the remaining π phase winding around the ring. We note that N_c , R_\perp , ξ and n_{2D} all depend implicitly on T and U_b . Finally,

$$E_b(U_b, T) = \epsilon_{sv} - \epsilon_{\ell=1} = \epsilon_{sv} - \frac{1}{2} m N_c \left(\frac{\hbar}{mR}\right)^2, \quad (6.2)$$

where $\epsilon_{\ell=1}$ is the energy of the first persistent current state. We have verified the accuracy of these expressions using GP calculations similar to those in Refs. [139, 140, 144, 145] to within 10 % for our parameters.

Fig. 6.3 shows the clear temperature dependence of the measured decay rate Γ of the persistent current. To quantify this dependence, we fit the data to the form $\Gamma = \Omega_a \exp(E_b/kT_{esc})$ for each temperature (shown as the solid lines in Fig. 6.3). We note that while the attempt frequency Ω_a is dependent on temperature (changing by five orders of magnitude from 40(12) nK to 195(30) nK), T_{esc} is not (see inset of Fig. 6.3). In fact, T_{esc} is roughly constant at $\approx 3\mu K$, while the BEC temperature varies from 30(10) nK to 195(30) nK. Thus, simple thermal activation does not explain the probability of a transition, since $T_{esc} \neq T$. The constancy of T_{esc} hints that a temperature-independent phenomenon like macroscopic quantum tunneling may play a role, as it does in superconducting systems [146]. We can estimate the decay rate due to quantum tunneling by drawing an analogy with an rf-superconducting quantum interference device. In this device, the quantum tunneling rate can be estimated by the WKB approximation, $\Gamma \approx (\omega_p/2\pi) \exp(-E_b/\hbar\omega_p)$, where ω_p is the frequency of the first photon mode in the superconducting system [30]. Here, by analogy, ω_p is the frequency of the first azimuthal phonon mode, which is $\approx 2\pi \times 30$ Hz. For our system, $E_b/\hbar\omega_p > 10^3$, so the quantum tunneling should be negligible. Thus, the observed decay cannot be described by either simple thermal activation or quantum mechanical tunneling [146]. It may be that more complicated models of energy dissipation may be required.

Finally, because there are parallels between a vortex moving through the annulus of the ring and a vortex leaving a simply connected BEC, we investigated models that predict the dissipative dynamics of these vortices [133, 135]. Such models predict lifetimes that scale algebraically with E_b and T . As can be seen from

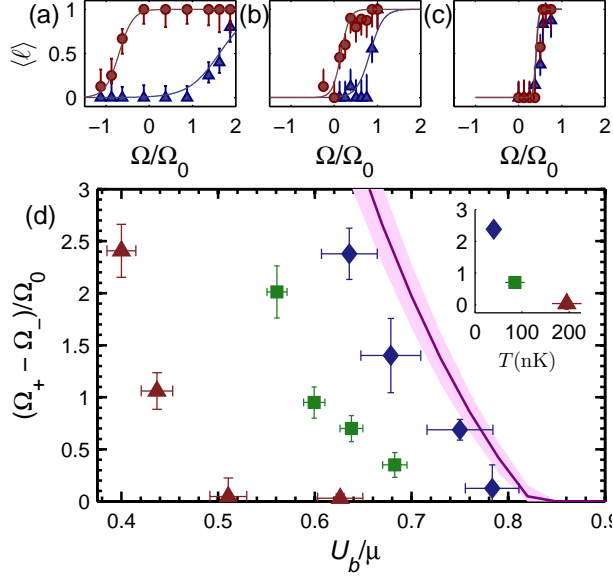


Figure 6.4: **Taken from [6].** Hysteresis loop for a perturbation strength of $0.64(4)U_b/\mu$ for 40(12) nK (a), 85(20) nK (b), and 195(30) nK (c).(d) Size of the hysteresis loop, $(\Omega_+ - \Omega_-)/\Omega_0$ (see text), vs. barrier strength for three different temperatures: 40(12) nK, diamonds, 85(12) nK (squares), and 195(12) nK (triangles). The zero temperature, GPE predicted, area of the hysteresis loop is shown as a purple band, which incorporates the uncertainty in speed of sound. The left y axis of the inset shows the hysteresis loop size shown in (a)-(c) as a function of temperature for a perturbation strength of $0.64(4)U_b/\mu$. The right y axis of the inset shows the corresponding extracted critical velocity (mm/s).

Fig. 6.3 our data scales exponentially with E_b . Thus, these models fail to explain the experimental data.

The measurements of the decay constants described above shows the strong effect of temperature on the persistent current state. As discussed above, this temperature dependence is wholly captured in the variation of the constant Ω_a with T , as T_{esc} is constant. This causes an apparent change in the critical velocity of a moving barrier (for a given application time), with higher temperatures having lower critical velocities. Such a change in critical velocity affects hysteresis loops [35]. For initial circulation state $\ell = 0(1)$, we experimentally determine $\Omega_+(\Omega_-)$, the angular velocity of the perturbation at which $\langle \ell \rangle = 0.5$. The hysteresis loop size is given by $\Omega_+ - \Omega_-$, normalized to Ω_0 , where $\Omega_0 = \hbar/mR^2$, m is the mass of an atom, R is the mean radius of the torus. We measure the hysteresis loop for four perturbation strengths and three different temperatures: 40(10) nK, 85(20) nK and 195(30) nK as shown in Fig. 6.4, with the zero-temperature GP prediction based on the speed of sound shown for references [35, 147]. We see from Fig. 6.4 that the discrepancy between experimental data and theoretical predictions decreases as the temperature is lowered. Using the density distribution of atoms around the ring, we extract the critical velocity from the hysteresis loop size [35]. For example, at $U_b/\mu = 0.64(4)$, a temperature change of 40(12) nK to 195(30) nK corresponds to a change in the critical velocity of $0.26(6) c_s$ to $0.03(2) c_s$. Here, c_s is the speed of sound in the bulk. While the measured critical velocity approached the zero-temperature, speed of sound, we see that at non-zero temperature thermal fluctuations must be taken into account in any measurement or calculation of the critical velocity.

In conclusion, we have measured the effect of temperature on transitions between persistent current states in a ring condensate in the presence of a local perturbation. The results of this work indicate that as thermal fluctuations become more pronounced, it becomes easier for the superfluid to overcome the energy barrier and the persistent current state to decay. If we assume that the decay is thermally driven and is thus described by an Arrhenius-type equation, we find a significant discrepancy between the measured temperature and the effective temperature governing the decay. Other possible mechanisms like macroscopic quantum tunneling should be greatly suppressed. Despite the disagreement, we find a clear temperature dependence of the critical velocity of the superfluid by measuring hysteresis loops. This work will provide a benchmark for finite temperature calculations on the decay of topological excitation in toroidal superfluids.

This supplemental material contains three sections. The first section explains the experimental procedure for initializing the persistent current state and the subsequent measurement. The second section explains the procedure for extracting temperature. The third section presents the method we use to calibrate perturbation strength and the effect of finite temperature on the calibration of the perturbation strength.

6.2 Experimental procedure

After creating a BEC in the target shaped trap, the experiment involves two stages, first a preparation stage followed by a measurement stage [see Fig. 6.5]. In

the preparation stage, a stationary perturbation is adiabatically raised in the ring for a total time, $T_{sp} = 1$ s to destroy any spontaneous circulation states. Subsequently, a circulation state is imprinted on the atoms by moving the perturbation around the ring for a total time, $T_{int} = 1$ s. In the preparation stage, both perturbations have a strength of $\approx 1.1\mu$, where μ is the unperturbed chemical potential. The density perturbation is raised to this strength in 300 ms, kept constant for 400 ms and then lowered down to zero in 300 ms. The reliability of the experimental data depends both on our ability to imprint circulation states deterministically and to eliminate spontaneous circulation states. The confidence level of having no spontaneous circulation before imprinting the circulation state is 0.99(1). The confidence level of imprinting a circulation state with one unit of circulation before the measurement stage is 0.96(2).

To measure the decay constant, we again apply a stationary perturbation whose strength is variable, but always less than the chemical potential. The perturbation is applied for a variable time t , during which it is raised to a desired strength in 70 ms, kept constant and then lowered down in 70 ms.

To measure the hysteresis loop size, we initialize the atoms in the ring in either a circulation state of $\ell = 0$ or $\ell = 1$. A rotating perturbation with a strength less than the chemical potential μ is then applied with a variable rotation rate to trace out the hysteresis loop [35]. The rotating perturbation is on for a total of 2 s, during which it is raised to the desired strength in 300 ms, kept constant, and then lowered in 300 ms.

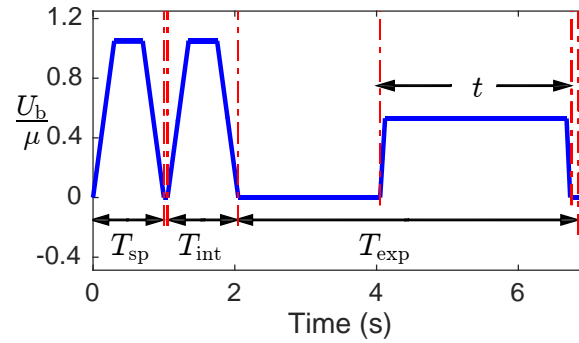


Figure 6.5: **Taken from [6].** The experimental sequence for measuring current decay. A stationary perturbation with height $U_b/\mu \approx 1.1$, where μ is the chemical potential is turned on during T_{sp} to destroy any spontaneous circulation. A rotating perturbation with the same height imprints the $\ell = 1$ circulation state during T_{int} . A stationary perturbation with strength less than the chemical potential (shown here as $0.5U_b/\mu$) probes the circulation state for t . An intermediate step $T_{exp} - t$ is introduced to ensure that the total experimental time T_{exp} remains constant.

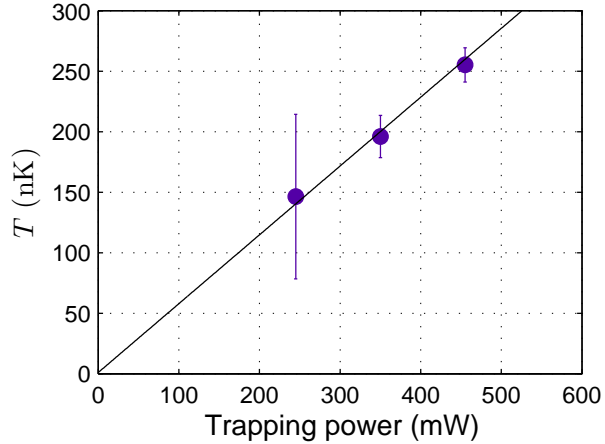


Figure 6.6: **Taken from [6]**. Measured temperature vs. power in the red-detuned (1064 nm) vertical trapping beam. The errorbars show the statistical uncertainty.

6.3 Measuring the temperature

The persistent current lifetime was measured at four different temperatures. The higher temperatures of 85(20) nK and 195(30) nK are achieved using the red-detuned vertical trap while the lower temperatures of 30(10) nK and 40(12) nK are obtained using the blue-detuned vertical trap. Typically, the temperature of the BEC is extracted by releasing the atoms from the trap and measuring the density distribution in time of flight (ToF). The 1D integrated density is then fitted to a bimodal distribution: the sum of a Gaussian and a Thomas-Fermi profile. The Gaussian part describes the thermal part while the Thomas-Fermi profile describes the condensate part. Fitting the evolution of the width of the Gaussian as a function of time yields the temperature [148].

To understand the final temperature, we need to understand the evaporation profile and the final trap configuration. During the evaporative cooling stage, the

laser cooled atoms are transferred to a red-detuned optical dipole trap with a depth of the order of $10 \mu\text{K}$. We then do an exponential forced evaporation ramp by lowering the laser power to obtain a degenerate quantum gas. The temperature of this gas is set by the final depth of the optical dipole trap. We reach a temperature of $85(20) \text{ nK}$ and $195(30) \text{ nK}$ for powers of 140 mW and 350 mW of red-detuned IR light respectively. A separate TEM_{00} red-detuned crossed dipole trap is then turned on ², after which the condensate is transferred to the target trap. The atoms now reside in a potential which is the convolution of an attractive potential of the red-detuned sheet trap and a repulsive blue-detuned target trap. The trap depth and hence the temperature is set by the red-detuned trap, since the potential due to red-detuned TEM_{00} beams are typically deeper than their blue-detuned counterparts [149]. To extract the temperature, we release the atoms in the target trap in time of flight and then image the cloud in the horizontal direction. We extract a temperature by fitting the atom density to a bimodal distribution. This measurement was repeated at various optical powers. The temperature of $195(30) \text{ nK}$ at 350 mW of trap power can be measured directly. The temperature of $85(20) \text{ nK}$ at 140 mW is obtained by extrapolation of the fit shown in Fig. 6.6. This extrapolation is necessary as the bimodal fit becomes less reliable at lower temperature, as the thermal fraction decreases.

²The transverse dimensions of atoms in the red-detuned vertical trapping beam is on the order of $100 \mu\text{m}$, while the target trap is only $\approx 50 \mu\text{m}$ in diameter. To ensure efficient transfer to the target trap, a Gaussian beam of $1/e^2$ width of $\approx 50 \mu\text{m}$ is turned on in tandem with the vertical confinement beams (effective mode matching)

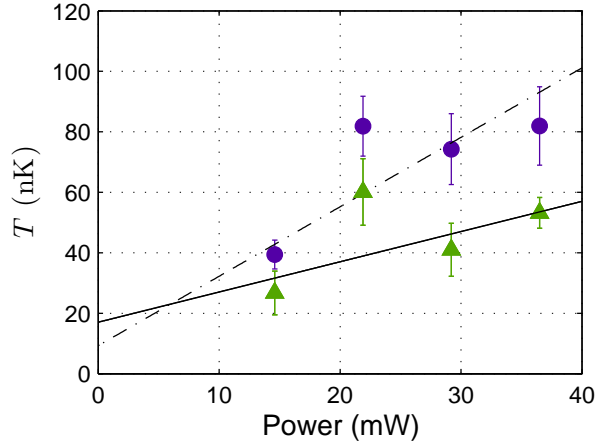


Figure 6.7: **Taken from [6].** Measured temperature vs mask beam power. Measurements are for a vertical trapping frequency of 520 Hz (circles) and 970 Hz (triangles) as a function of power in the radial trapping beam incident on the DMD. The experiment was carried out with the lowest radial trapping power of 14.6 mW.

A modified procedure is used when the blue detuned vertical trap is used. The blue-detuned vertical trap is a TEM_{01} beam. Atoms initially reside in the combination of red-detuned vertical trap and the crossed dipole trap. The atoms are then adiabatically transferred from the red-detuned vertical trap to the blue-detuned vertical trap (while horizontal confinement is maintained by the crossed dipole trap). We then perform a forced evaporation ramp by lowering the trapping power of the crossed dipole trap. Finally, the atoms are transferred to the target potential and the crossed dipole beam is turned off. We let the condensate equilibrate for 1 s. The temperature in the blue-detuned trap is set by both the depth of the target trap potential and the power of the blue-detuned vertical trap. The method used to extract temperature from the red-detuned trap does not work with the blue-detuned

trap due to the lower temperature. To circumvent this problem, we blow away the atoms in the ring and let the atoms in the disc expand in time of flight, imaging vertically. This is done for two primary reasons. First, the central disc is hard-walled and we expect the atoms in the disc to have a lower critical temperature³. A lower critical temperature results in a higher fraction of thermal atoms, making it easier to extract a temperature. Second, an analytical expression for an expanding toroidal trap does not exist⁴. To make our measurements more accurate, we not only took data in the experimental configuration (with a target trap power of 14.6 mW), but also at higher powers using the same atom number and vertical trapping frequency of the blue-detuned trap. A fit of the temperatures measured at higher power can be linearly extrapolated to verify the measured temperature at the experimental configuration. The measured temperatures for the blue-detuned trap are shown in Fig. 6.7. We reach a temperature of 40(12) nK and 30(10) nK for vertical trap frequencies of 520 Hz and 970 Hz respectively.

6.4 The effect of temperature on perturbation strength calibration

Calibration of the perturbation strength is done *in-situ* and follows the same procedure as [35]. Briefly, the optical density of atoms at the position of the perturbation is measured as a function of perturbation strength. Due to optical aberrations in the imaging system, the behavior of the optical density vs. U_b changes

³A simple assumption of uniform density for the hard walled disc puts the critical temperature to be on the order of 100 nK below the critical temperature of atoms in the ring

⁴we assume that the temperature of atoms in the disc and the ring are equal

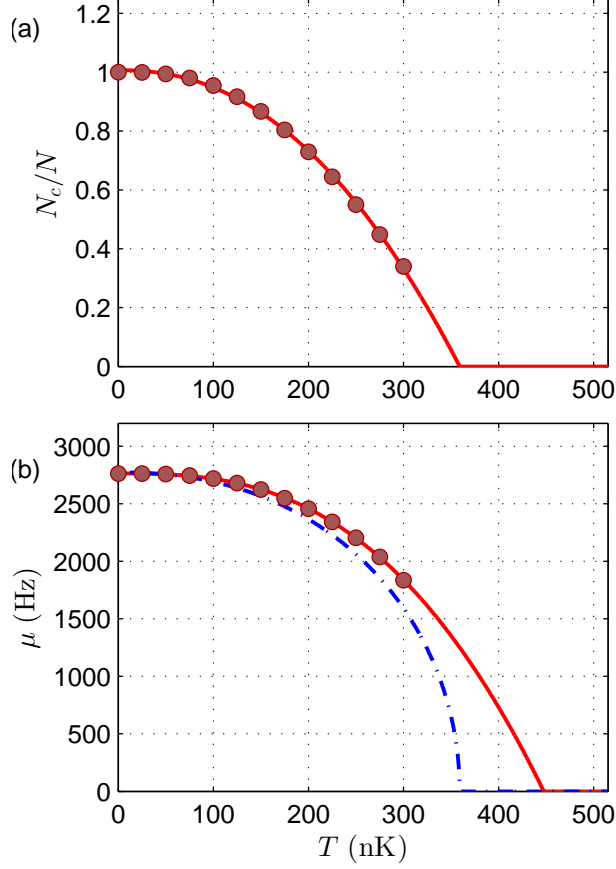


Figure 6.8: **Taken from [6].** (a) Computed condensate fraction as a function of temperature. The points show the results of our ZNG calculations for a vertical trapping frequency of 512 Hz (see text). A fit of the form $N_c/N = 1 - (T/T_c)^\alpha$ with $\alpha = 2.22(9)$ is also shown. (b) Computed chemical potential as a function of temperature. The red line shows a fit of the form $\mu(T)/\mu(T = 0) = 1 - (T/T_c)^\beta$ with $\beta = 2.72(4)$. For reference, the dash-dot line shows $\mu(T)/\mu(T = 0) = [1 - (T/T_c)^\alpha]^{1/2}$, expected from the Thomas-Fermi approximation. The difference between these two curves yields the first order correction to the barrier calibration as a function of temperature.

between $U_b/\mu < 1$ and $U_b/\mu > 1$. In particular, this function exhibits an “elbow” at $U_b/\mu = 1$. The location of the elbow where the optical density levels out enables us to determine the chemical potential of the un-perturbed toroid.

During imaging, we are unable to distinguish thermal atoms from the condensate atoms. It is possible that as we change the temperature, the resulting change in the thermal fraction may impact the measurement of the perturbation strength. Here, we investigate the systematic error introduced due to the barrier calibrations done at different temperatures. We performed ZNG [127] calculations to determine the effect of finite temperature on our measurements. In the ZNG model, the effective potential experienced by the condensate is:

$$U_c = V_{3d} + 2gn_{3dt}. \quad (6.3)$$

Here V_{3d} is the toroidal potential, n_{3dt} is the number density of the thermal cloud, $g = 4\pi\hbar^2 a_s/m$ is the interaction strength coefficient and a_s is the s-wave scattering length. This enables us to calculate the total number of atoms in the condensate N_c and the density of condensate atoms n_{3dc} by using the Thomas-Fermi approximation. The effective potential felt by the thermal atoms is given by:

$$U_t = V_{3d} + 2gn_{3dt} + 2gn_{3dc}. \quad (6.4)$$

This potential U_t is used to determine the thermal atom distribution n_{3dt} ,

$$n_{3dt} = 1/\Lambda_{dB}^3 Li_{3/2}(\exp((\mu - U_t)/k_B T)). \quad (6.5)$$

which can be summed up to yield the total number of thermal atoms N_t . Here $Li_{3/2}$ is the polylogarithmic function of order 3/2. These equations are solved under the

constraint that the total atom number N_0 is the sum of condensate atom number N_c and thermal atom number N_t , and remains constant. For a given temperature, this procedure of calculating the number of thermal atoms N_t and condensate atoms N_c is carried iteratively until the solution converges. The lowest temperature where the condensate atom number drops to zero is the critical temperature T_c .

Figure 6.8(a) shows the calculated condensate fraction as a function of temperature for a vertical trapping frequency ω_z of 518(4) Hz and radial trapping frequency of 258(12) Hz. The solid line shows a fit of the form $N_c/N = 1 - (T/T_c)^\alpha$ with $\alpha = 2.22(9)$. The extrapolated fit yields a critical temperature of 370 nK. Figure 6.8(b) shows the calculated chemical potential as a function of temperature. A fit of the form $\mu(T)/\mu(T = 0) = 1 - (T/T_c)^\beta$ with $\beta = 2.72(4)$ is shown as a solid line. For reference, the dash-dot line shows the expected Thomas-Fermi chemical potential $\mu(T)/\mu(T = 0) = [1 - (T/T_c)^\alpha]^{1/2}$. (For a ring, $N \propto \mu^2$ in the Thomas-Fermi approximation.) The shift between these two curves arises from the additional mean-field interaction between the thermal gas and the condensate. For a vertical trapping frequency of 512 Hz, the highest temperature that we operate at is 85(20) nK, which should be compared to the critical temperature of 370 nK (see Fig. 6.8). The fractional change in chemical potential due to the thermal component is 3.5×10^{-2} . This leads to a 3 % systematic shift in the barrier calibration. At the higher temperature of 195(30) nK with $\omega_z = 985$ Hz and $\omega_r = 258(12)$ Hz, the systematic shift is around 8 % (owing to the higher transition temperature of 470 nK), but this is small compared to the statistical error.

6.5 Table of Experimental parameters and fit

Case	T (nK)	T_c (nK)	$\omega_z/2\pi$ (Hz)	$N/10^5$	μ/h (kHz)	T_{esc} (nK)	Ω_a (s $^{-1}$)
I	30(10)	470(30)	974(7)	4.46(26)	2.91(12)	$3.9(6)\times 10^3$	$5(2)\times 10^{-1}$
II	40(12)	370(40)	518(4)	6.71(39)	2.93(11)	$9.2(8)\times 10^3$	$4.8(9)\times 10^0$
III	85(20)	370(40)	520(10)	6.48(46)	2.68(11)	$5.9(8)\times 10^3$	$1.9(4)\times 10^3$
IV	195(30)	470(30)	985(4)	4.22(26)	2.66(08)	$3.2(4)\times 10^3$	$1.2(2)\times 10^5$

Table 6.1: The temperature (T), critical temperature T_c , vertical trapping frequency ω_z , number of atoms N , chemical potential (μ) and fit parameters escape temperature T_{esc} and a for different trapping configurations. The radial trapping frequency ω_r remains essentially constant across all the configurations at 258(12) Hz. Errorbars in N and μ exclude systematic effects which we estimate to be up to a 20% common shift.

Chapter 7: A rapidly expanding Bose-Einstein condensate: an expanding universe in the lab

In this chapter, we study the dynamics of a toroidal Bose-Einstein condensate when the mean radius of the toroidal confinement is changed supersonically. We deploy both experimental and numerical methods for this study. We focus on the similarities between a rapidly expanding toroidal condensate and cosmological expansion. We observe red-shifting of long-wavelength excitations (phonons in case of a BEC). We observe that the energy deposited in the condensate during the radial expansion is dissipated by creation of topological excitations like solitons and vortices. The decay of these excitations leads to production of azimuthal phonons, and stochastic persistent currents. The content of this chapter is based on the following work [44].

1) “A supersonically expanding Bose-Einstein condensate: an expanding universe in the lab”, S. Eckel, A. Kumar, T. Jacobson, I.B. Spielman, G.K. Campbell, *arXiv:1710.05800* (2017).

This work has been reproduced in appendix B. I contributed to the experimental data acquisition.

Chapter 8: Conclusions and Future Experiments

In this thesis, we have shown the versatility of a ring-shaped ultracold superfluid as an experimental test bed. The experimental data obtained during the course of this thesis has made possible several insights into the behavior of an ultracold superfluid gas. The main outcomes of this thesis are:

- 1) Development of new metrological tools for measuring the circulation state of a ring-shaped superfluid. The circulation state in time of flight is measured interferometrically in time of flight, and using the Doppler effect in-situ.
- 2) Measuring the current phase relationship of a superfluid weak link.
- 3) Measuring the excitation spectrum of a ring-shaped superfluid.
- 4) We showed the explicit dependence of the critical velocity of a superfluid on the temperature. By varying the temperature of the superfluid, we showed both agreement and disagreement with predictions of the GP equations at zero temperature.
- 5) We showed that ultracold atoms can be used to mimic some aspects of cosmological expansion like red-shifting and the creation of spontaneous topological defects.

Despite the work done in this thesis, some aspects of the physics remain unexplored or unanswered. In the last two years, considerable work has been done on

the construction of a new generation of sodium rings experiment. Important improvements has been incorporated to improve the resolution of the imaging system by a factor of over four. With the improved resolution, we will be in a position to address interesting questions. For example, we can make make weak links at much smaller length scales, which will enable us to study the effects of tunneling effects in a superfluid ring. A better resolution will also help in a tighter radial confinement. It would be very interesting to repeat the expanding rings experiments with a tighter confinement. We saw that the radial oscillations of the condensate around its final mean position created topological defects. It would be interesting to observe the number of topological defects as a function of the radial trapping frequency. The structure factor measurements could also be repeated again, given that we have a better detection threshold. That will make comparison to theory over a broader range of data possible. We could also use the DMDs to excite both radial and azimuthal modes simultaneously, which will give rise to the excitation spectrum of a heavy phonon, which exhibits the dispersion relation of a massive relativistic particle.

Appendix A: Electronics development

A.1 Vacuum interlock operation

The operation of the interlock is as follows: the decision whether the vacuum state of the experiment lies above or below the safety threshold is decided by a signal from a vacuum gauge controller, Agilent XGS-600. The output from the XGS is connected to a 5 V signal using a 300 Ohm resistor. When the vacuum state is acceptable, the output from the controller is 0. A vacuum pressure reading above the safety threshold will give a output of 1. The safety threshold can be programmed in a Agilent XGS-600, which we set to be 1×10^{-10} torr for the main chamber and 5×10^{-7} torr for the oven side. As a zero signal is more susceptible to noise, we pass the signal through a NOT gate, so a logical high corresponds to an acceptable vacuum state. We use a flip-flop as a memory element for storing the vacuum state.

The interlock is always in a dis-engaged state when it is first powered on, so the output of the flip flop is zero initially. This desired output is implemented by sending a digital low signal to the ‘clear’ port of the D flip-flop [150], when the vacuum interlock first powers up. This is done by using a 22 μ F capacitor (shown as C3 in figure 2.2). This capacitor is connected to the ‘clear’ port of the D flip-flop on one side and ground on the other side. The ‘clear’ port is connected a +5 V

supply using a 2 k Ω resistor. When the interlock is first powered up, the +5 V supply can discharge to ground using the 22 μ F capacitor. As long as the capacitor is charging, the ‘clear’ remains at zero level, and raises to a logical level one when the capacitor is fully charged. This means that the output of the flip flop $Q = 0$ (shown as port 5 of the block 7474N in figure 2.2). This the output of the AND gate shown as V3/1 is also 0, and the gate valve will remain closed. Since the flip-flop is a memory element, the flip-flop will remain in that state. This implies that in the case of a power outage, the gate valve will be off when the power comes back, The gate valve will only open when the clock state is reset, which can only be done with human intervention. The RC constant of the circuit connected to the ‘clear’ port is $\tau = 66$ ms. This implies that after a time of around 5τ , the capacitor is fully charged and the ‘clear’ port of the flip flop is at logical high state.

If the vacuum system is good and below the safety threshold, and the ‘clear’ port is at logical high state, we turn the global activate switch on. This means that the data input to the flip flop is 1, since it is a result of an AND operation between the global activate and the NOT of the pressure gauge controller. The clock signal will see a downward slope. The output of the flip-flop will still be zero, since the flip-flop needs a positive edge trigger to make a change in the transition. Now we hit the clock button. This switch is a press button, which is on only when it is pressed. When the button is first pressed, the flip flop sees a positive clock pulse, which enables it to change its output state. This means that the output Q changes from 0 to 1, so the output U also changes to 1. The output U is obtained after an AND operation with the output of the flip flop and AND operation with the global

enable and the vacuum controller, as an additional precaution should the go into an indeterminate state. The output U controls a solid state relay, which controls an external power supply providing power to the gate valve, which opens up.

In the case the pressure in the main chamber exceeds the safety threshold and goes above the safety limits, the input from the vacuum gauge controller will go to logical high, which means that the value of the data point to the flip flop is now a logical low. While this happens, the clock of the flip flop sees a positive transition, since the clock is derived from an OR gate between the clock switch and the data signal. This means that the output of the flip-flop will go to zero, shutting off the gate valve. If the pressure comes back to safety values, the data signal will again become 1, but the clock signal will see a downward slope and hence no change in the output will happen. Only when a person comes up, and presses the clock button does the flip flop clock get a positive slope signal and the gate valve will open again.

A.2 Evaporation sequence

This section lists the various steps of evaporative cooling needed to make a condensate. The steps have been listed in a table [A.1](#) , and the waveform has been shown in figure [A.1](#). The current in the quadrupole magnetic coils is given in amperes (A), producing a field of 1.2 G/(A-cm). The power in the red-detuned sheet is given in mW. The power going to the TOP trap coils is controlled with an analog signal, where the maximum and the minimum power is obtained with 5 V and 0 V respectively. The frequency of RF radiations used for radiation is given in MHz.

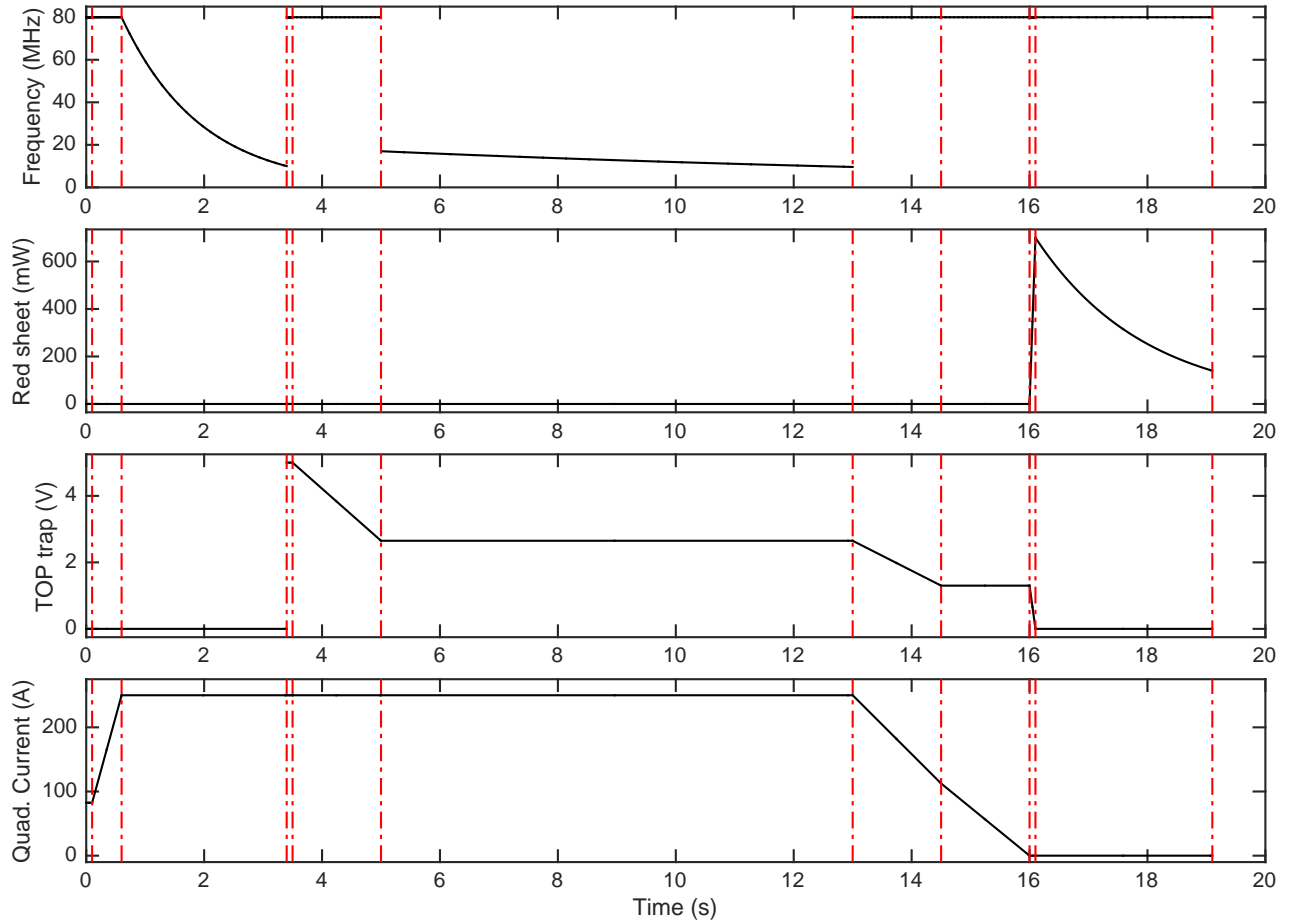


Figure A.1: The figure above shows the waveforms during a typical evaporation sequence to produce a BEC in a red-detuned sheet. The first panel shows the current flowing in the quadrupole coils producing a field of $1.2 \text{ G}/(\text{A}\cdot\text{cm})$. The second panel shows the voltage of the analog switch controlling the power to the amplifier for the TOP trap coils. The third panel shows the power in the red-detuned sheet. The last panel shows the frequency of the RF field responsible for evaporative cooling in MHz. The red-lines separate marks the end of a step in the sequence, which have been detailed in the table [A.1](#) .

In the table, LR and ER denote linear ramp and exponential ramp respectively.

Step no.	Step description	Time	Quad. current	TOP trap	Red-sheet power	RF freq.
1	Quadrupole on	0.1 s	82.5 A	0 V	0 mW	80 MHz
2	Compress Quadrupole	0.5 s	LR(82.5,250) A	0 V	0 mW	80 MHz
3	Quadrupole RF evap.	2.8 s	250 A	0 V	0 mW	ER(80,10) MHz
4	TOP trap on	0.1 s	250 A	5 V	0 mW	80 MHz
5	Death Circle Evap.	1.5 s	250 A	LR(5,2.65) V	0 mW	80 MHz
6	TOP trap Evap.	8 s	250 A	2.65 V	0 mW	ER(80,10) MHz
7	relax TOP trap	1.5 s	LR(250,112.5) A	LR(2.65,1.3) V	0 mW	80 MHz
8	Transfer to red-sheet	0.5 s	LR(112.5,0) A	1.3 V	0 mW	80 MHz
9	Set bias	0.02 s	0 A	LR(1.3,0) V	LR(0,700) mW	80 MHz
10	Red-sheet evap.	3 s	0 A	0 V	ER(700,140) mW	80 MHz

Table A.1: caption.

Appendix B: A rapidly expanding Bose-Einstein condensate: an expanding universe in the lab

This appendix is a copy of the following work [44].

1) “A supersonically expanding Bose-Einstein condensate: an expanding universe in the lab”, S. Eckel, A. Kumar, T. Jacobson, I.B. Spielman, G.K. Campbell, arXiv:1710.05800 (2017).

A rapidly expanding Bose-Einstein condensate: an expanding universe in the lab

S. Eckel,¹ A. Kumar,¹ T. Jacobson,² I.B. Spielman,¹ and G.K. Campbell¹

¹*Joint Quantum Institute, National Institute of Standards and Technology and University of Maryland, Gaithersburg, Maryland 20899, USA*

²*Department of Physics, University of Maryland, College Park, Maryland 20742, USA*

We study the dynamics of a supersonically expanding ring-shaped Bose-Einstein condensate both experimentally and theoretically. The expansion redshifts long-wavelength excitations, as in an expanding universe. After expansion, energy in the radial mode leads to the production of bulk topological excitations – solitons and vortices – driving the production of a large number of azimuthal phonons and, at late times, causing stochastic persistent currents. These complex nonlinear dynamics, fueled by the energy stored coherently in one mode, are reminiscent of a type of “preheating” that may have taken place at the end of inflation.

Cosmological expansion is central to our understanding of the universe. Here, we experimentally create a system where fields expand in a similar way as in the universe: an expanding, ring-shaped atomic Bose-Einstein condensate (BEC). Our laboratory test bed demonstrates three effects associated with the expanding universe. First, we conclusively demonstrate a redshifting of phonons analogous to the redshifting of photons, which provided the first evidence for an expanding universe [1]. Second, we observe hints of “Hubble friction” that damps the redshifted fields [2]. Third, we observe a process in which energy is rapidly transferred from a homogeneous radial mode into azimuthal modes by a nonlinear, turbulent cascade, reminiscent of that seen in some models of preheating at the end of cosmological inflation [3–9]. Experiments such as these can thus emulate both linear and nonlinear field theoretic aspects of cosmology.

A zero-temperature BEC is a vacuum for phonons [10], just as an empty universe is a vacuum for quantum fields, like photons. In this analogy, the speed of light is replaced by the speed of sound, c , in the BEC. Evoking general relativity, the equation for long-wavelength phonons (in the hydrodynamic limit [11]) takes on a covariant form with a curved spacetime metric [12–14]. Previous studies with ultra-cold atoms illuminated different aspects of this phonon metric. For example, an interface between regions of sub-sonic and super-sonic fluid flow forms a “sonic event horizon” that exhibits effects

such as Hawking radiation [12, 14–22]. By changing the interaction strength or density, one can simulate cosmological phenomena such as pair production [23–29], Sakharov oscillations [30], or the dynamical Casimir effect [31], the latter two having been recently observed experimentally [32, 33]. Beyond cold atoms, experimental studies have realized analog event horizons in other settings, for example in optical systems [34–36] and in classical fluids [37–39]. (For a recent review, see Ref. [40].)

The expansion of our BEC-universe is forced by dynamically increasing the radius of our nearly-flat bottomed ring-shaped potential (see Appendix A) [41, 42]. Figure 1 shows our BEC during a $t_{\text{exp}} = 23.1$ ms inflation. The radial velocity of the trapping potential (defined as the rate of change of the mean radius, R) is directly controlled, and can be made comparable to the speed of sound. For the expansion shown in Fig. 1, the maximum velocity is $v_p = dR/dt \approx 1.3c$, implying that points separated by an angle $\gtrsim \pi/4$ recede faster than c . The condensates used in this work are well-described by mean field theory; thus, we compare our measurements to numerical simulations using the stochastic-projected Gross-Pitaevskii equation (SPGPE, see Appendix B), which accurately captures BEC dynamics with thermal fluctuations [43, 44]. Images from this simulation are in excellent agreement with the corresponding experimental images.

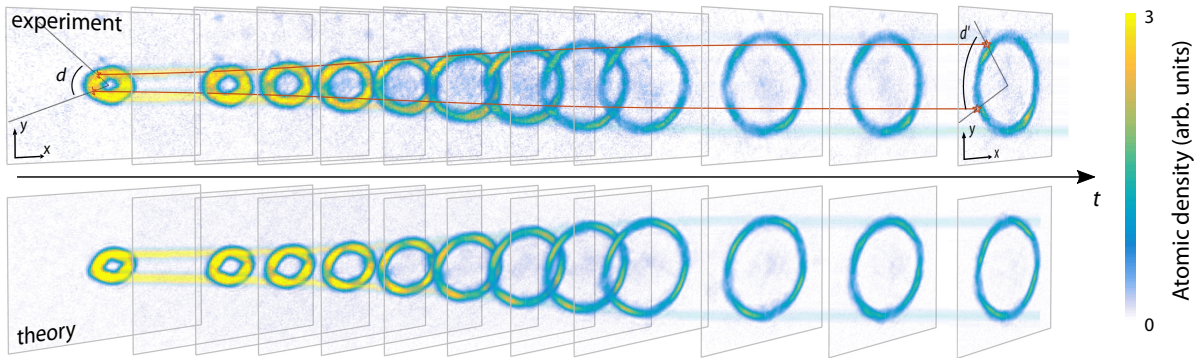


FIG. 1. Measured (top) and simulated (bottom) supersonic expansion of the ring with scale factor $a = R_f/R_i = 4.1(3)$, where $R_f = 46.4(1.4) \mu\text{m}$ ($R_i = 11.3(4) \mu\text{m}$) is the final (initial) radius [45]. An initial distance d transforms into a larger distance d' . The time elapsed in the figure is approximately 15 ms.

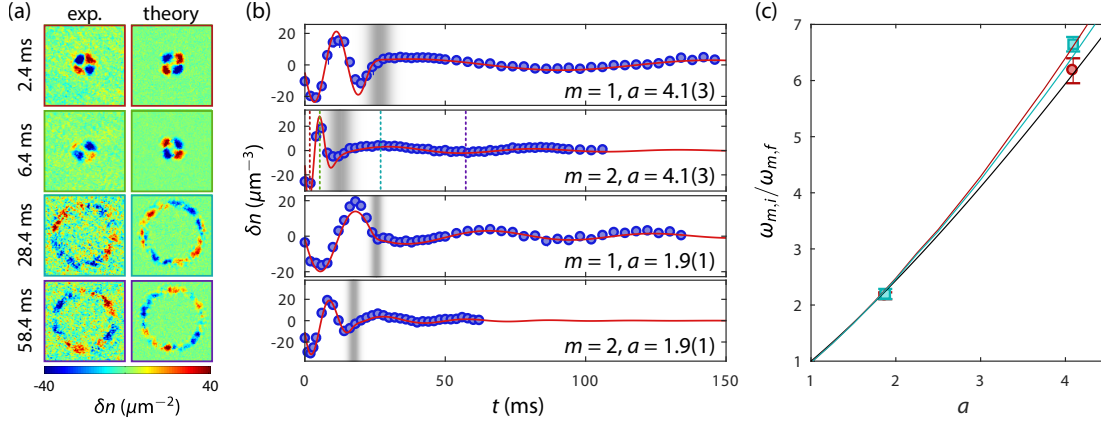


FIG. 2. Redshift of long-wave excitations. (a) Atomic density difference δn at various times for both experiment and simulation for a mode number $m = 2$ and scale factor $a = 4.1$. Density scale of images after expansion are multiplied by 10. (b) Phonon amplitude vs. time for various a and m . The grey bands indicate the time during which the BEC is inflated; their intensity denotes the expansion velocity relative to that expansion’s maximum. Vertical dashed lines in the $m = 2, a = 4.1$ panel indicate the times shown in (a). (c) Ratio of initial to final frequency vs. scale factor a . Red circles indicate $m = 1$ modes; cyan squares, $m = 2$. Solid, black curve is the $a^{9/7}$ expectation, and colored curves (with mode numbers matching points) are the result of full Bogoliubov calculation.

56 *Phonon redshift* – To study the red shifting of phonons, we first imprint a standing wave phonon excitation on the background BEC. During expansion, these effectively one-dimensional azimuthal phonons are redshifted, i.e., their wavelength grows as shown in Fig. 2a for both experiment and theory. These images show the oscillation of a standing-wave phonon, constructed by perturbing the condensate with a potential of the form $\sin(m\theta)$, where m is the integer azimuthal mode number of the phonon. The (approximate) axisymmetry implies that m is conserved, in analogy with conservation of the comoving wavevector in cosmology. The phonon wavelength is therefore stretched by a factor $a = R_f/R_i$, the ratio of the geometrical radii of the expanding ring. This is related to the usual redshift parameter z through $a = z + 1$.

70 Figure 2b shows the measured phonon amplitude δn vs. time for various a and m and clearly shows a shift in the frequency. (In this paper, we measure frequency and time in the laboratory frame, as opposed to using the comoving proper time as defined by the effective metric, Eq. C7.) To measure the frequency shift, we fit the oscillation before and after expansion to extract $\omega_{m,i}/\omega_{m,f}$, shown in Fig. 2c. At any given time, the phonon oscillation frequency is $\omega(t) = c_\theta(t)m/R(t)$, where $c_\theta(t)$ is the azimuthal speed of sound at time t . As the ring expands, both the atomic density and c_θ decrease. For the combination of harmonic confinement in the vertical direction and roughly quartic confinement in the radial direction, we find $c_\theta \propto R^{-2/7}$. The solid, black curve shows the resulting $\omega_{m,i}/\omega_{m,f} = a^{9/7}$ scaling; a full Bogoliubov calculation, with the azimuthally averaged potential, is shown as the solid, colored curves.

86 We understand the phonon’s behavior during the expansion

epoch in terms of a 1D equation for the phonon amplitude χ_m ,

$$\frac{\partial^2 \chi_m}{\partial t^2} + \left[2\gamma_m(t) + \frac{\dot{R}}{R} \right] \frac{\partial \chi_m}{\partial t} + [\omega(t)]^2 \chi_m = 0, \quad (1)$$

88 where $\delta n = (\hbar/U_0)\partial\chi_m/\partial t$, $U_0 = 4\pi\hbar^2 a_s/M$, a_s is the s -wave scattering length, and M is the mass of an atom. (See Appendix C for the derivation.) There are two contributions to the damping of the amplitude. The first damping term, γ_m , is phenomenological, but independently measured [46]. The second, \dot{R}/R , is analogous to the “Hubble friction” in cosmology, which damps fields with frequencies $\omega \lesssim \dot{a}/a$. In the present case, the Hubble friction has the largest impact when for supersonic expansion, i.e., when $\omega \lesssim \dot{R}/R$ or $mc_\theta \lesssim \dot{R}$.

97 For our expansions, we expect that the Hubble friction will play a role, particularly for the $a = 4.1, m = 1$ expansion where $\dot{R}/R \gtrsim 1.5\omega$. At maximum velocity, $\dot{R}/R \approx 3\gamma_m$ for $m = 2$ and $\dot{R}/R \gtrsim 20\gamma_m$ for $m = 1$, but this occurs only during the short expansion epoch. The Hubble friction term changes the phase and amplitude of the phonon oscillation after expansion. However, because the observed density difference δn is proportional to $\partial\chi_m/\partial t$ (see Appendix C), the predominant difference in observed amplitude before and after expansion results from the change in ω . To search for the Hubble friction term, we fit all the data simultaneously to Eq. 1, taking $\dot{R}/R \rightarrow \gamma_H \dot{R}/R$, where γ_H is a tunable parameter. While the best-fit value $\gamma_H = 0.55(21)$ indicates the presence of Hubble friction, the deviation from unity suggests that other effects like azimuthal asymmetry and non-zero annular thickness also affect the phonon amplitude [45]. For GPE simulations of the expansion of an azimuthally symmetric, thin annulus ring with a potential of a similar functional form, Eq. 1 is an accurate description of the phonon evolution (see Appendix C).

86 *Radial dynamics* – The preceding 1D discussion (based on

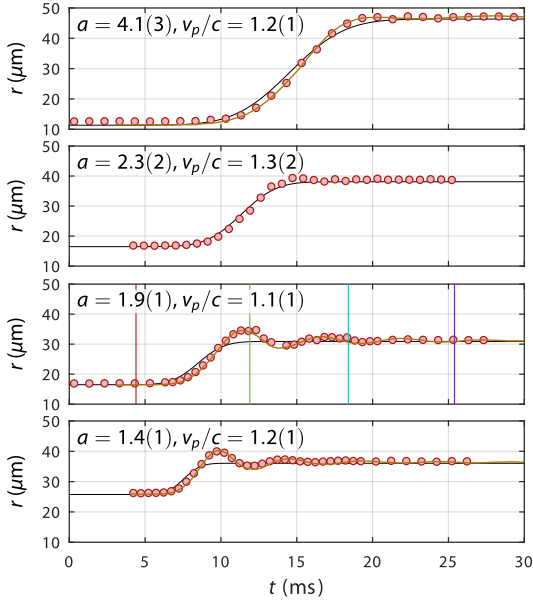


FIG. 3. Mean radius of the ring vs. time for select expansions. Black solid curves show the radius of the potential, red circles show experimental data and orange curves show simulation results. The vertical lines for $a = 1.9(1)$ correspond to times shown in Fig. 4.

Eq. 1), rested on the assumption that the background BEC contained no transverse dynamics. Perhaps the first indication of additional dynamics is visible in evolution of the ring-BEC's radius, shown by the red symbols in Fig. 3. As indicated by the oscillations around the trap's mean radius (black curves), the BEC is excited after the potential has reached its final value. The amplitude of the oscillation can be estimated based on a simple harmonic oscillator model (orange curves), where the oscillator is the first radial phonon mode and forces applied are due to the expansion of the confining potential. These oscillations decay rapidly, typically within a few oscillation periods for all scale factors and expansion velocities studied. If the trap were perfectly harmonic, this center-of-mass oscillation should be long-lived. In reality, our trap is more flat-bottomed, is anharmonic, and is not axially symmetric.

To understand this rapid decay, we show the atomic density and phase of a simulated Bose-Einstein condensate without an imprinted phonon during the first few oscillations after expansion in Fig. 4a and b, respectively. At $t = 10$ ms, the condensate reaches the far end of the potential and begins to turn around. At $t = 11.5$ ms, the condensate phase is approximately flat radially, with the exception of a discontinuity of $\approx \pi$ in the center of the annulus. This standing wave has nodes in the atomic density with corresponding π phase jumps, effectively imprinting a dark soliton onto the BEC [47, 48]. This process is analogous to the creation of solitons upon Bragg reflection in an optical lattice [49] or reflection of a condensate off of a tunnel barrier [50]. (Unfor-

tunately, due to imaging limitations, we are unable to resolve solitons or other similarly-sized structures in the experiment.)

The number of solitons N_s created from the decay of the radial mode can be estimated by comparing the energy per particles contained the radial excitation to the energy of a soliton per particle ($\epsilon_s \approx 4\hbar c/3R_T$, where R_T is the annular width of the ring). The amplitude of the radial excitation χ_r , while calculable analytically, is a complicated function that depends exponentially on the adiabaticity of the expansion relative to the frequency of the radial mode ω_r . Assuming a box-like potential in the radial direction implies $\omega_r \approx \pi c/R_T$. The adiabatic condition then implies that, in our system, \dot{R} must nearly be supersonic, i.e., $v_p \gtrsim 0.8c$ [51].

Turbulence and reheating- Dark solitons are unstable in condensates of more than one dimension. They suffer from a “snake instability” causing the soliton to first undulate and then fragment into vortex dipoles [52–54]. As shown by our numerics in Fig. 4a, the undulation is underway by 12.5 ms and the fragmentation into vortices is mostly complete by 14 ms. Theoretical estimates for a single soliton in a harmonically confined BEC suggest that the snake instability will result in $N_{vd,1} \approx 2\pi R/8\xi$ vortex pairs, where $\xi = \sqrt{\hbar^2/2M\mu}$ is the local healing length within the bulk of the condensate and μ is the chemical potential [55]. For the present case, this corresponds to $N_{vd,1} \approx 50$ vortex pairs. At $t = 13$ ms in Fig. 4b, the single soliton has decayed into ≈ 6 pairs over an angle $\approx 45^\circ$ near the top of the ring. This corresponds to roughly 48 vortex pairs around the full ring. These vortex pairs then form a highly turbulent state.

We experimentally observed the fingerprints of this process through the structure factor $S(k_\theta)$, a measure of the spatially structured density fluctuations (i.e., azimuthal phonons) with wavevector $k_\theta = m/R$. For both experiment and theory we extracted $S(k_\theta)$ by first evaluating the one-dimensional density $n_{1D}(\theta)$ around the ring to obtain the density fluctuations $\delta n_{1D}(\theta) = n_{1D}(\theta) - \langle n_{1D}(\theta) \rangle$, where $\langle \dots \rangle$ denotes the average over many realizations. The structure factor is

$$S(k_\theta) = \left\langle \left| \int \delta n_{1D}(\theta) e^{-ik_\theta R \theta} R d\theta \right|^2 \right\rangle. \quad (2)$$

Theoretical structure factors are shown in the top row of Fig. 4c; experimental structure factors are shown in the bottom row Fig. 4c. The colors in Fig. 4c identify the times at which the structure factors were evaluated. The density obtained from experiment has limited spatial resolution, is impacted by imaging aberrations, and has additional noise from the partial transfer absorption imaging process [56]. For these reasons, we first corrected for imaging aberrations (see Appendix A) and identified the detection threshold (shown by the horizontal, dashed lines). We used the numerical simulations (which include the same aberrations) to verify the correspondence between the corrected value of $S(k_\theta)$ based on simulated imaging to the value of $S(k_\theta)$ calculated from the simulated atomic density. These agree for values of $S(k_\theta)$ above the detection threshold.

As shown by the $S(k_\theta)$ snapshots, the structure factor starts at our detection threshold [57]. After expansion and during the soliton's initial formation ($t = 12$ ms), $S(k_\theta)$ maintains

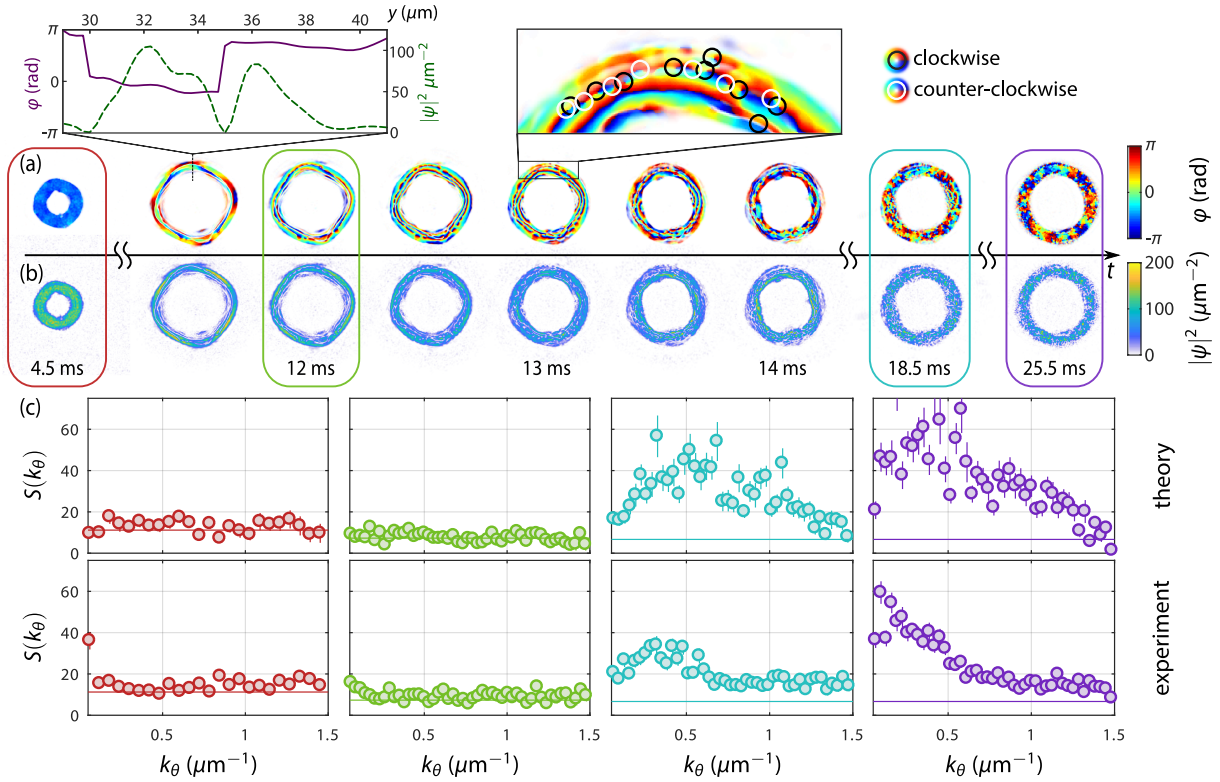


FIG. 4. Dynamics in the radial direction and generation of azimuthal excitations for a scale factor of $a = 1.9(1)$. (a–b) A single realization of the simulated BEC wavefunction’s phase (a) and magnitude $|\psi|^2$ (b) vs. time. (Left inset) Cross section along \hat{y} of the phase and density at $t = 11.5$ ms. (Right inset) Zoomed section of the phase profile at $t = 13$ ms with the location of vortices highlighted. (c) Azimuthal static structure factor. The color indicates the time, and matches the the vertical lines in Fig. 3 and the rectangles in (a) and (b). The horizontal lines indicate the imaging detection threshold (see text).

201 this value of unity, indicating that this state does not differ
 202 significantly between realizations. When the soliton begins to
 203 break apart at $t = 13$ ms, a small peak, still below our de-
 204 tection threshold, appears in the simulations near $k \approx 1 \mu\text{m}^{-1}$
 205 (not shown). This corresponds roughly to the wavenumber of
 206 the snake instability, $k \approx 2\pi/8\xi \approx 1.3 \mu\text{m}^{-1}$. As the turbu-
 207 lent state develops, this peak grows and shifts to lower k , be-
 208 coming detectable at 18.5 ms and becoming larger at 22.5 ms. The
 209 shift to lower k_θ is expected because of the inverse cascade that
 210 occurs in two-dimensional turbulence [58].

211 *Stochastic persistent currents* – While most of the vortex
 212 dipoles recombine and produce lower energy phonons, some
 213 of the vortex dipoles manage to break apart and become free
 214 vortices. If one of the free vortices slides into the center of
 215 the ring and one leaves the outside of the ring, then the over-
 216 all phase of the ring slips by 2π and the winding number ℓ ,
 217 quantifying the persistent current state of the ring, changes by
 218 one [59]. Indeed, we observe stochastic persistent currents in
 219 the ring after expansion in both the experiment and simulation.
 220 Figure 5a shows the resulting distributions of winding num-
 221 bers for various speeds of expansion for $a = 1.4$ ($R_f = 35 \mu\text{m}$
 222 and $R_i = 25 \mu\text{m}$).

223 Evidence for this process can be found by studying the
 224 width of the winding number distributions for expansions with
 225 different a and t_{exp} . The number of vortex dipoles produced
 226 from N_s solitons would be $N_{\text{vd}} \approx N_s(2\pi R_f/8\xi)$. The mea-
 227 sured distribution widths collapse reasonably well when plot-
 228 ted versus $N_{\text{vd}}^{1/4}$, as shown in Fig. 5b. The 1/4 may result from
 229 some combination of the stochastic nature of dipole disso-
 230 ciation and recombination, the interaction-driven dynamics of
 231 dipoles and free vortices in a turbulent fluid, and the random
 232 phase-slip process.

233 One may question whether the appearance of the wind-
 234 ing number might involve another cosmological phenomenon:
 235 the presence of sonic horizons. If we assume the speed of
 236 sound sets a limit on the speed at which information can
 237 travel through the condensate, the rapid supersonic expansion
 238 should create regions of condensate that are causally discon-
 239 nected. The typical horizon distance established during the
 240 expansion would be given by,

$$R_{\text{hor}} = 2 \int_0^{\tau} c(t) dt \lesssim 2c_0 t_{\text{exp}} \quad (3)$$

241 where c_0 is the initial speed of sound [60]. This leads to

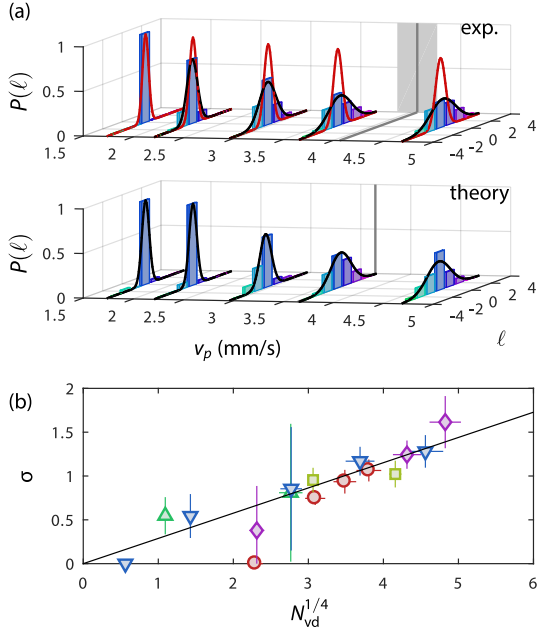


FIG. 5. (a) Measured winding number distributions for $a = 1.4(1)$ (histograms) with Gaussian fits (black curves) for the experiment (top) and simulations (bottom). The gray, vertical line and bar shows, for comparison, the speed of sound and its uncertainty. The red Gaussians show the expected distribution from the horizon model (see text). (b) Width of the winding number distribution σ vs. the number of vortex dipoles predicted by the soliton model, N_{vd} . The red circles denote $a = 1.31(9)$ [$R_i = 16.7(8) \mu\text{m}$, $R_f = 22(1) \mu\text{m}$], yellow squares $a = 1.9(1)$ [$R_i = 16.7(8) \mu\text{m}$, $R_f = 31(2) \mu\text{m}$], green triangles, $a = 2.3(2)$ [$R_i = 16.7(8) \mu\text{m}$, $R_f = 39(2) \mu\text{m}$] and blue inverted triangles, $a = 1.4(1)$ [$R_i = 25(1) \mu\text{m}$, $R_f = 35(2) \mu\text{m}$]. The purple diamonds also show $a = 1.4(1)$, but with a ring that is twice as wide. Solid line shows $\sigma = N_{\text{vd}}^{1/4}$.

$N_R \gtrsim 2\pi R_f / R_{\text{hor}} \approx \pi R_f / c_0 t_{\text{exp}}$ disconnected regions. If these regions' phases evolve at different rates and become sufficiently randomized, then when the regions recombine, they can form a topological excitation in the form of a persistent current [61, 62]. The probability for a given persistent current is then given by the geodesic rule [62–64]. The red Gaussians in Fig. 5a show the expected distributions resulting from this horizon model, which disagree with the experiment. Moreover, simple estimates for the phase fluctuations present in our condensate are a factor of 25 too low to sufficiently randomize the phase during expansion. Future studies using condensates of lower density could see this effect, as the phase fluctuations will be larger.

Discussion and Outlook – In this work, we explored the physics of a rapidly expanding Bose-Einstein condensate. We observed the redshifting of phonons during this rapid expansion, which has clear analogs in cosmological physics. After expansion stops, the condensate reheats through the creation and subsequent destruction of dark solitons, producing a highly turbulent state. This process leads to the creation

of global topological defects (i.e., persistent currents), which at first might be thought to arise due to the presence of cosmological horizons, but actually result from the vortices produced when the solitons break apart.

While we see evidence for Hubble friction in our system, future studies should be able to more precisely measure its influence during the expansion of the phonon modes. In particular, by varying \dot{R}/R , one could more easily distinguish between the Hubble friction and other damping effects. One could also contract the ring rather than expand it. Because the Hubble friction is not dissipative and is reversible, such a contraction should cause amplification of the phonon mode amplitude.

The process of expansion, which presumably cools the azimuthal degrees of freedom of the condensate, followed by the increase in azimuthal excitations (Fig. 4c-d) as the radial mode decays, is reminiscent of the reheating process in the early universe. At the end of inflation in the universe, the energy contained in the homogeneous mode of the quantum field that drove inflation, the inflaton, decayed into inhomogeneous excitations. It is not known how this occurred. In the simplest model, the inflaton oscillated around the minimum of its potential, decaying into lower energy particles [3], whereby the radial mode couples directly to lower energy azimuthal phonon modes. However, the decay of the radial mode through this process is expected to be much slower ($\approx 1 \text{ s}^{-1}$, using a calculation similar to that found in Ref. [65]) compared to the observed decay of the radial mode through soliton and vortex excitations ($\approx 100 \text{ s}^{-1}$). Future studies using a ring with stronger radial confinement should suppress the non-linear excitations and enhance the direct coupling. Other models are non-perturbative and include self-interactions in the inflaton field that can lead to turbulent cascading [4–9], much like the turbulence we observe here.

Perhaps surprisingly, the long-wavelength azimuthal phonon mode is redshifted in simple way (Fig. 2), despite the complex dynamics occurring in the underlying BEC state. This survival has a direct analogy in inflationary cosmology. During inflation, vacuum fluctuations were redshifted to large length scales and amplified. The subsequent preheating and thermalization processes took place on shorter length scales, yet the resulting thermal state was modulated by the long-wavelength amplified vacuum fluctuations. This process gave rise to the large-scale structure we observe today in the universe.

In addition to the possibilities described above, we anticipate that with new developments, other interesting cosmological phenomena might be realized with expanding condensates. First, with improved imaging that captures the initial (quantum and/or thermal) fluctuations, one could observe effects related to the scaling of the vacuum. In particular, one could observe cosmological particle production [23–29]. Second, a ring with stronger radial confinement will suppress transverse excitations, revealing the physics arising from the recombination of causally-disconnected regions. Given these possibilities, we believe an expanding ring BEC could provide an interesting laboratory test bed for cosmological physics.

ACKNOWLEDGMENTS

319

320 The authors thank J. Ho for initial discussions and a care-
 321 ful reading of the manuscript. We thank W.D. Phillips, E.
 322 Goldschmidt, M. Edwards and N. Proukakis for useful dis-
 323 cussions. This work was partially supported by ONR and the
 324 NSF through the PFC at the JQI. TJ was supported in part by
 325 NSF grants PHY-1407744 and PHY-1708139. IBS was par-
 326 tially supported by the AFOSR's Quantum Matter MURI and
 327 NIST.

Appendix A: Experimental Details

328

329 Our experimental setup consists of a BEC of ^{23}Na atoms
 330 in an optical dipole trap (ODT). Our BECs are created using
 331 standard laser cooling techniques, followed by evaporation in
 332 first magnetic then optical dipole traps. In this experiment,
 333 we work with BECs with between 1×10^5 and 4×10^5 atoms.
 334 For measurement, we use partial transfer absorption imaging
 335 (PTAI) [56].

336 The final stage of evaporation begins when thermal atoms
 337 are loaded into a combination of the vertical trap and dimple
 338 trap. Vertical confinement is created using a blue-detuned
 339 (532 nm), TEM₀₁ beam, tightly focused to create two paral-
 340 lel sheets of light with a dark region in between. The dimple
 341 trap is a red-detuned (1064 nm) Gaussian beam with $1/e^2$ di-
 342 ameter $\approx 50 \mu\text{m}$ that provides the initial confinement in the
 343 horizontal plane. Forced dipole evaporation occurs by lower-
 344 ing the intensity of both the blue-detuned vertical confinement
 345 beam and the red-detuned Gaussian beam until the condensate
 346 reaches a condensate fraction $> 95\%$. We estimate the initial
 347 temperature to be of the order of 50 nK by extrapolation of
 348 the evaporation process [66]. The final vertical trapping fre-
 349 quency is 650(4) Hz. The atoms are then adiabatically trans-
 350 ferred to the initial trap for the experiment.

351 To create the initial ring (or target) trap, we use a direct
 352 intensity masking technique [67] to create the blue-detuned
 353 (532 nm) trap in any shape. This approach images the face
 354 of a digital micromirror device (DMD) that is illuminated by
 355 a blue-detuned Gaussian beam and imaged onto the atoms.
 356 The pattern written onto the DMD is then transferred onto
 357 the potential experienced by the atoms. Using this technique,
 358 we can form fully-dynamic potentials in the shape of rings
 359 (with radii between $10 \mu\text{m}$ and $45 \mu\text{m}$) and target shaped traps
 360 (for measuring the persistent current state of the ring). The
 361 $1/e^2$ radius of the Gaussian beam that illuminates the DMD is
 362 $130(10) \mu\text{m}$ in the plane of the atoms.

363 Nominally, the pattern written on the DMD is given by

$$V_{\text{DMD}}(r) = \Theta([R(t) - R_T/2] - \rho) + \Theta(\rho - [R(t) + R_T/2]), \quad (\text{A1})$$

364 where Θ is the Heaviside step function, R_T is the ring's
 365 width, and ρ is the radial coordinate. For rings thinner than
 366 $R_T < 10 \mu\text{m}$, we apply corrections by changing R_T with angle
 367 θ to make the measured $n_{1D}(\theta)$ density of the condensate more
 368 uniform.

369 To expand the ring, we apply a time-dependent potential
 370 using our DMD. To minimize spurious effects related to jerk,

371 we used a smoothly varying function of the form

$$R(t) = \begin{cases} R_i & t \leq 0 \\ R_i + \frac{1}{2}(R_f - R_i)(1 + \text{erf}\left\{\frac{1}{\beta}\left(\frac{t}{t_{\text{exp}}} - \frac{1}{2}\right)\right\}) & 0 < t \leq t_{\text{exp}} \\ R_f & t > t_{\text{exp}} \end{cases}, \quad (\text{A2})$$

372 where erf is the error function and β is a parameter that min-
 373 imizes the jerk at $t = 0$ and $t = t_{\text{exp}}$. For the data reported
 374 in this paper, $\beta = 0.175$, which implies that at $t = 0$ and t_{exp}
 375 the radius suddenly jumps by $\approx 3 \times 10^{-5}(R_f - R_i)$. The DMD
 376 is pre-programmed with individual frames with ring radii cal-
 377 culated using Eq. A2. We typically use ≈ 30 frames spaced
 378 $\approx 300 \mu\text{s}$ to encode the expansion of the ring. Given our typ-
 379 ical chemical potentials of ≈ 1 kHz, this update rate is faster
 380 than all other timescales in the system. Moreover, we checked
 381 that our results are independent of the number of frames used.
 382 During the expansion, we increase the intensity of the trap-
 383 ping light to maintain constant intensity locally near the ring
 384 (compensating for the Gaussian profile of the beam illuminat-
 385 ing the DMD). We tune the increase in the trapping light to
 386 keep the frequency of the first radial Bogoliubov mode con-
 387 stant with radius.

388 To imprint a phonon of mode number m , we instantly
 389 change this pattern to

$$V_{\text{DMD}}(r, \theta) = \Theta\left(\left[R(t) - \frac{R_t}{2}\right] - \rho\right) + \Theta\left(\rho - \left[R(t) + \frac{R_t}{2}\right]\right) \\ + \frac{\lambda}{2} \Theta\left(\rho - \left[R(t) - \frac{R_t}{2}\right]\right) \Theta\left(\left[R(t) + \frac{R_t}{2}\right] - \rho\right) \\ \times [1 + \sin(m\theta)]. \quad (\text{A3})$$

390 Here $\lambda = 0.6$ is a parameter that describes the size of the
 391 perturbation relative to overall potential depth. One cannot
 392 generate the necessary values between 0 and 1 to produce the
 393 potential described by Eq. A3 with a binary DMD device. To
 394 get the necessary grayscale to create the potential, the DMD
 395 is demagnified in order to make its pixel size ($\approx 0.5 \mu\text{m}$ in the
 396 plane of the atoms) be much smaller than the aberrated point
 397 spread function ($\approx 4 \mu\text{m}$ $1/e^2$ full-width) of our imaging sys-
 398 tem. We then use halftoning to create the necessary grayscale
 399 effect. Ref. [68] contains more details about this imprinting
 400 process.

401 To measure the normalized phonon amplitude after imprint-
 402 ing, we first measure the 2D density *in situ* with $(n_{2D}(\rho, \theta))$ and
 403 without $(n_{2D,0}(\rho, \theta))$ the phonon imprinted. We then integrate
 404 over the radial dimension to obtain the 1D density around the
 405 ring, e.g., $n_{1D}(\theta) = \int n_{2D}(\rho, \theta) d\rho$. To obtain the normalized
 406 1D density, we compute $n_{1D}(\theta)/n_{1D,0}(\theta)$. Finally, the data are
 407 fit to $a_m \sin(m(\theta + \theta_0))$ at each time to extract the normalized
 408 amplitude of the phonon $a_m(t)$. The offset angle θ_0 is set by
 409 the imprinting process. Finally, we turn $a_m(t)$ into real phonon
 410 amplitude $\delta n(t)$ by multiplying by the total number of atoms
 411 and dividing by the estimated Thomas-Fermi volume of the
 412 condensate V_{TF} . Here, we have made two implicit assump-
 413 tions. First, we have assumed that the phonon's amplitude is
 414 independent of ρ and z , which is valid when the thickness of
 415 the annulus is small compared to its radius. (See Appendix C
 416 for details.) Second, we have assumed that the Thomas-Fermi
 417 volume scales in the experiment according to how it would in

418 a potential that is quartic in ρ and harmonic in z . With the
 419 same assumptions on the potential, the predicted frequency
 420 shift scales as $a^{9/7}$, which agrees rather well with the experi-
 421 ment (Fig. 2c). We also note that an incorrect estimate of the
 422 original Thomas-Fermi volume would lead to a common scal-
 423 ing of the phonon amplitude at all later times (before and after
 424 expansion), which would not lead to any change in either the
 425 fitted frequency shift or Hubble friction.

426 Calibration of the aberrations in our imaging system is nec-
 427 essary in order to accurately measure the correlation function
 428 $S(k)$. Conveniently, PTAI allows us to accurately calibrate
 429 our imaging system's sensitivity to density structures with
 430 wavevector k . When the transfer fraction f is low ($f \ll 1$),
 431 quantum shot noise is added and dwarfs the thermal and quan-
 432 tum fluctuations inherent to the condensate. This additional
 433 noise is white over all k , thus allowing for accurate calibration.
 434 To calibrate, we measure $n_{1D}(\theta)$ as described above and then
 435 construct $S(k)$ as described in the main text. To compensate
 436 for the our imaging system's degraded performance at larger
 437 k_θ , we minimize the functional $(\frac{S(k)}{C(k)} - \frac{1}{f})^2$ using the tunable
 438 parameters k_1 , p_1 , k_2 and k_3 contained within the correction
 439 function:

$$C(k) = \frac{1}{\sqrt{1 + |k/k_1|^{p_1}}} \frac{1}{\sqrt{1 + |k/k_2|^{p_2}}}. \quad (\text{A4})$$

440 The experimentally determined parameters are $k_1 =$
 441 $0.34(2) \mu\text{m}^{-1}$, $p_1 = 3.4(2)$, $k_2 = 1.50(4) \mu\text{m}^{-1}$ and $p_2 = 15(6)$.

442 To measure the persistent current state, we form a trap with
 443 a ring and a concentric, central disc (i.e., a target symbol) and
 444 use the interference between the two in time-of-flight to deter-
 445 mine the winding number [69, 70]. To produce acceptable inter-
 446 ference fringes for readout, the disc must also be expanded.
 447 This is done adiabatically over 25 ms with 40 frames.

448 Expansion of the ring produces a host of excitations, in-
 449 cluding phonons, vortices in the ring, and persistent currents.
 450 To accurately measure the persistent current with the least
 451 amount of interference from other excitations, we let the ring
 452 equilibrate for about 5 s. During this period, the intensity of
 453 light is ramped to $\approx 60\%$ of its value at the end of expansion
 454 to force evaporation of high energy excitations.

455 Appendix B: Stochastic-Projected Gross-Pitaevskii Calculations

456 To explore the behavior of our system numerically, we
 457 conducted simulations of the stochastic projected Gross-
 458 Pitaevskii equation [43, 44]. This numerical framework ex-
 459 tends the ordinary Gross-Pitaevskii equation to non-zero tem-
 460 perature, adding on fluctuations to the BEC ground state.
 461 While described in detail in the aforementioned references,
 462 we will briefly describe the technique here. In this formal-
 463 ism, the wavefunction of the BEC with fluctuations evolves in
 464 a ‘‘coherent’’ region – defined as the region of Hilbert space
 465 spanned by the state vectors that impact the dynamics of the
 466 BEC coherently. The BEC wavefunction in this C-region
 467 evolves as

$$(S)d\psi = d\psi_H + d\psi_G + (S)d\psi_M \quad (\text{B1})$$

468 where (S) denotes Stratonovich integration and

$$d\psi_H = \mathcal{P} \left\{ -\frac{i}{\hbar} \mathcal{L} \psi dt \right\} \quad (\text{B2})$$

$$d\psi_G = \mathcal{P} \left\{ \frac{G(\mathbf{r})}{k_B T} (\mu - \mathcal{L}) \psi dt + dW_G(\mathbf{r}, t) \right\} \quad (\text{B3})$$

469 Here, $\mathcal{L} = H_{sp} + U_0 |\psi|^2$ is the driver of Hamiltonian evolu-
 470 tion and $H_{sp} = p^2/2M + V$ is the single particle Hamiltonian.
 471 The equation for $d\psi_G$ represents growth of population in the
 472 C-region from particles colliding in the incoherent (I) region.
 473 Here, $G(\mathbf{r})$ is a coefficient that sets the strength of both terms
 474 in Eq. B3, where the first term is the damping term and the sec-
 475 ond is the growth term where dW_G describes a random noise
 476 seeded according to $\langle dW_G^*(\mathbf{r}', t') dW_G(\mathbf{r}, t) \rangle = 2G(\mathbf{r}) \delta(\mathbf{r}' - \mathbf{r}) dt$.
 477 For this work, we neglect terms where there is an exchange of
 478 energy and momentum between the C and I region without
 479 exchange of particles [43]. Finally, the projector operator \mathcal{P}
 480 continually projects the wavefunction into the C region.

481 From an implementation perspective, this involves taking a
 482 Gross-Pitaevskii equation solver and adding a noise term, and
 483 appropriately calculating the damping factor $G(\mathbf{r})$, which is
 484 assumed to be constant. Our calculations are done in a Carte-
 485 sian coordinate system. We apply the projection operator in
 486 momentum space, with a cutoff $k_c \approx \pi/\delta x$, where δx is the
 487 spacing between points in the grid.

488 To accurately capture the potential, we simulate the imag-
 489 ing process that is used to make the potential. We reproduce
 490 the image that is patterned on the DMD and simulate imaging
 491 using Fourier imaging techniques. The aperture function of
 492 the imaging system that relays the image from the DMD to
 493 the atoms is crucial in order to accurately replicate the poten-
 494 tial at the atoms. In the experiment, the same imaging system
 495 that is used for making potentials is also used for imaging
 496 of the atoms. By measuring density-density correlations in a
 497 simple-connected thermal gas with noise dominated by quan-
 498 tum shot noise (by using $f \ll 1$), we can extract the even
 499 (symmetric under parity reversal) aberrations [71]. To extract
 500 the odd aberrations, we use a less precise means. A second
 501 DMD in the Fourier plane of the imaging system can be used
 502 to measure the geometric spot diagram, yielding another, in-
 503 dependent means of obtaining the aperture function. The two
 504 methods are in agreement. We use the even aberrations from
 505 the correlations and the odd aberrations for the spot diagram
 506 technique to construct the aperture function.

507 The resulting potential is complicated and not easily ex-
 508 pressible in an analytic form. However, when azimuthally av-
 509 eraged, the potential has the form $V = \frac{1}{2} M \omega_r^2 (\rho - R(t))^2 +$
 510 $\lambda (\rho - R(t))^4$, with $\omega_r \approx 2\pi \times 100$ Hz and $\lambda/\hbar \approx 0.8$ Hz μm^{-4} .
 511 Because most ($\approx 90\%$) of the confinement comes from the
 512 quartic term, it is generally acceptable to neglect the quadratic
 513 term for the purposes of calculating static properties like the
 514 initial and final μ and c .

515 We combine the aperture function with the Gaussian beam.
 516 We assume the beam is perfectly Gaussian and is centered on
 517 the DMD. Because the beam portion of the potential tends
 518 toward zero as $r \rightarrow \infty$, we establish a low energy potential
 519 floor at large radius. This cutoff is determined by the min-
 520 imum value of the imaged and aberrated potential between

521 $R + \frac{3}{2}R_l < \rho < R + 1.1 \times \frac{3}{2}R_l$. This presents spurious effects
522 like the appearance of additional BEC components out at large
523 radius.

524 Given that some atoms are lost during the expansion, we
525 must also include absorbing boundary conditions in the simu-
526 lation. We do this by including a potential

$$V_a = \begin{cases} 0 & \rho < R_c \\ -iV_a e^{-w_a/(\rho-R_c)} & \rho > R_c \end{cases}, \quad (\text{B4})$$

527 where R_c is a radial cutoff at which the potential turns on, V_a
528 is the amplitude of the potential, and w_a is a parameter that
529 controls the width. The function is a non-analytic, contin-
530 uously differentiable function that minimizes the reflections
531 from the absorbing boundary. We chose $w_a \approx 25 \mu\text{m}$ and
532 $V_a/h \approx 1 \text{ kHz}$. This generally results in the best absorption
533 and the least reflection.

534 With all of these components, we first find the equilibrium
535 state by evolving the SPGPE (without V_a) for approximately
536 50 ms to 100 ms and a growth and decay term that are 100
537 times that of the value specified by the temperature (this al-
538 lows for faster equilibration times). Second, we expand the
539 ring according to that the same profile as seen in the exper-
540 iment. Approximately halfway through the experiment, we
541 turn on V_a to ensure that the decay of the atom number is
542 appropriately captured. After evolving for a total of approx-
543 imately 35 ms (20 ms additional after the end of the expan-
544 sion), we turn off the stochastic growth term in the SPGPE
545 and turn on significant damping to determine whether or not
546 a winding number is present in the condensate. We do this
547 approximately 25 independent times to gather statistics.

548 We then use the same data analysis tools used on the ex-
549 perimental data to extract the winding number distributions,
550 structure factor as a function of time, and radius of the ring
551 as a function of time. The structure factor, as was done in the
552 experiment, is measured relative to the mean density around
553 the ring. As a result, the structure factor is determined solely
554 by the differences in density between a given simulation and
555 the mean of all the simulations.

556 Appendix C: Evolution of azimuthal phonons

557 In this appendix, we derive the wave equation satisfied by
558 the phonon field, and explain the origin of the redshifting and
559 Hubble friction. We start by noting that the Gross-Pitaevskii
560 equation, written in terms of the density n and phase ϕ defined
561 through $\psi = \sqrt{n(\mathbf{r}, t)}e^{i\phi(\mathbf{r}, t)}$, can be expressed as an ideal fluid
562 with an equation for continuity,

$$-\frac{\partial n}{\partial t} = \frac{\hbar}{m} \nabla \cdot (n \nabla \phi), \quad (\text{C1})$$

563 and an equation analogous to the Euler equation,

$$-\hbar \frac{\partial \phi}{\partial t} = -\frac{\hbar^2}{2m\sqrt{n}} \nabla^2 \sqrt{n} + \frac{\hbar^2}{2m} (\nabla \phi)^2 + V + U_0 n, \quad (\text{C2})$$

564 where V is the potential for the atoms, $U_0 = 4\pi\hbar^2 a_s/M$ is
565 the interaction constant, M is the mass of an atom, and a_s is

the s -wave scattering length. In this treatment, we neglect the
566 quantum pressure term (the first term on the right hand side of
567 Eq. C2). By linearizing the equations about the background
568 solution n_0 and ϕ_0 , i.e., $n = n_0 + n_1$ and $\phi = \phi_0 + \phi_1$, one
570 obtains the coupled differential equations

$$\frac{\partial n_1}{\partial t} = -\frac{\hbar}{m} \nabla \cdot [n_0 \nabla \phi_1 + n_1 \nabla \phi_0] \quad (\text{C3})$$

$$-\hbar \frac{\partial \phi_1}{\partial t} = \frac{\hbar^2}{m} \nabla \phi_0 \cdot \nabla \phi_1 + U_0 n_1. \quad (\text{C4})$$

(In the main text, we use $\delta n = n_1$.) Solving the second equa-
571 tion for n_1 and inserting into the first yields a wave equation
572 for ϕ_1 , which, expressed in covariant form, is

$$\frac{1}{\sqrt{-g}} \partial_\mu (\sqrt{-g} g^{\mu\nu} \partial_\nu \phi_1) = 0, \quad (\text{C5})$$

574 where $g^{\mu\nu}$ is the inverse metric, g is the metric's determinant,
575 and ϕ_1 is the phonon's velocity potential field. The metric, in
576 its most general form, is given by the line element

$$ds^2 = g_{\mu\nu} dx^\mu dx^\nu \\ = c_0 \left[-c_0^2 dt^2 + (\mathbf{dx} - \mathbf{v}_0 dt) \cdot (\mathbf{dx} - \mathbf{v}_0 dt) \right]. \quad (\text{C6})$$

577 Here, $\mathbf{v}_0 = (\hbar/m) \nabla \phi_0$ is the velocity field of the background
578 condensate, and $c_0 = \sqrt{U_0 n_0 / M}$ is the speed of sound.

579 In the expanding ring experiment, the potential is (approx-
580 imately) axisymmetric, and is translated radially as a function
581 of time. In terms of cylindrical coordinates (ρ, θ, z) , the ve-
582 locity \mathbf{v}_0 thus has only ρ and z components, with its dominant
583 component being radial. The central radius of the ring is given
584 by a function $\rho = R(t)$ so, assuming the velocity is purely ra-
585 dial, the line element [Eq. C6] takes the form

$$ds^2 = c_0 [-c_0^2 dt^2 + (R + \tilde{\rho})^2 d\theta^2 + d\tilde{\rho}^2 + dz^2] \quad (\text{C7})$$

586 where $\tilde{\rho} = \rho - R(t)$ is a co-moving radial coordinate. The
587 tensor density that directly enters the wave equation [Eq. C5]
588 is then, in $(t, \theta, \tilde{\rho}, z)$ coordinates,

$$f^{\mu\nu} := \sqrt{-g} g^{\mu\nu} = (R + \tilde{\rho}) \text{diag}[-1, c_0^2/(R + \tilde{\rho})^2, c_0^2, c_0^2]. \quad (\text{C8})$$

589 The speed c_0 is determined by the background condensate
590 density, which to a first approximation follows the instanta-
591 neous ground state Thomas-Fermi distribution at all times dur-
592 ing the expansion,

$$n_0 = \frac{\mu - V(\tilde{\rho}, z)}{U_0} \quad (\text{C9})$$

593 This density extends out to the contour in the $\tilde{\rho}$ - z plane where
594 the numerator vanishes. The chemical potential μ drops as
595 the ring expands, so that the total number of atoms remains
596 constant.

597 In the experiment, we first apply a perturbation to a sta-
598 tionary condensate to excite an eigenmode of the wave equa-
599 tion. An eigenmode analysis based on the methods of
600 Ref. [72] will be detailed in a forthcoming paper; the es-
601 sential details are presented here. Assuming azimuthal sym-
602 metry, the eigenmodes for a thin ring have the form $\phi_1 =$

603 $\chi_{klm}\eta_{klm}(\tilde{\rho}, z; R)e^{i(\omega t - m\theta)}$, where $\eta_{klm}(\tilde{\rho}, z; R)$ is a function that
 604 describes the radial (k) and vertical excitations (l) of the Bogoliubov mode when the ring has radius R , and χ_{klm} is its
 605 amplitude. We denote the corresponding eigenfrequencies as
 606 ω_{klm} .

608 While the system may begin with only a $k = l = 0$ eigen-
 609 mode excited, the expansion of the ring can produce transi-
 610 tions into other modes. The solution at all times takes the
 611 general form $\phi_1(t, \tilde{\rho}, \theta, z) = \sum_{klm} \chi_{klm}(t)\eta_{klm}(\tilde{\rho}, z)e^{-im\theta}$, with all
 612 $\chi_{klm}(t = 0) = 0$ except for $k, l = 0$ and our excited mode of
 613 interest m . Azimuthal symmetry precludes coupling between
 614 modes with different values of m . Furthermore, in the thin
 615 ring limit, the coupling between different k modes tends to-
 616 wards zero. We therefore focus here exclusively on modes
 617 that are excited only in the azimuthal direction. (The radial
 618 excitation which occurs when the ring expansion stops and is
 619 not relevant to the redshift is discussed in the main text.)

620 When $m \ll \omega_{100}/(c_\theta/R)$ and for a thin ring, $\eta_{00m}(\tilde{\rho}, z; R)$
 621 is constant. (Henceforth, we will drop the k and l subscripts
 622 when they are both equal to zero.) In this limit, the equation
 623 for modes with $k, l = 0$ involves just t and θ derivatives, We
 624 can thus reduce the wave equation for these azimuthal phonon
 625 modes to a 1+1 dimensional wave equation, with an effective
 626 sound speed c_θ . As in Ref. [72], c_θ^2 is given by an average over
 627 the cross section of the ring. For a thin ring this takes the form

$$c_\theta^2 = \frac{1}{AM} \int [\mu - V(\tilde{\rho}, z)] d\tilde{\rho}dz, \quad (\text{C10})$$

628 where the integral is over the cross section of the Thomas-
 629 Fermi wavefunction of area A . For $V = \frac{1}{2}M\omega_z^2 z^2 + \lambda\tilde{\rho}^4$ this
 630 yields

$$c_\theta^2 = \frac{4}{7}c^2, \quad (\text{C11})$$

631 where $c^2 = \mu/M$ is the peak local sound speed. By normaliz-
 632 ing the Thomas-Fermi solution to the number of atoms N one
 633 finds that $\mu \propto R^{-4/7}$, and therefore $c_\theta \propto c \propto R^{-2/7}$.

634 The wave equation satisfied by our modes of interest, i.e.,
 635 $\phi_1 = \chi_m(t)e^{im\theta}$, is determined by the effective inverse metric
 636 density obtained from Eq. C8 by dropping the $\tilde{\rho}$ and z compo-
 637 nents and replacing c by c_θ . In the thin ring limit this gives

$$f_2^{ab} = \text{diag}[-R, c_\theta^2/R] \quad (\text{C12})$$

638 The resulting mode equation is

$$\ddot{\chi}_m + \frac{\dot{R}}{R}\dot{\chi}_m + \omega_m^2\chi_m = 0, \quad (\text{C13})$$

639 where $\omega_m := mc_\theta/R$. This is the equation of a damped har-
 640 monic oscillator, with time-dependent frequency and damp-
 641 ing rate. We note that this particular equation does not result
 642 from the wave equation for any 1+1 dimensional metric, since
 643 there exists no metric g_{2ab} for which $f_2^{ab} = \sqrt{-g}g^{ab}$. The rea-
 644 son is that the determinant of Eq. C12 is $-c_\theta^2$, whereas the de-
 645 terminant of $\sqrt{-g}g^{ab}$ is equal to -1 for any two-dimensional
 646 metric.

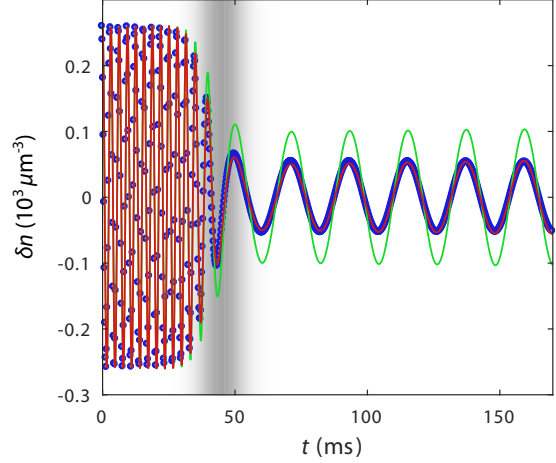


FIG. 6. Phonon evolution in the thin ring limit. Blue circles show 2D GPE simulation data, red (green) curve is the solution to Eq. C13 with (without) the \dot{R}/R ‘‘Hubble friction’’ term included. The gray band indicates the time during which the BEC is inflated; its intensity denotes the expansion velocity relative to the maximum.

647 As the ring expands, the azimuthal wavenumber m is con-
 648 served, so the physical wavelength redshifts as R^{-1} , in analo-
 649 gy with the cosmological redshift. Unlike in cosmology,
 650 the sound speed is also changing, so the frequency ω_m red-
 651 shifts as $R^{-9/7}$. In the cosmological setting, the damping term
 652 in Eq. C13 is called the ‘‘Hubble friction’’ term, and would
 653 be multiplied by 3 in three spatial dimensions. The Hubble
 654 damping is not actually dissipative; in fact, Eq. C13 can be ob-
 655 tained from the Lagrangian $L = \frac{1}{2}R\dot{\chi}_m^2 - \frac{1}{2}(m^2c_\theta^2/R)\chi_m^2$, which
 656 has the adiabatic invariant $R\omega_m\chi_m^2$. To obtain Eq. 1 in the text,
 657 we add the phenomenological damping γ_m observed in the ex-
 658 periment.

659 In the experiment, we measure the density variation n_1 , not
 660 the phonon velocity potential ϕ_1 . The relation between these
 661 quantities is given by Eq. C4. Since $\nabla\phi_1$ is azimuthal and $\nabla\phi_0$
 662 is radial, $\nabla\phi_0 \cdot \nabla\phi_1 = 0$, so we have

$$n_1 = -\frac{\hbar}{U_0}\dot{\phi}_1 = -\frac{\hbar}{U_0}\dot{\chi}_m e^{im\theta}. \quad (\text{C14})$$

663 Hence, in the experiment, we measure the time derivative of
 664 the phonon amplitude.

665 We can verify that a phonon excitation does indeed obey
 666 Eq. C13 in a thin ring, by simulating a BEC in this regime.
 667 Figure 6 shows such a 2D simulation of BEC in a radially
 668 quartic potential, expanding from 10 to 40 μm in ≈ 15 ms
 669 with 2×10^5 atoms. There is no damping in this simulation;
 670 therefore, the $\gamma_m(t)$ in Eq. 1 is identically zero. We choose
 671 the strength of the potential to make the initial Thomas-Fermi
 672 width be 2 μm . As can be seen from the figure, Eq. C13 ac-
 673 curately reproduces the behavior of the redshifted phonon, but
 674 only when the Hubble friction term is included. Unlike the
 675 experiment, the adiabatic limit is satisfied ($\partial\omega_m/\partial t \ll \omega_m^2$)
 676 and the final amplitude is accurately predicted using the adia-

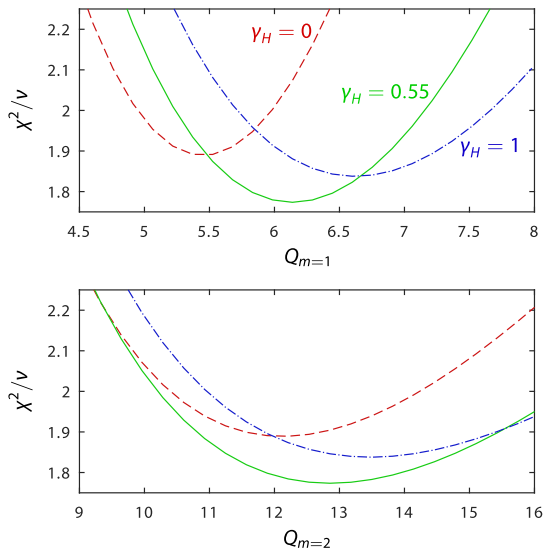


FIG. 7. Goodness of fit χ^2/ν , where ν is the number of degrees of freedom, versus quality factors for the $m = 1, 2$ modes for various values of γ_H .

batic invariant $R\omega_m\chi_m^2$. While this simulation shows the thin ring limit, we generally find that as we relax this constraint and increase the width of the annulus, the best-fit Hubble fric-

tion becomes less than unity, as might be expected from the experimental result.

For the experiment, we attempt to tease out the Hubble friction by fitting it along with the other parameters of Eq. 1. These parameters are the initial amplitudes, frequencies, and phases for each of the four expansions, the quality factor for the two m modes, $Q_m = \omega_m/2\gamma_m$, the scaling of the frequency with radius [expected to be $9/7 \approx 1.2875$, the best fit value is $1.19(2)$]. This fit therefore contains 15 parameters and 160 degrees of freedom. Fig. 7 shows the results of the reduced- χ^2 fit; it shows the value of χ^2 vs. both $Q_{m=1}$ and $Q_{m=2}$ in the vicinity of their best fit values for three values of γ_H , including the best fit value. There are several interesting features. First, the reduced- $\chi^2 > 1$, most likely because we do not have a good estimate of the statistical uncertainties (each point represents only four realizations of the experiment) and our model does not properly account for all the relevant effects (for example, the azimuthal asymmetry and non-zero annular thickness may play a non-negligible role in determining the phonon dynamics). Second, $\gamma_H = 1$ produces a better fit than $\gamma_H = 0$, but both are improved slightly by taking $\gamma_H = 0.55$. Third, the smallness of the change in the minimum of χ^2 with γ_H indicates our uncertainty in γ_H . (Part of this insensitivity comes from our choice, at the time of the experiment, to have $n_1 \propto \dot{\phi} \approx 0$ during the fastest part of the expansion, thereby inadvertently minimizing the effect of the Hubble friction [73].) Taken together, the evidence is consistent with $\gamma_H = 1$ but is not conclusive.

-
- [1] P.J.E. Peebles, *Principles of Physical Cosmology*, Princeton series in physics (Princeton University Press, 1993).
- [2] Daniel Baumann, “Inflation,” in *Physics of the Large and the Small* (World Scientific, 2012) pp. 523–686.
- [3] Lev Kofman, Andrei Linde, and Alexei A. Starobinsky, “Reheating after inflation,” *Phys. Rev. Lett.* **73**, 3195 (1994).
- [4] Gary Felder and Lev Kofman, “Development of equilibrium after preheating,” *Phys. Rev. D* **63**, 103503 (2001).
- [5] L. Kofman, “Tachyonic Preheating,” in *Particles, Strings, and Cosmology*, edited by P. Frampton and J. Ng (2001) p. 167, hep-ph/0107280.
- [6] Edmund J. Copeland, S. Pascoli, and A. Rajantie, “Dynamics of tachyonic preheating after hybrid inflation,” *Phys. Rev. D* **65**, 103517 (2002).
- [7] Marcelo Gleiser, Noah Graham, and Nikitas Stamatopoulos, “Long-lived time-dependent remnants during cosmological symmetry breaking: From inflation to the electroweak scale,” *Phys. Rev. D* **82**, 043517 (2010).
- [8] Mustafa A. Amin, Richard Easther, Hal Finkel, Raphael Flauger, and Mark P. Hertzberg, “Oscillons after inflation,” *Phys. Rev. Lett.* **108**, 241302 (2012).
- [9] Mustafa A. Amin, Mark P. Hertzberg, David I. Kaiser, and Johanna Karouby, “Nonperturbative Dynamics Of Reheating After Inflation: A Review,” *Int. J. Mod. Phys. D* **24**, 1530003 (2014).
- [10] L P Pitaevskii and S Stringari, *Bose-Einstein Condensation*, International Series of Monographs on Physics (Clarendon Press, 2003).
- [11] That is, neglecting the quantum pressure term.
- [12] W. G. Unruh, “Experimental black-hole evaporation?” *Phys. Rev. Lett.* **46**, 1351 (1981).
- [13] Uwe R. Fischer and Matt Visser, “Riemannian Geometry of Irrotational Vortex Acoustics,” *Phys. Rev. Lett.* **88**, 110201 (2002).
- [14] Carlos Barceló, Stefano Liberati, and Matt Visser, “Analogue gravity,” *Living Reviews in Relativity* **8**, 12 (2005).
- [15] L. J. Garay, J. R. Anglin, J. I. Cirac, and P. Zoller, “Sonic analog of gravitational black holes in Bose-Einstein condensates,” *Phys. Rev. Lett.* **85**, 4643 (2000).
- [16] L. J. Garay, J. R. Anglin, J. I. Cirac, and P. Zoller, “Sonic black holes in dilute Bose-Einstein condensates,” *Phys. Rev. A* **63**, 023611 (2001).
- [17] Ralf Schützhold, “Effective horizons in the laboratory,” in *Quantum Analogues: From Phase Transitions to Black Holes and Cosmology*, Lecture Notes in Physics, Vol. 718, edited by Ralf Schützhold and William G. Unruh (Springer, Berlin, Heidelberg, 2007) pp. 5–28.
- [18] P. Jain, A. S. Bradley, and C. W. Gardiner, “Quantum de Laval nozzle: Stability and quantum dynamics of sonic horizons in a toroidally trapped Bose gas containing a superflow,” *Phys. Rev. A* **76**, 023617 (2007).
- [19] Jean Macher and Renaud Parentani, “Black-hole radiation in Bose-Einstein condensates,” *Phys. Rev. A* **80**, 043601 (2009).
- [20] Oren Lahav, Amir Itah, Alex Blumkin, Carmit Gordon, Sha-

- har Rinott, Alona Zayats, and Jeff Steinhauer, “Realization of a Sonic Black Hole Analog in a Bose-Einstein Condensate,” *Phys. Rev. Lett.* **105**, 240401 (2010).
- [21] Jeff Steinhauer, “Observation of self-amplifying Hawking radiation in an analogue black-hole laser,” *Nat. Phys.* **10**, 864 (2014).
- [22] Jeff Steinhauer, “Observation of quantum Hawking radiation and its entanglement in an analogue black hole,” *Nat. Phys.* **12**, 959 (2016).
- [23] P. O. Fedichev and U. R. Fischer, “Gibbons-Hawking Effect in the Sonic deSitter Space-Time of an Expanding Bose-Einstein-Condensed Gas,” *Phys. Rev. Lett.* **91**, 240407 (2003).
- [24] Carlos Barceló, S. Liberati, and Matt Visser, “Probing semiclassical analog gravity in Bose-Einstein condensates with widely tunable interactions,” *Phys. Rev. A* **68**, 053613 (2003).
- [25] P. O. Fedichev and U. R. Fischer, “Cosmological” quasiparticle production in harmonically trapped superfluid gases,” *Phys. Rev. A* **69**, 033602 (2004).
- [26] U. R. Fischer and R. Schützhold, “Quantum simulation of cosmic inflation in two-component Bose-Einstein condensates,” *Phys. Rev. A* **70**, 063615 (2004).
- [27] E. A. Calzetta and B. L. Hu, “Early Universe Quantum Processes in BEC Collapse Experiments,” *International Journal of Theoretical Physics* **44**, 1691–1704 (2005).
- [28] Piyush Jain, Silke Weinfurter, Matt Visser, and C. W. Gardiner, “Analog model of a Friedmann-Robertson-Walker universe in Bose-Einstein condensates: Application of the classical field method,” *Phys. Rev. A* **76**, 033616 (2007).
- [29] Angus Prain, Serena Fagnocchi, and Stefano Liberati, “Analogue cosmological particle creation: Quantum correlations in expanding Bose-Einstein condensates,” *Phys. Rev. D* **82**, 105018 (2010).
- [30] A.D. Sakharov, “The Initial Stage of an Expanding Universe and the Appearance of a Nonuniform Distribution of Matter,” *Sov. Phys. JETP* **22**, 241 (1966).
- [31] Gerald T. Moore, “Quantum theory of the electromagnetic field in a variable-length one-dimensional cavity,” *J. Math. Phys.* **11**, 2679–2691 (1970).
- [32] Chen-Lung Hung, Victor Gurarie, and Cheng Chin, “From Cosmology to Cold Atoms: Observation of Sakharov Oscillations in a Quenched Atomic Superfluid,” *Science* **341**, 1213 (2013).
- [33] J.-C. Jaskula, G. B. Partridge, M. Bonneau, R. Lopes, J. Ruedel, D. Boiron, and C. I. Westbrook, “Acoustic analog to the dynamical Casimir effect in a Bose-Einstein condensate,” *Phys. Rev. Lett.* **109**, 220401 (2012).
- [34] F. Belgiorno, S. L. Cacciatori, M. Clerici, V. Gorini, G. Ortenzi, L. Rizzi, E. Rubino, V. G. Sala, and D. Faccio, “Hawking radiation from ultrashort laser pulse filaments,” *Phys. Rev. Lett.* **105**, 203901 (2010).
- [35] E. Rubino, J. McLenaghan, S. C. Kehr, F. Belgiorno, D. Townsend, S. Rohr, C. E. Kuklewicz, U. Leonhardt, F. König, and D. Faccio, “Negative-frequency resonant radiation,” *Phys. Rev. Lett.* **108**, 253901 (2012).
- [36] David Vocke, Calum Maitland, Angus Prain, Fabio Biancalana, Francesco Marino, Ewan M. Wright, and Daniele Faccio, “Rotating black hole geometries in a two-dimensional photon superfluid,” (2017), [arXiv:1709.04293](https://arxiv.org/abs/1709.04293).
- [37] Silke Weinfurter, Edmund W. Tedford, Matthew C. J. Penrice, William G. Unruh, and Gregory A. Lawrence, “Measurement of stimulated Hawking emission in an analogue system,” *Phys. Rev. Lett.* **106**, 021302 (2011).
- [38] L.-P. Euvé, F. Michel, R. Parentani, T. G. Philbin, and G. Rousseaux, “Observation of noise correlated by the Hawking effect in a water tank,” *Phys. Rev. Lett.* **117**, 121301 (2016).
- [39] Theo Torres, Sam Patrick, Antonin Coutant, Maurício Richartz, Edmund W. Tedford, and Silke Weinfurter, “Rotational superradiant scattering in a vortex flow,” *Nat. Phys.* **13**, 833–836 (2017), 1612.06180.
- [40] D. Faccio, F. Belgiorno, S. Cacciatori, V. Gorini, S. Liberati, and U. Moschella, *Analogous Gravity Phenomenology: Analogous Spacetimes and Horizons, from Theory to Experiment*, Lecture Notes in Physics (Springer International Publishing, 2013).
- [41] This forced expansion is different from the expansion of the universe, which is driven by the energy contained within it.
- [42] With perfect imaging, our potential would be flat-bottomed, but a combination of finite resolution and aberrations causes our potential to have both curvature and broken axial symmetry.
- [43] S. J. Rooney, P. B. Blakie, and A. S. Bradley, “Stochastic projected Gross-Pitaevskii equation,” *Phys. Rev. A* **86**, 053634 (2012).
- [44] A. S. Bradley, S. J. Rooney, and R. G. McDonald, “Low-dimensional stochastic projected Gross-Pitaevskii equation,” *Phys. Rev. A* **92**, 033631 (2015).
- [45] Unless stated otherwise, all uncertainties and errorbars in this paper are the uncorrelated combination of 1σ statistical and systematic uncertainties.
- [46] We measure $Q = \gamma_m/\omega_m \approx 6$ for all $m > 1$ and $Q \gtrsim 20$ for $m = 1$, indicating that the intrinsic damping γ_m is most likely Landau damping [65]. Q decreases slightly for increasing m and R . For fitting a given m , we take Q to be constant with time.
- [47] C.J. Pethick and H. Smith, *Bose-Einstein Condensation in Dilute Gases* (Cambridge University Press, 2002).
- [48] D J Frantzeskakis, “Dark solitons in atomic Bose-Einstein condensates: from theory to experiments,” *J. Phys. A Math. Theor.* **43**, 213001 (2010).
- [49] R. G. Scott, A. M. Martin, T. M. Fromhold, S. Bujkiewicz, F. W. Sheard, and M. Leadbeater, “Creation of Solitons and Vortices by Bragg Reflection of Bose-Einstein Condensates in an Optical Lattice,” *Phys. Rev. Lett.* **90**, 110404 (2003).
- [50] A. M. Martin, R. G. Scott, and T. M. Fromhold, “Transmission and reflection of Bose-Einstein condensates incident on a Gaussian tunnel barrier,” *Phys. Rev. A* **75**, 065602 (2007).
- [51] For the expansion described by Eq. A2, $\chi_r = (R_f - R_i) \exp[-(\beta\omega_r t_{\text{exp}})^2/4]$. Thus, we must compare the energy of the soliton to that of the energy in the radial mode, $\frac{1}{2}m\omega_r^2\chi_r^2$. The full adiabatic condition then becomes $v_p \gtrsim c(R_f - R_i)/R_f \times \sqrt{\pi} \left[\log \left(3\pi^2 mc(R_f - R_i)^2 / \hbar R_f \right) \right]^{-1/2}$.
- [52] E. A. Kuznetsov and S. K. Turitsyn, “Instability and collapse of solitons in media with a defocusing nonlinearity,” *Sov. Phys. JETP* **67**, 1583 (1988).
- [53] A. M. Kamchatnov and L. P. Pitaevskii, “Stabilization of Solitons Generated by a Supersonic Flow of Bose-Einstein Condensate Past an Obstacle,” *Phys. Rev. Lett.* **100**, 160402 (2008).
- [54] A. Cetoli, J. Brand, R. G. Scott, F. Dalfovo, and L. P. Pitaevskii, “Snake instability of dark solitons in fermionic superfluids,” *Phys. Rev. A* **88**, 043639 (2013).
- [55] L. A. Toikka and K. A. Suominen, “Snake instability of ring dark solitons in toroidally trapped Bose-Einstein condensates,” *Phys. Rev. A* **87**, 043601 (2013).
- [56] Anand Ramanathan, Sérgio R. Muniz, Kevin C. Wright, Russell P. Anderson, William D. Phillips, Kristian Helmer, and Gretchen K. Campbell, “Partial-transfer absorption imaging: a versatile technique for optimal imaging of ultracold gases,” *Rev. Sci. Instrum.* **83**, 083119 (2012).
- [57] In the simulations, $S(k_\theta)$ as computed from the density (as op-

- posed to simulated, aberrated images) is ≈ 1 at these early times. This corresponds to the equilibrium value for a condensate where $k_B T \approx \mu$, T is the temperature, and k_B is Boltzmann's constant.
- [58] Robert H. Kraichnan, "Inertial Ranges in Two-Dimensional Turbulence," *Phys. Fluids* **10**, 1417 (1967).
- [59] P. W. Anderson, "Considerations on the flow of superfluid helium," *Rev. Mod. Phys.* **38**, 298 (1966).
- [60] The approximation of constant speed of sound is good to within 10% because of the weak dependence of c on R .
- [61] W. H. Zurek, "Cosmological experiments in superfluid helium?" *Nature* **317**, 505 (1985).
- [62] David R. Scherer, Chad N. Weiler, Tyler W. Neely, and Brian P. Anderson, "Vortex Formation by Merging of Multiple Trapped Bose-Einstein Condensates," *Phys. Rev. Lett.* **98**, 110402 (2007).
- [63] M. J. Bowick, L. Chandar, E. A. Schiff, and A. M. Srivastava, "The cosmological kibble mechanism in the laboratory: string formation in liquid crystals." *Science* **263**, 943 (1994).
- [64] We find through Monte Carlo simulations that the probabilities are well described by normal distributions with $\sigma \approx 0.3 \sqrt{N_R}$.
- [65] L. P. Pitaevskii and S. Stringari, "Landau damping in dilute Bose gases," *Phys. Lett. A* **235**, 398 (1997).
- [66] A. Kumar, S. Eckel, F. Jendrzejewski, and G. K. Campbell, "Temperature-induced decay of persistent currents in a superfluid ultracold gas," *Phys. Rev. A* **95**, 021602 (2017).
- [67] Jeffrey G Lee and W T Hill, "Spatial shaping for generating arbitrary optical dipole traps for ultracold degenerate gases," *Rev. Sci. Instrum.* **85**, 103106 (2014).
- [68] A. Kumar, N. Anderson, W. D. Phillips, S. Eckel, G. K. Campbell, and S. Stringari, "Minimally destructive, Doppler measurement of a quantized flow in a ring-shaped Bose-Einstein condensate," *New J. Phys.* **18**, 025001 (2016).
- [69] Stephen Eckel, Jeffrey G. Lee, Fred Jendrzejewski, Noel Murray, Charles W. Clark, Christopher J Lobb, William D. Phillips, Mark Edwards, and Gretchen K. Campbell, "Hysteresis in a quantized superfluid 'atomtronic' circuit," *Nature* **506**, 200 (2014).
- [70] Laura Corman, Lauriane Chomaz, Tom Bienaimé, Rémi Desbuquois, C. Weitenberg, S. Nascimbène, Jean Dalibard, and Jérôme Beugnon, "Quench-Induced Supercurrents in an Annular Bose Gas," *Phys. Rev. Lett.* **113**, 135302 (2014).
- [71] Chen-Lung Hung, Xibo Zhang, Li-Chung Ha, Shih-Kuang Tung, Nathan Gemelke, and Cheng Chin, "Extracting density-density correlations from in situ images of atomic quantum gases," *New J. Phys.* **13**, 075019 (2011).
- [72] E Zaremba, "Sound propagation in a cylindrical Bose-condensed gas," *Phys. Rev. A* **57**, 518 (1998).
- [73] Our experiments were performed before we realized the significance of the Hubble friction effect, which was only later pointed out by our more enlightened theory co-author.

Bibliography

- [1] Anand Ramanathan. *A ring with a spin: superfluidity in a toroidal Bose-Einstein Condensate*. PhD thesis, University of Maryland, The address of the publisher, 7 2011. An optional note.
(Cited on pages [xi](#), [27](#), [31](#), [38](#), and [62](#).)
- [2] S. Eckel, F. Jendrzejewski, A. Kumar, C. J. Lobb, and G. K. Campbell. Interferometric measurement of the current-phase relationship of a superfluid weak link. *Phys. Rev. X*, 4:031052, Sep 2014.
(Cited on pages [xiii](#), [xiv](#), [23](#), [63](#), [67](#), [69](#), [71](#), [72](#), and [124](#).)
- [3] R. Mathew, A. Kumar, S. Eckel, F. Jendrzejewski, G. K. Campbell, Mark Edwards, and E. Tiesinga. Self-heterodyne detection of the in situ phase of an atomic superconducting quantum interference device. *Phys. Rev. A*, 92:033602, Sep 2015.
(Cited on pages [xiv](#), [23](#), [53](#), [73](#), and [76](#).)
- [4] Yi-Hsieh Wang, A. Kumar, F. Jendrzejewski, Ryan M. Wilson, Mark Edwards, S. Eckel, G. K. Campbell, and Charles W. Clark. Resonant wavepackets and shock waves in an atomtronic SQUID. 2015.
(Cited on pages [xiv](#), [xv](#), [xvi](#), [23](#), [77](#), [81](#), [82](#), [83](#), [89](#), [92](#), [95](#), [96](#), [98](#), [99](#), [101](#), and [110](#).)
- [5] A. Kumar, N. Anderson, W. D. Phillips, S. Eckel, G. K. Campbell, and S. Stringari. Minimally destructive, Doppler measurement of a quantized flow in a ring-shaped Bose-Einstein condensate. *New J. Phys.*, 18(2):025001, 2016.
(Cited on pages [xvi](#), [xvii](#), [104](#), [107](#), [111](#), [114](#), [116](#), and [118](#).)
- [6] A. Kumar, S. Eckel, F. Jendrzejewski, and G. K. Campbell. Temperature-induced decay of persistent currents in a superfluid ultracold gas. *Phys. Rev. A*, 95:021602, Feb 2017.
(Cited on pages [xvii](#), [xviii](#), [xix](#), [25](#), [37](#), [121](#), [125](#), [126](#), [129](#), [132](#), [136](#), [137](#), [139](#), and [141](#).)

- [7] Anand Ramanathan, Sergio R. Muniz, Kevin C. Wright, Russell P. Anderson, William D. Phillips, Kristian Helmerson, and Gretchen K. Campbell. Partial-transfer absorption imaging: A versatile technique for optimal imaging of ultracold gases. *Review of Scientific Instruments*, 83(8), 2012.
(Cited on pages [xvii](#) and [125](#).)
- [8] J. Li, H. Y. Guo, B. N. Wan, X. Z. Gong, Y. F. Liang, G. S. Xu, K. F. Gan, J. S. Hu, H. Q. Wang, L. Wang, L. Zeng, Y. P. Zhao, P. Denner, G. L. Jackson, A. Loarte, R. Maingi, J. E. Menard, M. Rack, and X. L. Zou. A long-pulse high-confinement plasma regime in the experimental advanced superconducting tokamak. *Nature Physics*, 9(11):817, 2013.
(Cited on page [1](#).)
- [9] A. E. Leanhardt, T. A. Pasquini, M. Saba, A. Schirotzek, Y. Shin, D. Kielpinski, D. E. Pritchard, and W. Ketterle. Cooling bose-einstein condensates below 500 picokelvin. *Science*, 301(5639):1513–1515, 2003.
(Cited on page [1](#).)
- [10] Heike Kamerlingh Onnes, editor. *Proceedings of the Academy of Sciences*, volume 4 of 5, 8 1908. In this brief note to the 1908 Academy of Sciences, Heike Kamerlingh Onnes reports on the first liquefaction of helium which will earn him the Nobel Prize in 1913. He then reaches a temperature of about -271.5 C , a little more than 1 degree above absolute zero.
(Cited on page [2](#).)
- [11] H. Kammerlingh Onnes. *Commun. Phys. Lab. Univ. Leiden.*, page 122b, 1911.
(Cited on page [2](#).)
- [12] H. Kammerlingh Onnes. *Koninkl. Ned. Akad. Wetenschap.*, 23:278, 1914.
(Cited on pages [2](#) and [122](#).)
- [13] P. Kapitza. Viscosity of Liquid Helium below the λ -Point. *Nature*, 141:74, January 1938.
(Cited on page [2](#).)
- [14] J.F. Allen and A.D. Misener. Flow Phenomena in Liquid Helium II. *Nature*, 142:643, October 1938.
(Cited on page [2](#).)
- [15] J. Bardeen, L. N. Cooper, and J. R. Schrieffer. Theory of superconductivity. *Phys. Rev.*, 108:1175–1204, Dec 1957.
(Cited on page [2](#).)
- [16] M. H. Anderson, J. R. Ensher, M. R. Matthews, C. E. Wieman, and E. A. Cornell. Observation of bose-einstein condensation in a dilute atomic vapor. *Science*, 269(5221):198–201, 1995.
(Cited on pages [4](#) and [13](#).)

- [17] K. B. Davis, M. O. Mewes, M. R. Andrews, N. J. van Druten, D. S. Durfee, D. M. Kurn, and W. Ketterle. Bose-einstein condensation in a gas of sodium atoms. *Phys. Rev. Lett.*, 75:3969–3973, Nov 1995.
(Cited on pages 4 and 13.)
- [18] J. M. Kosterlitz and D. J. Thouless. Ordering, metastability and phase transitions in two-dimensional systems. *Journal of Physics C Solid State Physics*, 6:1181–1203, April 1973.
(Cited on page 5.)
- [19] Vanderlei Bagnato, David E. Pritchard, and Daniel Kleppner. Bose-einstein condensation in an external potential. *Phys. Rev. A*, 35:4354–4358, May 1987.
(Cited on page 5.)
- [20] B.S Deaver and J.M Pierce. Relaxation oscillator model for superconducting bridges. *Physics Letters A*, 38(2):81 – 82, 1972.
(Cited on page 9.)
- [21] E. Madelung. Quantentheorie in hydrodynamischer form. *Zeitschrift für Physik*, 40(3):322–326, Mar 1927.
(Cited on page 9.)
- [22] T. Frisch, Y. Pomeau, and S. Rica. Transition to dissipation in a model of superflow. *Phys. Rev. Lett.*, 69:1644–1647, Sep 1992.
(Cited on pages 12 and 13.)
- [23] C. Raman, M. Köhl, R. Onofrio, D. S. Durfee, C. E. Kuklewicz, Z. Hadzibabic, and W. Ketterle. Evidence for a critical velocity in a bose-einstein condensed gas. *Phys. Rev. Lett.*, 83:2502–2505, Sep 1999.
(Cited on page 13.)
- [24] Woo Jin Kwon, Geol Moon, Sang Won Seo, and Y. Shin. Critical velocity for vortex shedding in a bose-einstein condensate. *Phys. Rev. A*, 91:053615, May 2015.
(Cited on page 14.)
- [25] Woo Jin Kwon, Geol Moon, Jae-yoon Choi, Sang Won Seo, and Yong-il Shin. Relaxation of superfluid turbulence in highly oblate bose-einstein condensates. *Phys. Rev. A*, 90:063627, Dec 2014.
(Cited on page 14.)
- [26] Geol Moon, Woo Jin Kwon, Hyunjik Lee, and Yong-il Shin. Thermal friction on quantum vortices in a bose-einstein condensate. *Phys. Rev. A*, 92:051601, Nov 2015.
(Cited on page 14.)
- [27] Joon Hyun Kim, Woo Jin Kwon, and Y. Shin. Role of thermal friction in relaxation of turbulent bose-einstein condensates. *Phys. Rev. A*, 94:033612,

Sep 2016.

(Cited on page 14.)

- [28] A. Ramanathan, K. C. Wright, S. R. Muniz, M. Zelan, W. T. Hill, C. J. Lobb, K. Helmerson, W. D. Phillips, and G. K. Campbell. Superflow in a toroidal bose-einstein condensate: An atom circuit with a tunable weak link. *Phys. Rev. Lett.*, 106:130401, Mar 2011.
(Cited on pages 14 and 124.)
- [29] D. E. Miller, J. K. Chin, C. A. Stan, Y. Liu, W. Setiawan, C. Sanner, and W. Ketterle. Critical velocity for superfluid flow across the bec-bcs crossover. *Phys. Rev. Lett.*, 99:070402, Aug 2007.
(Cited on page 15.)
- [30] J. Clarke, A. N. Cleland, M. H. Devoret, D. Esteve, and J. Martinis. Quantum mechanics of a macroscopic variable - The phase difference of a Josephson junction. *Science*, 239:992–997, February 1988.
(Cited on pages 15, 123, and 131.)
- [31] Erich J. Mueller. Superfluidity and mean-field energy loops: Hysteretic behavior in bose-einstein condensates. *Phys. Rev. A*, 66:063603, Dec 2002.
(Cited on pages 19 and 123.)
- [32] Dmitri Diakonov, L. M. Jensen, C. J. Pethick, and H. Smith. Loop structure of the lowest bloch band for a bose-einstein condensate. *Phys. Rev. A*, 66:013604, Jul 2002.
(Cited on page 19.)
- [33] Biao Wu and Qian Niu. Nonlinear landau-zener tunneling. *Phys. Rev. A*, 61:023402, Jan 2000.
(Cited on page 19.)
- [34] A H Silver and J E Zimmerman. Quantum States and Transitions in Weakly Connected Superconducting Rings. *Phys. Rev.*, 157(2):317–341, May 1967.
(Cited on pages 19 and 55.)
- [35] S. Eckel, J. G. Lee, F. Jendrzejewski, N. Murray, C. W. Clark, C. J. Lobb, W. D. Phillips, M. Edwards, and G. K. Campbell. Hysteresis in a quantized superfluid ‘atomtronic’ circuit. *Nature*, 506:200–203, February 2014.
(Cited on pages 19, 21, 123, 124, 127, 133, 135, and 140.)
- [36] A. Ramanathan, K. C. Wright, S. R. Muniz, M. Zelan, W. T. Hill, C. J. Lobb, K. Helmerson, W. D. Phillips, and G. K. Campbell. Superflow in a toroidal bose-einstein condensate: An atom circuit with a tunable weak link. *Phys. Rev. Lett.*, 106:130401, Mar 2011.
(Cited on page 20.)

- [37] M. F. Andersen, C. Ryu, Pierre Cladé, Vasant Natarajan, A. Vaziri, K. Helmerson, and W. D. Phillips. Quantized rotation of atoms from photons with orbital angular momentum. *Phys. Rev. Lett.*, 97:170406, Oct 2006. (Cited on page 20.)
- [38] C. Ryu, M. F. Andersen, P. Cladé, Vasant Natarajan, K. Helmerson, and W. D. Phillips. Observation of persistent flow of a bose-einstein condensate in a toroidal trap. *Phys. Rev. Lett.*, 99:260401, Dec 2007. (Cited on page 20.)
- [39] K. C. Wright, R. B. Blakestad, C. J. Lobb, W. D. Phillips, and G. K. Campbell. Driving phase slips in a superfluid atom circuit with a rotating weak link. *Phys. Rev. Lett.*, 110:025302, Jan 2013. (Cited on pages 21 and 22.)
- [40] A. Kumar, N. Anderson, W. D. Phillips, S. Eckel, G. K. Campbell, and S. Stringari. Minimally destructive, Doppler measurement of a quantized, superfluid flow. 2015. (Cited on pages 25, 79, and 103.)
- [41] Amy C. Mathey, Charles W. Clark, and L. Mathey. Decay of a superfluid current of ultracold atoms in a toroidal trap. *Phys. Rev. A*, 90:023604, Aug 2014. (Cited on pages 25, 124, 128, and 130.)
- [42] W. H. Zurek. Cosmological experiments in superfluid helium? *Nature*, 317(10):505, 1985. (Cited on page 25.)
- [43] Grigory E. Volovik. *The universe in a helium droplet*. Clarendon Press, Oxford, 2003. (Cited on page 25.)
- [44] S. Eckel, A. Kumar, T. Jacobson, I. B. Spielman, and G. K. Campbell. A supersonically expanding Bose-Einstein condensate: an expanding universe in the lab. *ArXiv e-prints*, October 2017. (Cited on pages 26, 145, and 153.)
- [45] H.J. Metcalf and van der Straten. *Laser cooling and trapping*. Springer-Verlag New York, 1 edition, 1999. (Cited on page 27.)
- [46] Wolfgang Ketterle, Kendall B. Davis, Michael A. Joffe, Alex Martin, and David E. Pritchard. High densities of cold atoms in a dark spontaneous-force optical trap. *Phys. Rev. Lett.*, 70:2253–2256, Apr 1993. (Cited on page 30.)

- [47] W. Ketterle, D. S. Durfee, and D. M. Stamper-Kurn. Making, probing and understanding Bose-Einstein condensates. *eprint arXiv:cond-mat/9904034*, April 1999.
(Cited on page 37.)
- [48] Anand Ramanathan, Sérgio R Muniz, Kevin C Wright, Russell P Anderson, William D Phillips, Kristian Helmerson, and Gretchen K Campbell. Partial-transfer absorption imaging: a versatile technique for optimal imaging of ultracold gases. *Rev. Sci. Instrum.*, 83(8):083119, August 2012.
(Cited on pages 38, 88, 106, and 113.)
- [49] A. Ramanathan, K. C. Wright, S. R. Muniz, M. Zelan, W. T. Hill, C. J. Lobb, K. Helmerson, W. D. Phillips, and G. K. Campbell. Superflow in a Toroidal Bose-Einstein Condensate: An Atom Circuit with a Tunable Weak Link. *Phys. Rev. Lett.*, 106(13):130401, March 2011.
(Cited on pages 52, 78, 105, and 122.)
- [50] S. Eckel, F. Jendrzejewski, A. Kumar, C. J. Lobb, and G. K. Campbell. Interferometric Measurement of the Current-Phase Relationship of a Superfluid Weak Link. *Phys. Rev. X*, 4(3):031052, September 2014.
(Cited on pages 53, 59, 78, 79, 87, 106, and 112.)
- [51] B. Josephson. Coupled Superconductors. *Rev. Mod. Phys.*, 36(1):216–220, jan 1964.
(Cited on page 54.)
- [52] Loshak A. Backhaus S. Davis J. C. Packard R. E. Pereverzev, S. V. Quantum oscillations between two weakly coupled reservoirs of superfluid ^3He . *Nature*, 388:449, July 1997.
(Cited on page 56.)
- [53] I. Hahn E. Hoskinson, Y. Sato and R. E. Packard. Transition from phase slips to the josephson effect in a superfluid ^4He weak link. *Nature Physics*, 2:23–26, 2006.
(Cited on page 56.)
- [54] S. Raghavan, A. Smerzi, S. Fantoni, and S. R. Shenoy. Coherent oscillations between two weakly coupled bose-einstein condensates: Josephson effects, π oscillations, and macroscopic quantum self-trapping. *Phys. Rev. A*, 59:620–633, Jan 1999.
(Cited on page 56.)
- [55] Lahoud E. Shomroni I. Steinhauer J. Levy, S. The a.c. and d.c. josephson effects in a bose-einstein condensate. *Nature Letters*, 449:579, 2007.
(Cited on pages 56 and 78.)

- [56] Michael Albiez, Rudolf Gati, Jonas Fölling, Stefan Hunsmann, Matteo Cristiani, and Markus K. Oberthaler. Direct observation of tunneling and non-linear self-trapping in a single bosonic josephson junction. *Phys. Rev. Lett.*, 95:010402, Jun 2005.
(Cited on page 56.)
- [57] F. Piazza, L. A. Collins, and A. Smerzi. Current-phase relation of a bose-einstein condensate flowing through a weak link. *Phys. Rev. A*, 81:033613, Mar 2010.
(Cited on page 56.)
- [58] K. C. Wright, R. B. Blakestad, C. J. Lobb, W. D. Phillips, and G. K. Campbell. Driving phase slips in a superfluid atom circuit with a rotating weak link. *Phys. Rev. Lett.*, 110:025302, Jan 2013.
(Cited on pages 57 and 127.)
- [59] Y. Castin and R. Dum. Bose-einstein condensates in time dependent traps. *Phys. Rev. Lett.*, 77:5315–5319, Dec 1996.
(Cited on page 75.)
- [60] Yu. Kagan, E. L. Surkov, and G. V. Shlyapnikov. Evolution of a bose-condensed gas under variations of the confining potential. *Phys. Rev. A*, 54:R1753–R1756, Sep 1996.
(Cited on page 75.)
- [61] K. C. Wright, R. B. Blakestad, C. J. Lobb, W. D. Phillips, and G. K. Campbell. Driving phase slips in a superfluid atom circuit with a rotating weak link. *Phys. Rev. Lett.*, 110:025302, Jan 2013.
(Cited on pages 78, 105, and 120.)
- [62] S. Eckel, F. Jendrzejewski, A. Kumar, C. J. Lobb, and G. K. Campbell. Interferometric measurement of the current-phase relationship of a superfluid weak link. *Phys. Rev. X*, 4:031052, Sep 2014.
(Cited on pages 78, 79, 105, 108, and 112.)
- [63] F. Jendrzejewski, S. Eckel, N. Murray, C. Lanier, M. Edwards, C. J. Lobb, and G. K. Campbell. Resistive flow in a weakly interacting bose-einstein condensate. *Phys. Rev. Lett.*, 113:045305, Jul 2014.
(Cited on pages 78 and 124.)
- [64] G Edward Marti, Ryan Olf, and Dan M. Stamper-Kurn. Collective excitation interferometry with a toroidal Bose-Einstein condensate. *Phys. Rev. A*, 91(1):013602, January 2015.
(Cited on pages 79, 103, 108, 117, and 120.)
- [65] F Jendrzejewski, S Eckel, N Murray, C Lanier, M Edwards, C. J. Lobb, and G. K. Campbell. Resistive Flow in a Weakly Interacting Bose-Einstein Condensate. *Phys. Rev. Lett.*, 113(4):045305, July 2014.
(Cited on pages 79 and 105.)

- [66] Augusto Smerzi and Stefano Fantoni. Large amplitude oscillations of a bose condensate. *Phys. Rev. Lett.*, 78:3589–3593, May 1997.
(Cited on page 80.)
- [67] S. Choi, S. Morgan, and K. Burnett. Phenomenological damping in trapped atomic Bose-Einstein condensates. *Phys. Rev. A*, 57(5):4057–4060, May 1998.
(Cited on page 80.)
- [68] S. A. Morgan, S. Choi, K. Burnett, and M. Edwards. Nonlinear mixing of quasiparticles in an inhomogeneous bose condensate. *Phys. Rev. A*, 57:3818–3829, May 1998.
(Cited on page 80.)
- [69] N Proukakis, S Gardiner, M Davis, and M Szymanska. *Quantum Gases: Finite Temperatures and Non-equilibrium Dynamics*. Cold atoms. Imperial College Press, 2013.
(Cited on page 80.)
- [70] P. G. Kevrekidis, D. J. Frantzeskakis, and R. Carretero-Gonzalez. *The defocusing nonlinear Schrödinger equation : from dark solitons to vortices and vortex rings*. Society for Industrial and Applied Mathematics, 2015.
(Cited on pages 81 and 101.)
- [71] Jeffrey G. Lee and W. T. Hill. Spatial shaping for generating arbitrary optical dipole traps for ultracold degenerate gases. *Rev. Sci. Instrum.*, 85(10):–, 2014.
(Cited on pages 87 and 112.)
- [72] S. Stringari and L. Pitaevskii. *Bose-Einstein Condensation*. Oxford University Press, 2003.
(Cited on pages 89 and 90.)
- [73] C.J. Pethick and H. Smith. *Bose-Einstein Condensation in Dilute Gases*. Cambridge University Press, second edition, 2008.
(Cited on pages 89, 90, and 91.)
- [74] E. Zaremba. Sound propagation in a cylindrical bose-condensed gas. *Phys. Rev. A*, 57:518–521, Jan 1998.
(Cited on pages 93 and 115.)
- [75] M. R. Andrews, D. M. Kurn, H.-J. Miesner, D. S. Durfee, C. G. Townsend, S. Inouye, and W. Ketterle. Propagation of sound in a bose-einstein condensate. *Phys. Rev. Lett.*, 79:553–556, Jul 1997.
(Cited on page 100.)
- [76] Fabrice Béthuel, Philippe Gravejat, and Jean-Claude Saut. Travelling Waves for the Gross-Pitaevskii Equation II. *Commun. Math. Phys.*, 285(2):567–651, January 2009.
(Cited on page 101.)

- [77] D. J. Frantzeskakis. Dark solitons in atomic BoseEinstein condensates: from theory to experiments. *J. Phys. A Math. Theor.*, 43(21):213001, May 2010. (Cited on page [101](#).)
- [78] A. M. Kamchatnov and N. Pavloff. Generation of dispersive shock waves by the flow of a bose-einstein condensate past a narrow obstacle. *Phys. Rev. A*, 85:033603, Mar 2012. (Cited on page [101](#).)
- [79] Charles J. M. Mathy, Mikhail B. Zvonarev, and Eugene Demler. Quantum flutter of supersonic particles in one-dimensional quantum liquids. *Nat. Phys.*, 8(12):881–886, October 2012. (Cited on page [101](#).)
- [80] I. Zapata, M. Albert, R. Parentani, and F. Sols. Resonant Hawking radiation in BoseEinstein condensates. *New J. Phys.*, 13(6):063048, June 2011. (Cited on page [101](#).)
- [81] Florent Michel and Renaud Parentani. Nonlinear effects in time-dependent transonic flows: An analysis of analog black hole stability. *Phys. Rev. A*, 91:053603, May 2015. (Cited on page [101](#).)
- [82] Jeff Steinhauer. Observation of self-amplifying hawking radiation in an analogue black-hole laser. *Nature Physics*, 10(11):864–869, 2014. (Cited on page [102](#).)
- [83] M. Zak and I. Kulikov. Supersonic effects and shock waves in a Bose-Einstein condensate. *Phys. Lett. A*, 307:99–106, January 2003. (Cited on page [102](#).)
- [84] Igor Kulikov and Michail Zak. Shock waves in a bose-einstein condensate. *Phys. Rev. A*, 67:063605, Jun 2003. (Cited on page [102](#).)
- [85] Bogdan Damski. Formation of shock waves in a bose-einstein condensate. *Phys. Rev. A*, 69:043610, Apr 2004. (Cited on page [102](#).)
- [86] J. J. Chang, P. Engels, and M. A. Hoefer. Formation of dispersive shock waves by merging and splitting bose-einstein condensates. *Phys. Rev. Lett.*, 101:170404, Oct 2008. (Cited on page [102](#).)
- [87] R. Meppelink, S. B. Koller, J. M. Vogels, P. van der Straten, E. D. van Ooijen, N. R. Heckenberg, H. Rubinsztein-Dunlop, S. A. Haine, and M. J. Davis. Observation of shock waves in a large bose-einstein condensate. *Phys. Rev. A*, 80:043606, Oct 2009. (Cited on page [102](#).)

- [88] Sidney Shapiro. Josephson Currents in Superconducting Tunneling: The Effect of Microwaves and Other Observations. *Phys. Rev. Lett.*, 11(2):80–82, July 1963.
(Cited on page [103](#).)
- [89] F Sols and S Kohler. Shapiro Resonances in an Isolated ac-Driven Double Bose Einstein Condensate. *Laser Phys.*, 14(9):1259–1264, 2004.
(Cited on page [103](#).)
- [90] A.J. Makowski and S.T. Dembiński. Exactly solvable models with time-dependent boundary conditions. *Phys. Lett. A*, 154(5-6):217–220, 1991.
(Cited on page [103](#).)
- [91] Barbara Drossel and Thomas Prellberg. Dynamics of a single particle in a horizontally shaken box. *Eur. Phys. J. B*, 1(4):533–543, March 1998.
(Cited on page [103](#).)
- [92] Petr Seba. Quantum chaos in the Fermi-accelerator model. *Phys. Rev. A*, 41(5):2306–2310, March 1990.
(Cited on page [103](#).)
- [93] Vladimir Grubelnik, Marjan Logar, and Marko Robnik. Quantum Fermi acceleration in the resonant gaps of a periodically driven one-dimensional potential box. *J. Phys. A Math. Theor.*, 47(35):355103, 2014.
(Cited on page [103](#).)
- [94] C. Ryu, M. F. Andersen, P. Cladé, Vasant Natarajan, K. Helmerson, and W. D. Phillips. Observation of persistent flow of a bose-einstein condensate in a toroidal trap. *Phys. Rev. Lett.*, 99:260401, Dec 2007.
(Cited on pages [105](#) and [122](#).)
- [95] C. Ryu, P. W. Blackburn, A. A. Blinova, and M. G. Boshier. Experimental realization of josephson junctions for an atom squid. *Phys. Rev. Lett.*, 111:205301, Nov 2013.
(Cited on page [105](#).)
- [96] S. Stringari. Collective Excitations of a Trapped Bose-Condensed Gas. *Phys. Rev. Lett.*, 77(12):2360, 1996.
(Cited on page [106](#).)
- [97] Mark Edwards, P. A. Ruprecht, K Burnett, R. J. Dodd, and Charles W. Clark. Collective Excitations of Atomic Bose-Einstein Condensates. *Phys. Rev. Lett.*, 77(9):1671, 1996.
(Cited on page [106](#).)
- [98] F Chevy, K W Madison, and J Dalibard. Measurement of the Angular Momentum of a Rotating Bose-Einstein Condensate. *Phys. Rev. Lett.*, 85(11):2223, 2000.
(Cited on page [106](#).)

- [99] P. Haljan, I. Coddington, P. Engels, and E. Cornell. Driving Bose-Einstein-Condensate Vorticity with a Rotating Normal Cloud. *Phys. Rev. Lett.*, 87(21):210403, 2001.
(Cited on page 106.)
- [100] Francesca Zambelli and Sandro Stringari. Quantized Vortices and Collective Oscillations of a Trapped Bose-Einstein Condensate. *Phys. Rev. Lett.*, 81(9):1754, 1998.
(Cited on pages 106 and 108.)
- [101] Anatoly A. Svidzinsky and Alexander L. Fetter. Normal modes of a vortex in a trapped Bose-Einstein condensate. *Phys. Rev. A*, 58(4):3168, 1998.
(Cited on page 106.)
- [102] M. Cozzini, B. Jackson, and S. Stringari. Vortex signatures in annular Bose-Einstein condensates. *Phys. Rev. A*, 73(1):013603, 2006.
(Cited on page 106.)
- [103] Stuart Moulder, Scott Beattie, Robert P. Smith, Naaman Tammuz, and Zoran Hadzibabic. Quantized supercurrent decay in an annular Bose-Einstein condensate. *Phys. Rev. A*, 86(1):013629, 2012.
(Cited on page 106.)
- [104] Noel Murray, Michael Krygier, Mark Edwards, K. C. Wright, G. K. Campbell, and Charles W. Clark. Probing the circulation of ring-shaped Bose-Einstein condensates. *Phys. Rev. A*, 88(5):053615, 2013.
(Cited on page 106.)
- [105] C Ryu, K C Henderson, and M G Boshier. Creation of matter wave Bessel beams and observation of quantized circulation in a Bose-Einstein condensate. *New J. Phys.*, 16(1):013046, January 2014.
(Cited on page 106.)
- [106] L. Corman, L. Chomaz, T. Bienaimé, R. Desbuquois, C. Weitenberg, S. Nascimbène, J. Dalibard, and J. Beugnon. Quench-induced supercurrents in an annular Bose gas. *Phys. Rev. Lett.*, 113:135302, Sep 2014.
(Cited on page 106.)
- [107] M. R. Andrews, M.-O. Mewes, N. J. van Druten, D. S. Durfee, D. M. Kurn, and W. Ketterle. Direct, Nondestructive Observation of a Bose Condensate. *Science*, 273(5271):84, 1996.
(Cited on page 106.)
- [108] M. R. Andrews, C. G. Townsend, H.-J. Miesner, D. S. Durfree, D. M. Kurn, and W. Ketterle. Observation of Interference Between Two Bose Condensates. *Science*, 275(5300):637, January 1997.
(Cited on page 106.)

- [109] L. Turner, K. Domen, and R. Scholten. Diffraction-contrast imaging of cold atoms. *Phys. Rev. A*, 72(3):031403, 2005.
(Cited on page 106.)
- [110] Miroslav Gajdacz, Poul L Pedersen, Troels Mørch, Andrew J Hilliard, Jan Arlt, and Jacob F Sherson. Non-destructive Faraday imaging of dynamically controlled ultracold atoms. *Rev. Sci. Instrum.*, 84(8):083105, 2013.
(Cited on page 108.)
- [111] R. Mathew, A. Kumar, S. Eckel, F. Jendrzejewski, G. K. Campbell, Mark Edwards, and E. Tiesinga. Self-heterodyne detection of the in situ phase of an atomic superconducting quantum interference device. *Phys. Rev. A*, 92(3):033602, 2015.
(Cited on page 112.)
- [112] J.F. Jarvis, C.N. Judice, and W.H. Ninke. A survey of techniques for the display of continuous tone pictures on bilevel displays. *Comput. Graph. Image Process.*, 5(1):13, March 1976.
(Cited on page 113.)
- [113] J. Hope and J. Close. Limit to Minimally Destructive Optical Detection of Atoms. *Phys. Rev. Lett.*, 93(18):180402, 2004.
(Cited on pages 113 and 119.)
- [114] P. O. Fedichev, G. V. Shlyapnikov, and J. T. M. Walraven. Damping of Low-Energy Excitations of a Trapped Bose-Einstein Condensate at Finite Temperatures. *Phys. Rev. Lett.*, 80(11):2269, 1998.
(Cited on page 117.)
- [115] N. Katz, J. Steinhauer, R. Ozeri, and N. Davidson. Beliaev Damping of Quasiparticles in a Bose-Einstein Condensate. *Phys. Rev. Lett.*, 89(22):220401, 2002.
(Cited on page 117.)
- [116] D. V. Freilich, D. M. Bianchi, A. M. Kaufman, T. K. Langin, and D. S. Hall. Real-Time Dynamics of Single Vortex Lines and Vortex Dipoles in a Bose-Einstein Condensate. *Science*, 329(5996):1182, 2010.
(Cited on page 119.)
- [117] J. File and R. G. Mills. Observation of persistent current in a superconducting solenoid. *Phys. Rev. Lett.*, 10:93–96, Feb 1963.
(Cited on page 122.)
- [118] J. B. Mehl and W. Zimmermann. Flow of superfluid helium in a porous medium. *Phys. Rev.*, 167:214–229, Mar 1968.
(Cited on page 122.)

- [119] I. Rudnick, H. Kojima, W. Veith, and R. S. Kagiwada. Observation of superfluid-helium persistent current by doppler-shifted splitting of fourth-sound resonance. *Phys. Rev. Lett.*, 23:1220–1223, Nov 1969.
(Cited on page [122](#).)
- [120] Scott Beattie, Stuart Moulder, Richard J. Fletcher, and Zoran Hadzibabic. Persistent currents in spinor condensates. *Phys. Rev. Lett.*, 110:025301, Jan 2013.
(Cited on page [122](#).)
- [121] D. Sanvitto, F. M. Marchetti, M. H. Szymańska, G. Tosi, M. Baudisch, F. P. Laussy, D. N. Krizhanovskii, M. S. Skolnick, L. Marrucci, A. Lemaître, J. Bloch, C. Tejedor, and L. Viña. Persistent currents and quantized vortices in a polariton superfluid. *Nature Physics*, 6:527–533, July 2010.
(Cited on page [122](#).)
- [122] R. Doll and M. Näbauer. Experimental proof of magnetic flux quantization in a superconducting ring. *Phys. Rev. Lett.*, 7:51–52, Jul 1961.
(Cited on page [122](#).)
- [123] A.O Caldeira and A.J Leggett. Quantum tunnelling in a dissipative system. *Annals of Physics*, 149(2):374 – 456, 1983.
(Cited on page [123](#).)
- [124] John M. Martinis, Michel H. Devoret, and John Clarke. Energy-level quantization in the zero-voltage state of a current-biased josephson junction. *Phys. Rev. Lett.*, 55:1543–1546, Oct 1985.
(Cited on page [123](#).)
- [125] John M. Martinis and Hermann Grabert. Thermal enhancement of macroscopic quantum tunneling: Derivation from noise theory. *Phys. Rev. B*, 38:2371–2379, Aug 1988.
(Cited on page [123](#).)
- [126] R. Rouse, Siyuan Han, and J. E. Lukens. Observation of resonant tunneling between macroscopically distinct quantum levels. *Phys. Rev. Lett.*, 75:1614–1617, Aug 1995.
(Cited on page [123](#).)
- [127] E. Zaremba, T. Nikuni, and A. Griffin. Dynamics of trapped bose gases at finite temperatures. *Journal of Low Temperature Physics*, 116(3):277–345, 1999.
(Cited on pages [124](#) and [142](#).)
- [128] P.B. Blakie, A.S. Bradley, M.J. Davis, R.J. Ballagh, and C.W. Gardiner. Dynamics and statistical mechanics of ultra-cold bose gases using c-field techniques. *Advances in Physics*, 57(5):363–455, 2008.
(Cited on page [124](#).)

- [129] S. J. Rooney, A. S. Bradley, and P. B. Blakie. Decay of a quantum vortex: Test of nonequilibrium theories for warm Bose-Einstein condensates. *Phys. Rev. A*, 81(2):023630, feb 2010.
(Cited on page [124](#).)
- [130] S. J. Rooney, A. J. Allen, U. Zülicke, N. P. Proukakis, and A. S. Bradley. Reservoir interactions of a vortex in a trapped three-dimensional Bose-Einstein condensate. *Phys. Rev. A*, 93(6):063603, jun 2016.
(Cited on page [124](#).)
- [131] Michikazu Kobayashi and Makoto Tsubota. Thermal Dissipation in Quantum Turbulence. *Phys. Rev. Lett.*, 97(14):145301, oct 2006.
(Cited on page [124](#).)
- [132] B. Jackson, N. Proukakis, C. Barenghi, and E. Zaremba. Finite-temperature vortex dynamics in Bose-Einstein condensates. *Phys. Rev. A*, 79(5):053615, may 2009.
(Cited on page [124](#).)
- [133] R. A. Duine, B. W. A. Leurs, and H. T. C. Stoof. Noisy dynamics of a vortex in a partially bose-einstein condensed gas. *Phys. Rev. A*, 69:053623, May 2004.
(Cited on pages [124](#) and [131](#).)
- [134] Natalia Berloff and Anthony Youd. Dissipative Dynamics of Superfluid Vortices at Nonzero Temperatures. *Phys. Rev. Lett.*, 99(14):145301, oct 2007.
(Cited on page [124](#).)
- [135] P. O. Fedichev and G. V. Shlyapnikov. Dissipative dynamics of a vortex state in a trapped bose-condensed gas. *Phys. Rev. A*, 60:R1779–R1782, Sep 1999.
(Cited on pages [124](#) and [131](#).)
- [136] Geol Moon, Woo Jin Kwon, Hyunjik Lee, and Yong-il Shin. Thermal friction on quantum vortices in a bose-einstein condensate. *Phys. Rev. A*, 92:051601, Nov 2015.
(Cited on page [124](#).)
- [137] William A. Little. Decay of persistent currents in small superconductors. *Phys. Rev.*, 156:396–403, Apr 1967.
(Cited on page [130](#).)
- [138] Joachim Brand and William P Reinhardt. Generating ring currents, solitons and svortices by stirring a bose-einstein condensate in a toroidal trap. *Journal of Physics B: Atomic, Molecular and Optical Physics*, 34(4):L113, 2001.
(Cited on page [130](#).)
- [139] A Muoz Mateo and J Brand. Stability and dispersion relations of three-dimensional solitary waves in trapped boseeinstein condensates. *New Journal of Physics*, 17(12):125013, 2015.
(Cited on page [130](#).)

- [140] Mark J. H. Ku, Wenjie Ji, Biswaroop Mukherjee, Elmer Guardado-Sanchez, Lawrence W. Cheuk, Tarik Yefsah, and Martin W. Zwierlein. Motion of a solitonic vortex in the bec-bcs crossover. *Phys. Rev. Lett.*, 113:065301, Aug 2014.
(Cited on page 130.)
- [141] Giacomo Valtolina, Alessia Burchianti, Andrea Amico, Elettra Neri, Klejdja Khani, Jorge Amin Seman, Andrea Trombettoni, Augusto Smerzi, Matteo Zaccanti, Massimo Inguscio, and Giacomo Roati. Josephson effect in fermionic superfluids across the bec-bcs crossover. *Science*, 350(6267):1505–1508, 2015.
(Cited on page 130.)
- [142] Simone Donadello, Simone Serafini, Marek Tylutki, Lev P. Pitaevskii, Franco Dalfovo, Giacomo Lamporesi, and Gabriele Ferrari. Observation of solitonic vortices in bose-einstein condensates. *Phys. Rev. Lett.*, 113:065302, Aug 2014.
(Cited on page 130.)
- [143] M. Tylutki, S. Donadello, S. Serafini, L. P. Pitaevskii, F. Dalfovo, G. Lamporesi, and G. Ferrari. Solitonic vortices in bose-einstein condensates. *The European Physical Journal Special Topics*, 224(3):577–583, 2015.
(Cited on page 130.)
- [144] Joachim Brand and William P. Reinhardt. Solitonic vortices and the fundamental modes of the snake instability: Possibility of observation in the gaseous Bose-Einstein condensate. *Phys. Rev. A*, 65(4):043612, 2002.
(Cited on page 130.)
- [145] S. Komineas and N. Papanicolaou. Solitons, solitonic vortices, and vortex rings in a confined Bose-Einstein condensate. *Phys. Rev. A*, 68(4):043617, oct 2003.
(Cited on page 130.)
- [146] Richard F. Voss and Richard A. Webb. Macroscopic quantum tunneling in 1- μm nb josephson junctions. *Phys. Rev. Lett.*, 47:265–268, Jul 1981.
(Cited on page 131.)
- [147] Gentaro Watanabe, F. Dalfovo, F. Piazza, L. P. Pitaevskii, and S. Stringari. Critical velocity of superfluid flow through single-barrier and periodic potentials. *Phys. Rev. A*, 80:053602, Nov 2009.
(Cited on page 133.)
- [148] W. Ketterle, D. S. Durfee, and D. M. Stamper-Kurn. Making, probing and understanding bose-einstein condensates. In M. Inguscio, S. Stringari, and C. E. Wieman, editors, *Bose-Einstein Condensation in Atomic Gases*, volume 160 of *Proceedings of the International School of Physics “Enrico Fermi”*, chapter 3, pages 67–176. IOS press, 1999.
(Cited on page 137.)

- [149] Nir Friedman, Ariel Kaplan, and Nir Davidson. Dark optical traps for cold atoms. 48:99 – 151, 2002.
(Cited on page [138](#).)
- [150] Donald P. Leach and Albert P. Malvino. *Digital Principles and Applications*. Glencoe/McGraw-Hill, 5th edition, 1994.
(Cited on page [148](#).)